TRANSPORT PROCESSES IN WAVY WALLED CHANNELS

A Dissertation
Presented to
The Academic Faculty

By

Zachary Grant Mills

In Partial Fulfillment
of the Requirements for the Degree
Doctor of Philosophy in the
George W. Woodruff School of Mechanical Engineering

Georgia Institute of Technology
May 2017

TRANSPORT PROCESSES IN WAVY WALLED CHANNELS

Approved by:

Dr. Alexander Alexeev, Advisor
School of Mechanical Engineering
Georgia Institute of Technology

Dr. Yogendra Joshi
School of Mechanical Engineering
Georgia Institute of Technology

Dr. S. Mostafa Ghiaasiaan
School of Mechanical Engineering
Georgia Institute of Technology

Dr. Alok Warey
Global Research and Development
General Motors

Dr. David L. Hu
School of Mechanical Engineering
Georgia Institute of Technology

Date Approved: 16 December, 2016

To my better half, Laura, my parents Beth and Jeff and Susan and Zack, my brothers Heath and Ross and my sisters Brett and Erin.

Without all of your love patience and support, this work would not have been possible.

ACKNOWLEDGEMENTS

This work is dedicated to my Fiancée, Laura Hardeman, for her unconditional love, understanding, and patience. I would not be where I am today without her encouragement and support.

I would like to thank my advisor, Dr. Alexander Alexeev, for his encouragement and support throughout my time as Ph.D. student, and for introducing me to the world of computational fluid mechanics. In addition, I would like to thank Dr. Alexeev for the invaluable guidance and advice he has given me other the last few years.

I would also like to thank my thesis committee, Dr. Mostafa Ghiaasiaan, Dr. David Hu, Dr. Yogendra Joshi and Dr. Alok Warey for reviewing my dissertation and providing me with their valuable insight and comments.

I am also thankful for my lab mates, Hassan, Wenbin, Peter, Matt, Nick, Yaro and Sam for all of the help, advice, encouragement and, most importantly, entertainment you have given me during our time working together.

I would also like to thank my friends, Brad, Page, Sean, Nina, Stephanie, Jeremy and Ryan for the love, support, and guidance they have shown me over the years.

Lastly, I would like to thank my family. My parents, Beth and Jeff and Susan and Zack, My brothers, Heath and Ross, and my sisters, Brett and Erin, for their continuous love and support. Also, I would like to thank my pets Alice Pooper “Magoops”, Eva

“Veevers”, Zoe “The Zoester”, Grimace “Flim Flam”, Mia “The Cheese Monster”, Tabby “Tabby McFlabs” and Tiger “Tigerman” for showing me so much unconditional love.

TABLE OF CONTENTS

LIST OF TABLES

LIST OF FIGURES

SUMMARY

Due to their complex shape, wavy walled geometries are capable of inducing unsteady and even chaotic flows at low Reynolds numbers. The convective effects of the unsteady motion significantly enhances heat and mass transport in the fluid. Because of this, wavy walled channels are commonly used in applications such as heat exchangers. Despite their common use however, a systematic investigation of the dependence of the fluid flow and heat transfer on the geometric parameters of the channel does not exist.

In many heat exchanger applications, the working fluid contains suspended particulates. When cooling these particle laden flows, thermophoretic forces induced on the particles by thermal gradients in the fluid result in their deposition along the cooler walls. This process, known as fouling, leads to the formation of a porous layer, which reduces the effectiveness of the cooler. One application in which fouling is a significant issue is exhaust gas recirculation (EGR) used in diesel and gasoline engines to reduce nitrogen oxides (NO_x) emissions. The heat exchanger used in this process experiences rapid degradation in performance from fouling caused by the high concentration of soot particles entrained in the exhaust gas. Recently, engine manufacturers have begun using wavy walled heat exchangers as empirical evidence suggests that this geometry is less prone to fouling. However, a limited amount of research has been performed to understand how this geometry reduces fouling and the dependence of this reduction on the geometric parameters of the channel.

In this work we use computational modeling to investigate the effect of asymmetric wavy walled channel geometries on laminar fluid flow and heat/mass transfer. To this end,

we develop a computational model based on the lattice Boltzmann method, explicit finite differences and Brownian dynamics to simulate unsteady viscous flow and heat/mass transport in wavy walled channel geometries and use this model to systematically examine these processes. Furthermore, we investigate the formation of deposit layers resulting from thermophoretic deposition of particulates transported by the flow onto the channel walls and probe how this process can be mitigated using a wavy wall geometry. The results from our studies are important for designing laminar heat/mass exchangers utilizing unsteady flows for enhancing transport processes. Additionally these results provide valuable information necessary to develop heat exchangers which are less prone to fouling.

CHAPTER 1. INTRODUCTION

In laminar flows in straight pipes and channels, the rate of heat and mass transfer is limited by the diffusive timescale. This rate can be improved by increasing the flow rate to achieve turbulent flow which induces turbulent mixing. This occurs at the cost of increased viscous losses and a reduced contact time of the fluid with the walls, which in applications such as heat exchangers, reduces their overall effectiveness. Additionally, achieving the Reynolds numbers necessary to induce turbulence is difficult with small length scales such as those found in microfluidic devices. Due to these shortcomings associated with utilizing turbulent mixing, another common approach to facilitate mixing and heat/mass transport is the use of complex channel geometries to induce convective transport and mixing in laminar flows.[1]

The use of complex geometries to enhance mixing has received considerable attention by researchers and engineers and a multitude of geometries have been investigated. Examples of a few geometries used in compact heat exchangers and microfluidic devices are described in reviews by Jacobi and Shah[2] and Hessel et al.,[3] respectively. A geometry of particular interest for this study is channels with in-phase periodic sinusoidal shaped wavy walls, an example of which is provided in Figure 1.1. This is due to the potential for this geometry to induce significant mixing, while being considerably easier to manufacture and introducing smaller additional frictional losses compared to other more complex geometries.[4]

In many technological applications, the working fluid contains suspended particulates. Cooling of such fluid induces deposition of the particulates onto the inner

walls of the heat exchanger, a process known as fouling. The deposits may form a porous layer characterized by a low thermal conductivity that acts to insulate the cold walls from the hot fluid and can severely reduce the effectiveness of the heat exchanger.[5] The mechanisms behind the particle deposition include turbulent impaction (when flow is turbulent), diffusion and thermophoresis, which is the motion of particles toward areas of lower temperatures. The magnitude of the thermophoretic motion is proportional to the thermal gradient at the location of the particles. Because of the large temperature gradients in heat exchangers, this is often the dominant mechanism for particle deposition.[6-9] When heat exchangers are used in applications where the fluids contain high amounts of entrained particulates, the effects of fouling become a significant obstacle that must be overcome.

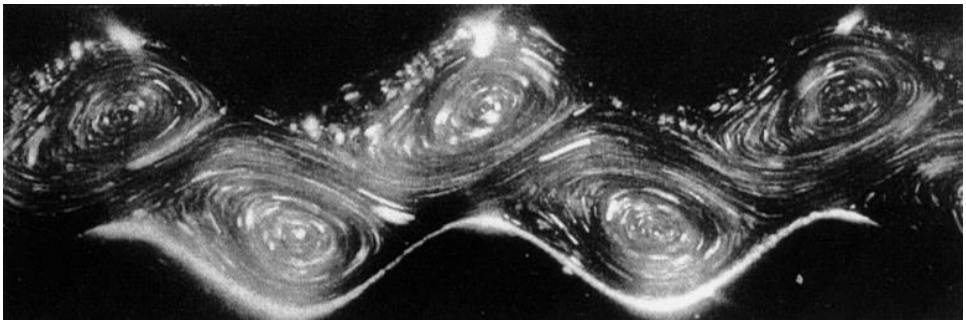

Figure 1.1 – Visualization of streamlines in flow through an asymmetric wavy walled channel.[10]

An application where fouling is a significant issue is exhaust gas recirculation (EGR) used in diesel and gasoline engines. EGR is a commonly used method to reduce the amount of nitrogen oxides (NO_x) generated by diesel engines in order to meet the emission regulations found in most developed countries. This is done by redirecting a portion of the exhaust gas through a heat exchanger, reducing its temperature, before directing it into the intake manifold of the engine along with fresh air. This reduces the combustion

temperatures in the engine cylinders, which in turn reduces the amount of NO_x generated by the combustion process.[11]

EGR is a highly effective method of reducing NO_x generation; however, the need for a heat exchanger to reduce the exhaust temperature does create a significant engineering problem, especially in diesel engines. This is due to the high levels of soot particles in diesel exhaust, causing fouling in the heat exchanger to occur so rapidly that they are rendered ineffective in a matter of hours (an example of a fouled EGR heat exchanger can be seen in Figure 1.2).[12-14] Because of this, it is important to identify efficient methods for reducing the fouling rate in EGR heat exchangers. Using the wavy walled geometry is a promising approach that can be employed to reduce fouling in addition to increasing the heat transfer effectiveness.

Figure 1.2 – Image of a fouled EGR heat exchanger.[15]

1.1 Background

In this section, we provide a brief overview of the current state of research into the wavy walled channel geometry. The overview is divided into three subsections with research into the flow through the channel, the heat/mass transfer enhancement induced by the geometry and its effect on fouling in heat exchangers (specifically EGR coolers) grouped together. Additionally, the fouling subsection provides a general discussion of EGR fouling and computational models developed for simulating the fouling layer development.

1.1.1 Fluid Flow

The geometry of wavy walled channels is capable of inducing complex flow patterns in the fluid flowing through it. These patterns are the result of vortices generated by the wall geometry including their shedding from the walls of the channel which in turn can lead to periodic, quasi-periodic and chaotic flows at low Reynolds numbers. Because of this, a significant amount of research has been performed in order to better understand how the geometry influences the flow, as well as to provide a foundation for future investigations into harnessing this flow to enhance heat and mass transport.

Multiple studies have been performed to determine the effects of sinusoidal-shaped geometries on the onset of circulation and unsteady motion in flow within the channel. These studies each focused on either one or both of two types of wavy walled geometries, which are a converging-diverging (symmetric) channel with the walls 180° out of phase and an asymmetric channel with the walls in phase with each other. These studies indicate

that sinusoidal geometries can induce unsteady laminar flows with significant circulation at low Reynolds numbers.

Using numerical simulations, Sobey[16] investigated the flow in symmetric and asymmetric wavy channels and determined that, at a critical Reynolds number, inertial effects lead to flow separation and the formation of vortices in the furrows of the channels. He also described the onset of unsteady flow as Re increases, which results from the ejection and subsequent shedding of a new vortex. Stephanoff et al.[17] used experiments to visualize the flow and support the predictions for the symmetric channel made by Sobey.

Guzmán, Amon and others used numerical simulations to investigate flow bifurcations and the route taken by the flow as it transitions to chaos in both symmetric and asymmetric channels.[18-24] In their research, they found that both channel geometries induced chaotic flows at significantly lower Reynolds numbers than those necessary in straight channels, but at the cost of higher frictional losses. Additionally, they found that depending on the ratio of the wall amplitude to its period, the flow transitions to chaotic through either the Feigenbaum (successive period doubling bifurcations) or the Ruelle-Takens-Newhouse (successive Hopf bifurcations) scenarios.[18, 24]

Using a linear stability analysis, Cho et al.[25] and Cabal et al.[26] examined the dependence of two and three dimensional instabilities on the amplitude of the wavy walls. These analytical studies were limited to relatively low wall amplitudes. They determined the critical Reynolds number at which the flow becomes unstable for several amplitudes. Both groups concluded that the instabilities were Tollmien-Schlichting waves modified by the channel walls. Tollmien-Schlichting waves are viscosity induced instabilities resulting

from the amplification of an initial disturbance.[27] Cho et al.[25] pointed out that the critical Reynolds numbers for asymmetric channels are slightly lower than those of the symmetric channel.

Despite the significant previous research into flow through wavy walled channels, little information exists regarding the onset of circulatory and unsteady flow (both periodic and quasi-periodic) over a wide range of geometric parameters. Furthermore, while Guzmán and Amon investigated the flow at Reynolds numbers well beyond those necessary to induce unsteady flow, the majority of their research focuses on the symmetric converging-diverging channel and, like much of the other research described above, only investigates geometries of a few different dimensions.

1.1.2 Heat/Mass Transfer

Due to the ability of the wavy channel geometry to enhance heat and mass transfer, a significant amount of research has been performed to better understand the mechanisms behind these enhancements. As in the previous section, these studies investigated mixing enhancement in both symmetric and asymmetric wavy walled channels. In these studies, it was determined that the heat/mass transfer is improved by the wavy walled channels due to the increased convective mixing induced by the geometry of the channel.

Using numerical techniques, Wang and Chen investigated the influence of channel aspect ratio on heat transfer in symmetric wavy-walled channels.[28] For each aspect ratio, they performed simulations at several different Reynolds numbers while remaining in the steady flow regime. Their results showed that for small aspect ratios (small amplitudes), the heat transfer enhancement is minimal, but for larger aspect ratios (large amplitudes) the

enhancement is significant. Additionally, the enhancement is increased as Re increases. Wang and Vanka investigated the influence of both steady and unsteady flows in symmetric wavy walled channels on the heat transfer rate.[29] They found that a significant increase in heat transfer accompanies the transition from steady to unsteady flow and they concluded that this increase is the result of oscillations in the flow destabilizing the laminar thermal boundary layer.

Several papers have investigated the effects of pulsatile flows on heat/mass transfer in both asymmetric and symmetric wavy walled channels.[10, 30-37] The research described in the papers was performed using both experimental and numerical techniques. Results from the investigations indicate that the optimum geometry for mass/heat transfer is dependent on oscillation frequency of the fluid pumping defined using the Strouhal number.

Using direct numerical simulations, Guzmán et al. examined the effect of flow bifurcations in asymmetric wavy channels on heat transfer.[22] Their investigations examined the increase in the heat transfer for a wide range of Reynolds numbers which included multiple bifurcations for three different aspect ratios and two Prandtl numbers. By comparing the Nusselt number for a given flow rate with the pumping power required to achieve that flow rate, they showed that a larger Prandtl number results in a significantly greater return in heat transfer for a given increase in pumping power.

Sui et al. used numerical simulations[38, 39] and experiments[40] to investigate the effects of three dimensional asymmetric wavy channels with rectangular cross sections on flow and heat transfer in microchannels. They found that secondary flows (Dean vortices) are generated by the geometry of the channel, and location of these vortices varies along the

flow direction. This induces chaotic advection that significantly increases heat transfer. From their results they concluded that the increase in pressure drop associated with wavy channels is less than the increase in heat transfer, which makes wavy walled geometries a viable option for increasing heat transfer in microscale devices. Gong et al.[41] used numerical simulations to study the dependence of flow and heat transfer in both symmetric and asymmetric three dimensional microchannels at low Re on the wall amplitude, wavelength and aspect ratio. From their simulations, they determined that wavy walled channels are a viable option for use in microscale devices to improve heat transfer rates. Also, due to the larger improvement in heat transfer compared to the increase in pressure drop, the asymmetric channel outperforms the symmetric microchannel.

Stone and Vanka[42] studied developing flow and heat transfer in a 2D symmetric wavy walled channel using numerical techniques. They simulated flow in a channel with multiple periods and varied Re (from steady to time periodic) while keeping geometric parameters constant. They found that when the flow becomes unsteady, the mixing between the fluid in the center of the channel and that near the walls increases leading to an increase in heat transfer as well as pressure drop. They extended their research to investigate the influence of geometric parameters for both developing and fully developed flows.[43] Their investigations initially focused on three geometries in which they simulated a long channel with multiple periods. For these geometries they determined the location where the flow becomes unsteady as a function of the Re as well as examining the flow patterns, heat transfer rates and pressure drop associated with the flow in the developing region. They extended their understanding of the effect of wavy walls on heat transfer by simulating a single period with periodic boundary conditions. They varied the amplitude, period and

aspect ratio, and examined the effect on the heat transfer. From their investigations they determined that the transition Re is more dependent on amplitude of the wave than the height of the channel and that the heat transfer enhancement is minimal for steady flow.

Rush et al.[44] used experiments to study the influence of phase shift between the upper and lower walls of a wavy walled channel on fluid flow and heat transfer in the laminar and transitional regimes. Based on their experiments, they made several conclusions: 1) Flow is unsteady and unstable in wavy channels while remaining laminar and the distance necessary for the fluid to travel in the channel before becoming unsteady decreases as Re increases. 2) For symmetric channels, circulation develops in the furrows at low Re and the flow becomes unsteady when the shear layer between the trapped vortices and the core becomes unstable. 3) For asymmetric channels (phase shift of 0 and 90) the circulations develop at a low Re also and "macroscopic mixing occurs when the oscillating reattachment point moves upstream and the impinging flow 'injects' fluid in the trapped vortex." 4) Phase shifts of 0 and 90 lead to development of unsteady flow further upstream than symmetric channel. 5) Amplitude significantly influences the stability of the flow. 6) The geometry of the channel significantly enhances heat transfer for laminar flow.

Metwally and Manglik[45] used numerical simulations to investigate the effect of the Reynolds number, the aspect ratio and the Prandtl number on heat transfer in asymmetric wavy walled channels. In their investigations, they examined the flow and heat transfer for steady flow and unsteady time periodic flows. They found that the use of wavy walled channels produces self-sustained transverse vortices which significantly enhance heat transfer at a nominal friction factor penalty.

Nishimura et al.[46] used experiments to investigate the influence of asymmetric wavy walled channels on mass transfer for flow rates that ranged from laminar to turbulent. They found that for laminar flows, a steady vortex existed in the furrow of the channels and, for turbulent flows, the separated shear layer between the main stream and the recirculation vortex rolls up into a traverse vortex. This is accompanied with vortex fusion and stretching leading to a significant increase in mass transfer rate especially near the flow reattachment point in the large recirculation vortex.

Zhang et al.[47] used numerical simulations to investigate the effect of amplitude, period and flow rate on flow and heat transfer in an asymmetric wavy walled channel. By examining the Colburn j factor, $j = \mathrm{Nu}/\mathrm{Re}\,\mathrm{Pr}^{1/3}$, in each flow, they determined that the heat transfer is significantly enhanced when the flow becomes unsteady. Furthermore, they found that the amplitude of the wall corrugations has the most significant influence on the total performance of the channel.

Manglik et al.[48] used 3D numerical simulations to investigate the influence of Re, width to height aspect ratio, amplitude, and period of asymmetric wavy walled channels on heat transfer and fluid flow. Their investigation considered both constant wall temperatures and constant heat fluxes. Their simulations indicated the formation of secondary cross flows affect the core flow in the center of the channel, which slow the core fluid down. The size and strength of the vortices increases with increasing Re. These vortices serve to thin the thermal boundary layer and increase heat transfer.

Although a substantial amount of research has been conducted to better understand the effects of wavy walled channels on heat and mass transfer, a comprehensive and

systematic picture of how the heat and mass transfer changes for a wide range of system parameters is still missing. Additionally, as with the fluid flow, a majority of research into the heat transfer enhancement in wavy channels is focused on the converging-diverging geometry, while most compact heat exchanger designs utilize the asymmetric channel geometry.[49] This, coupled with the fact that the asymmetric channel has been shown to outperform the converging-diverging channel, indicates a need for further research into the heat transfer enhancement in this geometry.[50]

1.1.3 Heat Exchanger Fouling

Due to the significant effect of fouling on the effectiveness and lifespan of EGR heat exchangers, a considerable amount of research has been conducted investigating this phenomenon. This research includes both the development and use of computational models as well as experiments. Although a few have focused on wavy walled coolers, the majority of studies examined the formation of the fouling layer in simple shell and tube geometries.

Several groups have performed experiments investigating the fouling layer formation and the reduction in effectiveness in shell and tube heat exchangers.[11, 12, 14, 51-53] These investigations showed large degradations in performance in as little as 12 hours of operation and that this degradation was coupled with an increasing thermal resistance of the fouling layer. They also observed that the rate of increase in the thermal resistance, indicating an increasing layer thickness, decreased over time. This continued until the resistance approached an asymptotic value, signifying a steady operating condition was reached.

In order to understand how deposits can be removed from the fouling layer, several groups have narrowed their investigations to focus specifically on the effect of the fluid velocity on shear removal of particles from the surface.[5, 54-56] These studies have found that the critical velocity necessary for shear removal is a function of the particle size with the smallest particles requiring the largest velocities. They have found that this critical velocity provides one explanation for the asymptotic behavior of the fouling layer growth. This is because the increase in the fouling layer thickness decreases the diameter of the tube, causing an increase in the fluid velocity. The narrowing continues until the velocity reaches a critical value where any additional deposits are immediately sheared from the surface.

Various models have been developed by different groups in order simulate the effects of the fouling layer growth in a cooler. The most basic of these are one dimensional models which rely on experimental correlations without explicitly including physical mechanisms accounting for particle removal and re-entrainment.[57, 58] Results obtained with these models compare well with those obtained in the beginning of experiments indicating that they are well suited for investigating the initial fouling in shell and tube coolers.

Other groups have extended these one dimensional models by including mechanisms to capture particle rebound and deposit removal.[59, 60] By including these mechanisms, results from these models compare well with those obtained over the full length of experiments. Even more elaborated models have been developed to account for two and three dimensional depositions, employ a Lagrangian framework to simulate the particle motion, and incorporate highly detailed models for the interaction of particles with the surface.[61-64] In addition to being able to simulate geometries other than a single channel of

a shell and tube cooler, these models are capable of simulating the formation of a fouling layer with greater accuracy than the simple one dimensional models.

In addition to simulations and experiments investigating how the fouling layer develops in the cooler, several studies examining the properties of the deposits have been conducted.[65-67] In these studies, researchers examined the composition of the fouling layer, the structures formed by the deposits in the layer, its thermal properties and its density. Results showed that the layer is composed of soot, metallic ash and sulfate hydrate particles, as well as condensed hydrocarbons which can form complex dendritic structures at the surface. Additionally, by determining the mass of a small section of the layer, the researchers calculated a deposit porosity of ~ 0.98. This high porosity accounts for the thermal conductivity of the layer being much lower than that of carbon soot which is the primary constituent of the layer.

While a large body of research exists on fouling in EGR heat exchangers, only two of these investigations have focused specifically on the wavy walled geometry, both of which utilized numerical simulations. Strebel used computational simulations to investigate thermophoretic deposition of particles in an asymmetric wavy channel with both laminar and turbulent flows.[68] His results showed that compared to a straight channel, the wavy channel induces higher rates of deposition for both laminar and turbulent flows and that this rate increases with the temperature gradient. Additionally he found that for laminar flows, the amount of deposition decreases with an increase in Re while the opposite is true for turbulent flows.

Nagendra et al. used numerical simulations to investigate the deposition of soot particles in a wavy EGR heat exchanger.[69, 70] Using their model they simulated particles entrained in fully developed turbulent flow through a single period of a channel with perfectly adsorbing walls. From their results they concluded that for large wall temperature gradients, the deposition of sub-micron particles is independent of size, and the amount of deposition is linearly correlated with the wall temperature gradient. Additionally they found that the deposition rate increases with decreasing Re.

In addition to these two computational studies, a survey of fouled EGR coolers from production vehicles conducted by Lance et al. included coolers with wavy walled geometries.[67] In their examination of fouling in the wavy walled cooler, they observed that the leading edge of the sinusoidal peak contained a minimal amount of deposit with the majority of the deposit being located beyond the peak.

Despite the limited amount of research conducted into the effect of a sinusoidal shaped wavy walled geometry on fouling layer formation, it is frequently used in production EGR heat exchangers.[67] This is because it is believed that the larger surface area of these coolers leads to an increased resistance to the negative effects of fouling. There is little to no published data that supports this assumption. Moreover, a review of studies on the effectiveness of various geometries at mitigating fouling found conflicting results to be common among them. By looking into the studies concerning the various geometries, the authors of the review concluded that the effect of the geometry on fouling layer development is not fully known and computational modeling is necessary to gain a complete understanding.[9]

Of the two computational studies concerning particle deposition in wavy walled EGR coolers, neither incorporated a model for the growth of the fouling layer. Both models also utilized perfectly adsorbing walls, leaving them unable to capture the effects of the fluid velocity and wall shear stress inhibiting particle deposition. Because of this, neither model is able to accurately capture particle deposition. This is apparent in the results Nagendra et al. obtained using their model, which showed the leading edge of the wall peak having the highest concentration of deposits.[69] This directly contradicts the observations on fouled coolers made by Lance et al. and indicates that a more robust computational model is necessary for modeling particle deposition and fouling layer growth.[67] Although other models discussed above incorporate models for particle attachment and removal and fouling layer growth, their use appears limited to a small range of parameter. Furthermore, none have been utilized to simulate the wavy-walled geometry.

1.2 Objectives

In spite of a significant amount of research that has been already performed to better understand the effects of wavy walled geometries on flow with heat and mass transport, we are still missing a fundamental and systematic insight into these processes especially in the case of EGR cooler fouling. This knowledge is critical for the efficient use of wavy walled channels in practical applications. The goal of this thesis, therefore, is to contribute to the understanding of the influence of asymmetric wavy walled channels on the flow, heat transfer and formation of a fouling layer within it. To achieve this goal, our research was split into these five objectives:

1. Develop and validate a finite-differences thermal model for simulating heat transfer and couple it with a lattice Boltzmann model for fluid flow.
2. Investigate influence of wavy wall geometry on the fluid flow through the channel.
3. Investigate the influence of the geometry on heat transfer in the fluid.
4. Expend the computational model for simulating fouling layer growth by integrating it with a Brownian dynamics model for the motion and deposition of particles entrained in the fluid.
5. Employ the extended model to examine the effect of the geometry on the fouling layer formation and development.

When investigating the effect of the geometry on the fluid flow, heat transfer and fouling layer development (objectives 2, 3, and 5, respectively), we systematically vary the parameters defining the geometry and flow in order to understand how they influence the various aspects of the system.

The insights gained from this research will have impacts not only in EGR heat exchanger design, but on a wide range of engineering applications. This includes mixing and heat transfer in microscale devices which are incapable of achieving turbulent mixing, as well as designing more efficient general purpose heat exchangers were fouling may or may not be a significant issue. Furthermore, our computational model will provide a more comprehensive understanding of the physics governing the fouling layer development as well as serve provide a computational framework that can be further expanded for use in future research.

1.3 Thesis Overview

A detailed description of the computational model developed when completing objectives 1 and 4 is provided in Chapter 2. Significant attention is given to the implementation of the methods used for simulating particle deposition and the fouling layer model. Additionally, a brief discussion of GPU computing, specifically the OpenCL® programming framework, is included as it became necessary for our code to utilize GPU accelerators to maintain reasonable simulation times for the computationally intensive simulations. To verify the implementation of the methods, we performed validation tests for the developed computational models. We have provided the results from these tests in Chapter 3.

Our investigations began by probing the effects of wavy walled channels on the fluid flow, which are detailed in Chapter 4. Specifically, we investigated how the flow occurring in the channel is influenced by the geometric parameters of the channel (i.e., the amplitude and period of the walls and height of the channel), and the pressure drop driving the flow. By performing simulations over a wide range of these parameters we were able to examine how they influence multiple aspects of the system. These aspects include the flow structures found in the fluid, the pressure drop necessary to induce unsteady flow, and the frictional losses resulting from the complex geometry. Additionally, we probed the effect of the geometry on the stability of the flow and the bifurcations the fluid undergoes as it transitions from laminar to chaotic flow regimes.

Chapter 5 focuses on the heat transfer enhancement induced by the wavy walled geometry (objective 3). We vary the geometric and flow parameters to observe how they

influence the heat transport in the channel. Using the local and mean Nusselt numbers, we compare how these parameters affect both the heat transfer occurring at various locations along the wall, as well as the overall heat transfer enhancement. Additionally, a thermal-hydraulic performance factor, which provided a more accurate representation of the overall performance, is used to quantify the effects of the geometry.

Using the full computational model, we conclude our investigation with the examination of the effect of the wavy walled geometry on the development of the fouling layer (objective 5). A discussion of our results is provided in Chapter 6. As in the previous investigations, we vary the geometric and flow parameters and observe how they influence the fouling of the channel. Specifically, we examine their effect on the thickness and growth rate of the fouling layer, the localization of the deposits, and the degradation of the cooler performance. Our results provide insights into how the wavy walled geometry influences the growth of the fouling layer.

Lastly, major conclusions drawn from our research are formulated in Chapter 7. This chapter also discusses further plans for continued model development and research.

CHAPTER 2. METHODOLOGY

In order to investigate the systems of interest, computational methods were needed to simulate the fluid flow, heat transfer and particle motion in the domain. The methods chosen for our computation model consisted of:

- The Lattice Boltzmann Method (LBM) for the fluid flow
- A finite-differences thermal model (FDTM) for the heat transfer
- A Brownian dynamics model (BDM) for the particle motion
- A custom fouling layer model (FLM) to capture the effect on the system of a growing fouling layer, resulting from particle deposition

This fouling layer model shifts the location of the surfaces defining the fluid-solid interface inward into the channel to simulate the growth of the fouling layer.

In the initial investigation of the fluid flow in the wavy channel, only the lattice Boltzmann method was utilized. Consequently, this required no coupling between methods. When investigating the heat transport, the finite-differences thermal solver was used in addition to the LBM. One way coupling between these two methods was implemented through the velocities calculated with the LBM. In the final investigation of the fouling layer formation, all four models (LBM, FDTM, BDM and FLM) were employed in each simulation. As before, one way coupling was applied between the LBM and FDTM using the fluid velocities. Similarly, the Brownian dynamics model was coupled with the LBM and FDTM through the velocities and temperatures used to calculate the particle trajectories, respectively. The BDM was linked to the fouling layer model

through the deposition of particles along the surface. In turn, the FLM directly influenced the LBM, FDTM and BDM by shifting the surface locations, changing the shape of the domain. With all four methods coupled either directly or indirectly (see Figure 2.1 for a diagram of these couplings), our computational model is able to capture the complex interactions between all aspects of the system.

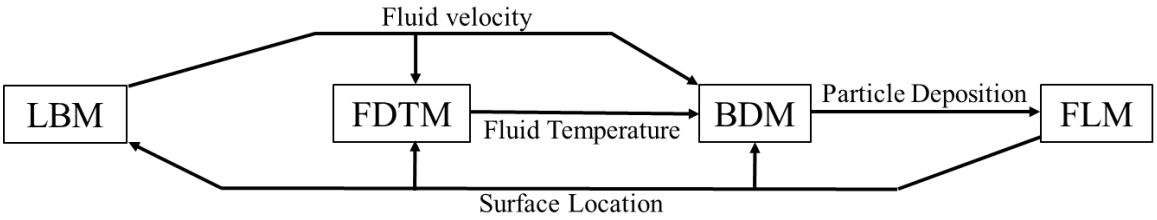

Figure 2.1 – Diagram of coupling between methods used in computational model.

Early developments of this computational model were written in C++ and simulations were executed on a compute cluster containing Intel Xeon multicore processors. During the development of the fouling layer model, all new methods along with nearly all those previously written in C++ were (re)implemented in the OpenCL™ framework (which is based on the C99 programming standard). The OpenCL™ framework provides the capability to execute on various computational devices, including graphics processing units (GPUs).[71] As such, simulations using methods implemented in OpenCL™ were executed on standard desktop computers containing AMD brand GPUs.

The following sections of this chapter will discuss the theory and implementation of the lattice Boltzmann method, the finite-differences thermal model, the Brownian dynamics model and the fouling layer model. A final section will provide a brief overview of the OpenCL™ framework along with a discussion of our model's implementation in the framework.

2.1 Lattice Boltzmann Method

In our model, we use the lattice Boltzmann method to model the fluid flow. The LBM is a mesoscopic method which uses the discrete Boltzmann equation to simulate flow of a Newtonian fluid instead of directly solving the Navier-Stokes equations.[72-74] The method uses a fixed square lattice and simple boundary conditions, which allow for modeling of complex geometries and eliminate the need for re-meshing with moving boundaries. Additionally, the spatial locality of the method make is relatively simple to implement and highly parallelizable.[75]

2.1.1 Historic overview of the LBM

Historically, the lattice Boltzmann method grew out of the lattice gas cellular automata (LGCA) models first introduced by Hardy, Pomeau, and de Pazzis in 1973.[76] Their model, called HPP, consisted of fictitious particles traveling along a fixed square lattice in four fixed directions corresponding to four velocities. When two or more particles occupy the same lattice site, they undergo collisions which enforce conservation of mass and momentum.[77] By undergoing successive transport and collision steps, the particles behave similar to molecules in a gas at a microscopic level. However, several flaws in the model left it incapable of simulating the flow of a fluid at the continuum level.[78]

In 1986 Frisch, Hasslacher and Pomeau published a paper detailing an improved LGCA method, known as FHP, which was capable of simulating fluid flows.[79] Rather than using a square lattice and four velocities, their model utilized a hexagonal lattice and six particle velocities. The higher symmetry of the FHP model allowed it to achieve the isotropy necessary to recover the Navier-Stokes equations in the macroscopic limit.[78]

Although this model and as subsequent LCGA models were able to overcome the initial limitations seen in early LCGA models, they still suffered from two notable disadvantages, a lack of Galilean invariance and statistical noise.[72]

The development of the lattice Boltzmann method grew directly out of attempts to overcome the drawbacks of LGCA methods. McNamara and Zanetti replaced the individual particles traveling along the lattice with ensemble averaged populations of particles in order to eliminate the issue of statistical noise.[80] Working independently, Higuera and Jimenez also did away with individual particles but went a step further by replacing the collision rules defining particle interactions with a linearized collision operator derived from the Boltzmann transport equation.[81] These two papers laid the ground work for what has become known as the lattice Boltzmann method.

Over the last three decades the method has been improved and new versions of the method have been developed. The earliest model, introduced by Quin and Chen et al, used the Bhatnagar-Gross-Krook collision operator to form a single relaxation time model known as the lattice BGK (LBGK) model.[82, 83] In order to overcome stability issues that occurred with small relaxation times and to improve accuracy, multi-relaxation time (MRT) and two relaxation time (TRT) models have been developed.[84-86] Others have extended the model to simulate a wide range of physical phenomena such as heat/mass transport and multiphase/multicomponent mixtures.[87-90] This development has led to the lattice Boltzmann method becoming a highly versatile and useful tool in the area of computational physics.

2.1.2 Implementation of the LBM

The lattice Boltzmann method simulates hydrodynamic flows using a density distribution function describing the motion of microscopic "fluid particles". The evolution of the distribution function proceeds through sequential collision and propagation steps and is governed by the discretized lattice Boltzmann equation given by:[73]

$$f_i\left(\mathbf{r}+\mathbf{c}_i\Delta t, t+\Delta t\right) = f_i\left(\mathbf{r},t\right)+\Omega\left[\mathrm{f}\left(\mathbf{r},t\right)\right] = f_i^* \tag{2.1}$$

In this equation, the local fluid distribution function $f_i(\mathbf{r},t)$ is propagated across each lattice direction, $\mathbf{c}_i$, at each time step, Δt. The collision operator $\Omega[\mathrm{f}(\mathbf{r},t)]$, which is a function of all f_i's at the lattice point, denoted $\mathrm{f}(\mathbf{r},t)$, relaxes the distribution function towards its local equilibrium. In our simulations we use a double relaxation time model developed by Ladd. The right hand side of Equation 2.1, denoted f_i^*, is the post-collision distribution which is calculated according to:[73]

$$f_i^* = a^{c_i}\left[\rho+\frac{\rho\mathbf{u}\cdot\mathbf{c}_i}{c_s^2}+\frac{\left(\rho\mathbf{uu}+\boldsymbol{\Pi}^{neq,*}\right):\left(\mathbf{c}_i\mathbf{c}_i-c_s^2\mathbf{1}\right)}{2c_s^4}\right] \tag{2.2}$$

Here, a^{c_i} is the lattice velocity, $c_s^2 = 1/3$ is the adiabatic speed of sound, $\rho = \sum f_i$ is the density, $\mathbf{u} = \sum f_i\mathbf{c}_i/\rho$ is the local fluid velocity, and $\boldsymbol{\Pi}^{neq,*}$ is the modified non equilibrium second moment given by:

$$\boldsymbol{\Pi}^{neq,*} = (1+\lambda)\bar{\boldsymbol{\Pi}}^{neq}+\frac{1}{3}(1+\lambda_v)\left(\boldsymbol{\Pi}^{neq}:\mathbf{1}\right)\mathbf{1} \tag{2.3}$$

Here λ and λ_v are eigenvalues of the linearized collision operator, $\mathbf{\Pi}^{neq} = \mathbf{\Pi} - \mathbf{\Pi}^{eq}$ is the non-equilibrium second moment, $\mathbf{\Pi} = \sum_i f_i \mathbf{c}_i \mathbf{c}_i$ is the second moment of the distribution function, $\mathbf{\Pi}^{eq} = \sum_i f_i^{eq} \mathbf{c}_i \mathbf{c}_i$ is the second moment of the equilibrium distribution given by:

$$f_i^{eq} = a^{c_i} \left[\rho + \frac{\rho \mathbf{u} \cdot \mathbf{c}_i}{c_s^2} + \frac{\rho \mathbf{uu} : \left(\mathbf{c}_i \mathbf{c}_i - c_s^2 \mathbf{1} \right)}{2c_s^4} \right] \tag{2.4}$$

The eigenvalues λ and λ_v are related to the shear and bulk dynamic viscosities according to: $\mu = -\rho c_s^2 \left(\lambda^{-1} + 0.5 \right)$ and $\mu_v = -\rho c_s^2 \left(2\lambda_v^{-1} + 1 \right) / 3$. The pressure is calculated from the equation of state, $p = \rho c_s^2$. In each simulation we used the density $\rho = 1$, $\lambda_v = -1$, and time step $\Delta t = 1$.

The lattice Boltzmann method is implemented on an equal-spaced square grid uniformly covering the computational domain. In our simulations, a 9 velocity model was used for two-dimensional simulations (D2Q9) with lattice velocities and corresponding are defined below.

$$\mathbf{c}_i = \begin{cases} (0,0), & i = 0, & a^{c_0} = 4/9 \\ (\pm 1, 0), (0, \pm 1), & i = 1-4, & a^{c_{1-4}} = 1/9 \\ (\pm 1, \pm 1), & i = 5-8, & a^{c_{5-8}} = 1/36 \end{cases} \tag{2.5}$$

The directions of the lattice velocities can be seen in Figure 2.2.

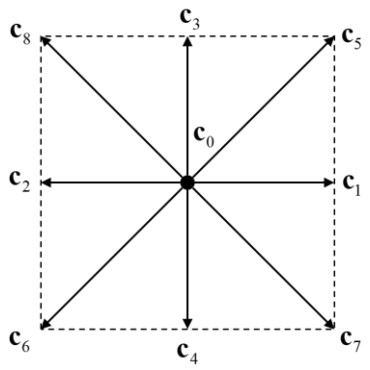

Figure 2.2 – Velocity directions for D2Q9 lattice.

2.1.3 Boundary Conditions and Determination of Boundary Nodes

For simple geometries, such as a straight channel, no-slip boundary conditions can be readily implemented using the half-way bounce back method. In this method, distributions that cross a solid boundary during propagation return to the same lattice site, but in the opposite direction. This method is second order accurate for boundaries located one half step from a lattice site, otherwise it is first order accurate.[91]

In complex geometries, such as the wavy channel considered in our study, the distance between the boundaries and the LBM nodes located next to the boundary varies. In this case, we used the interpolated bounce-back method introduced by Bouzidi et al.[92] to impose no slip boundaries along the channel walls, which maintains second order accuracy with minimal computational costs. The values for the "bounced back" distribution functions are interpolated according to:

$$f_{i'}\left(\mathbf{r}_l, t+\Delta t\right) = 2q f_i^c\left(\mathbf{r}_l, t\right) + \left(1-2q\right) f_i^c\left(\mathbf{r}_l - \mathbf{c}_i, t\right), \quad q < 0.5, \tag{2.6}$$

$$f_{i'}\left(\mathbf{r}_l, t+\Delta t\right) = \frac{1}{2q} f_i^c\left(\mathbf{r}_l, t\right) + \frac{2q-1}{2q} f_{i'}\left(\mathbf{r}_l, t\right), \quad q \geq 0.5. \tag{2.7}$$

Here, $f_{i'}$ is the distribution in the opposite direction relative to f_i, q is the distance between the lattice node and the wall, $\mathbf{r}_l$ is a fluid node with $\mathbf{r}_l + \mathbf{c}_i$ being a fictitious node located within solid, and f_i^c is the value taken after the collision, but before the propagation step. Figure 2.3 provides a schematic depicting how the method is implemented. When $q < 0.5$ (Figure 2.3 (a)), the value of a distribution is interpolated from nodes A and E for a fictitious node D. The location of D is chosen such that when the distribution is propagated a full step, it will bounce back at the wall (C) and reach node A. When $q \geq 0.5$ (Figure 2.3 (b)), the distribution leaving node A propagates a full step to the fictitious node D. The new value for the unknown distribution at A is then interpolated from the values at nodes D and E. In addition to no-slip boundaries along the wall, periodic boundary conditions are implemented along the inlet/outlet of the channel by transferring all distributions crossing the outlet (inlet) during propagation to the inlet (outlet).

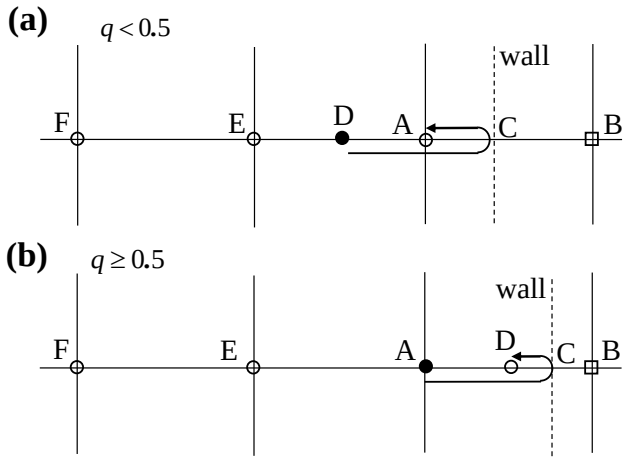

Figure 2.3 – Schematic of implementation of interpolated bounce-back method for (a) $q < 0.5$ and (b) $q \geq 0.5$.

The walls of the channel are delineated by set of n_p points spaced equidistantly across the length of the domain. Linking these points is a set of $n_{SE} = n_p - 2$ surface elements, each defined by two points. Using these surface elements, we are able to reduce the complex sinusoidal shape of the channel walls to a set linear line segments (see Figure 2.4).

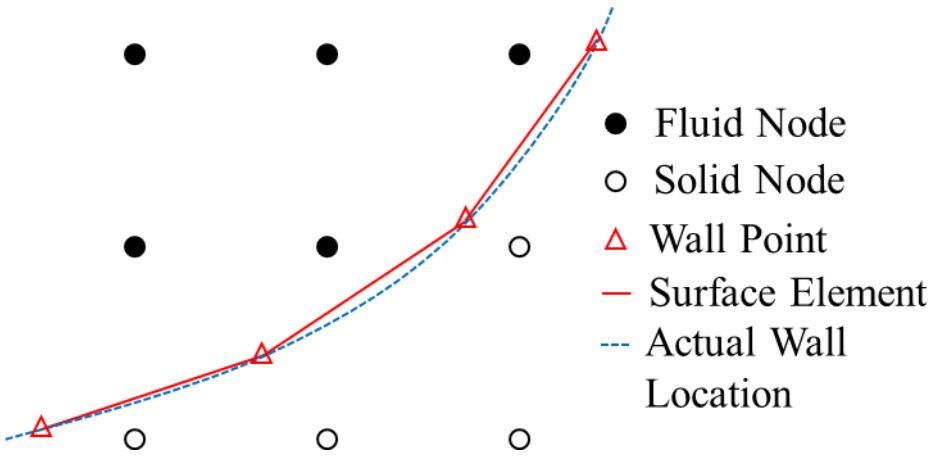

Figure 2.4 – Depiction of surface elements defining channel wall.

By defining the fluid-solid interface with a set of surface elements defined by two points, we can use simple geometrical relationships to obtain important information necessary for calculations. For example, the surface element information can be used to determine if a distribution at a given node crosses the wall and if it does, the distance between the surface and the node. This process is depicted in Figure 2.5, where the lattice velocity $\mathbf{c}_7$ at node $\mathbf{r}_l$ is crossing the surface is defined by points $\mathbf{p}_0$ and $\mathbf{p}_1$. First, using the vector $\mathbf{v}_{\mathbf{p}_0,\mathbf{p}_1} = \mathbf{p}_1 - \mathbf{p}_0$, the surface normal is calculated according to:

$$\hat{\mathbf{n}}_s = \frac{\left(-\mathbf{v}_{\mathbf{p}_0,\mathbf{p}_1}\hat{\mathbf{j}}, \mathbf{v}_{\mathbf{p}_0,\mathbf{p}_1}\hat{\mathbf{i}}\right)}{\left\|-\mathbf{v}_{\mathbf{p}_0,\mathbf{p}_1}\right\|}. \qquad 2.8$$

To ensure consistency, the $\mathbf{p}_0$ and $\mathbf{p}_1$ points defining each surface element are chosen in such a way that the normal calculated with Equation 2.8 will always point inward toward the fluid. Once the normal vector is obtained, the magnitude of vectors $\left\|\mathbf{v}_{\mathbf{r}_l,E}\right\| = \left|\mathbf{v}_{\mathbf{r}_l,\mathbf{p}_0} \cdot \hat{\mathbf{n}}_\mathbf{s}\right|$ and $\left\|\mathbf{v}_{\mathbf{r}_l,C}\right\| = \left|\mathbf{c}_7 \cdot \hat{\mathbf{n}}_\mathbf{s}\right|$ can be calculated. Lastly, because triangles ABC and ADE are similar, we can obtain the value of $q = \left\|\mathbf{v}_{\mathbf{r}_l,\mathrm{C}}\right\| / \left\|\mathbf{v}_{\mathbf{r}_l,E}\right\|$ for use in the interpolated bounce back method as well as the location of intersection $\mathbf{p}_{\text{int}} = \mathbf{r}_l + q\mathbf{c}_7$. Additionally, we can ensure that $\mathbf{p}_{\text{int}}$ is located on the surface element by testing if Equation 2.9 is satisfied.

$$\left\|\mathbf{v}_{\mathbf{p}_0,\mathbf{p}_1}\right\| = \left\|\mathbf{v}_{\mathbf{p}_0,\mathrm{D}}\right\| + \left\|\mathbf{v}_{\mathrm{D},\mathbf{p}_1}\right\| \tag{2.9}$$

If it is not satisfied, this indicates that $\mathbf{p}_{\text{int}}$ is located on the line passing through points $\mathbf{p}_0$ and $\mathbf{p}_1$, but outside of the section defined by them.

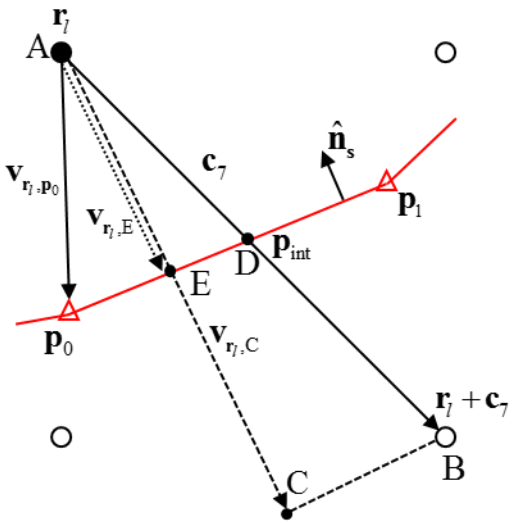

Figure 2.5 – Diagram representing calculation of distance between node and surface.

In addition to no-slip boundaries along the wall, a periodic boundary condition is implemented along the inlet/outlet of the channel. Coupled with the periodic boundary, a body force density $\mathbf{f}$ is applied to the momentum term in the collision operator leading to a modified flow momentum:[93]

$$\mathbf{j}' = \sum_i f_i \mathbf{c}_\mathbf{i} + \mathbf{f}/2 \,. \tag{2.10}$$

By setting $\mathbf{f} = -dp/dx\,\hat{\mathbf{i}}$, we were able to model flow driven by a constant pressure gradient. Additionally, using periodic conditions allowed us to simulate the sections of the channel sufficiently far downstream from the inlet for the flow to have fully developed. This is significantly more efficient than using pressure or velocity boundary conditions, which would require a simulation domain containing an entrance region full channel with multiple periods to allow the flow to became fully developed.

2.2 Finite Difference Thermal Model

An implicit finite-differences thermal model was used to model the temperature distribution within the channel. This method was used because of its simple implementation and computational efficiency.[94] The generalized form of the convection-diffusion equation for heat transfer in an incompressible fluid without heat generation is given by:[95]

$$\frac{\partial T}{\partial t} = \nabla \cdot \left(\alpha \nabla T \right) - \nabla \cdot \left(\mathbf{v} T \right), \tag{2.11}$$

where α is the thermal diffusivity, T is the temperature and $\mathbf{v}$ is the velocity of the fluid. Expanding the diffusion term (the first term on the right hand side of Equation 2.11) results in

$$\frac{\partial T}{\partial t} = \alpha \nabla^2 T + \nabla \alpha \cdot \nabla T - \nabla \cdot (\mathbf{v} T) \qquad 2.12$$

For systems with constant thermal diffusivity throughout the fluid, the second term on the right hand side of Equation 2.12 can be dropped as $\nabla \alpha = 0$. Removing this term, and expressing differential equation in its implicit form gives:

$$T^1(\mathbf{r}) = T^0(\mathbf{r}) + \Delta t \left[\alpha \left(\frac{\partial^2 T^1(\mathbf{r})}{\partial x^2} + \frac{\partial^2 T^1(\mathbf{r})}{\partial y^2} \right) + \left(U \frac{\partial T^1(\mathbf{r})}{\partial x} + V \frac{\partial T^1(\mathbf{r})}{\partial y} \right) \right]. \qquad 2.13$$

Here $T^0(\mathbf{r})$ and $T^1(\mathbf{r})$ are the temperatures at position $\mathbf{r}$ and times t and $t + \Delta t$ respectively, Δt is the time step, and U and V are the x and y components of the velocity. This form of the heat equation is used when investigating heat transfer in the channel without fouling as the thermal diffusivity of the fluid remains constant.

If the thermal diffusivity is variable in the system, its spatial derivative becomes non-zero cannot no be dropped from Equation 2.12. Therefore the following term must be included on the right hand side of Equation 2.13:

$$\Delta t \left[\frac{\partial \alpha(\mathbf{r})}{\partial x} \frac{\partial T^1(\mathbf{r})}{\partial x} + \frac{\partial \alpha(\mathbf{r})}{\partial y} \frac{\partial T^1(\mathbf{r})}{\partial y} \right], \qquad 2.14$$

where $\alpha(\mathbf{r})$ is the local thermal diffusivity. In all simulations the finite difference equations are solved on the same lattice as that used in the LBM.

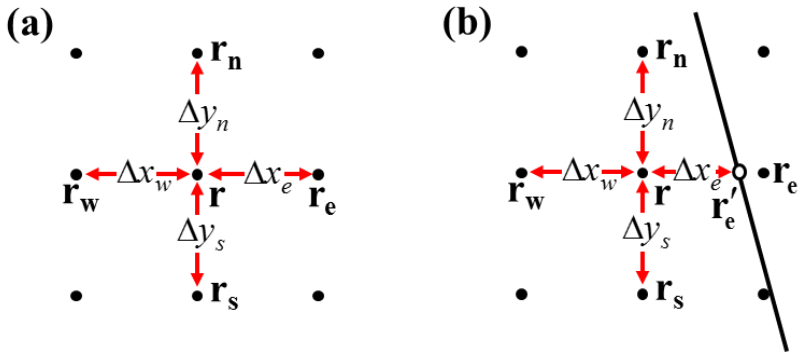

Figure 2.6 – Diagram of node spacing scheme used in finite differences thermal model. (a) Interior nodes have uniform spacing while (b) boundary nodes have non-uniform spacing.

2.2.1 Spatial Derivatives

A central difference scheme was used to calculate the spatial derivatives. Because of the complex geometry associated with the wavy walls, the first and second derivatives with respect to x were calculated according to:

$$\frac{\partial T^1(\mathbf{r})}{\partial x} = \frac{\Delta x_w T^1(\mathbf{r}_e)}{\Delta x_e(\Delta x_e + \Delta x_w)} - \frac{\Delta x_e T^1(\mathbf{r}_w)}{\Delta x_w(\Delta x_e + \Delta x_w)} + \frac{(\Delta x_e - \Delta x_w)T^1(\mathbf{r})}{\Delta x_e \Delta x_w} \qquad 2.15$$

$$\frac{\partial^2 T^1(\mathbf{r})}{\partial x^2} = \frac{2T^1(\mathbf{r}_e)}{\Delta x_e(\Delta x_e + \Delta x_w)} + \frac{2T^1(\mathbf{r}_w)}{\Delta x_w(\Delta x_e + \Delta x_w)} - \frac{2T^1(\mathbf{r})}{\Delta x_e \Delta x_w} \qquad 2.16$$

where Δx_e and Δx_w are the distances from the center node (at $\mathbf{r}$) to the east (at $\mathbf{r}_e$) and west (at $\mathbf{r}_w$) nodes, respectively (see Figure 2.6 for a visual representation of the node layout and spacing).[96] For nodes located away from the walls, where $\Delta x_e = \Delta x_w$ these two

equations reduce to the common central difference form. The derivatives in the y direction can be obtained by replacing the east and west nodes with the north and south nodes.

For the thermal diffusivity, rather than using its value at neighboring nodes to calculate the spatial derivatives, those representing the thermal diffusivities between nodes are used. Therefore, the spatial derivatives become:

$$\frac{\partial \alpha(\mathbf{r})}{\partial x} = \frac{2\Delta x_w \alpha(\mathbf{r}'_e)}{\Delta x_e(\Delta x_e + \Delta x_w)} - \frac{2\Delta x_e \alpha(\mathbf{r}'_w)}{\Delta x_w(\Delta x_e + \Delta x_w)} + \frac{2(\Delta x_e - \Delta x_w)\alpha(\mathbf{r})}{\Delta x_e \Delta x_w} \qquad 2.17$$

$$\frac{\partial^2 \alpha(\mathbf{r})}{\partial x^2} = \frac{4\alpha(\mathbf{r}'_e)}{\Delta x_e(\Delta x_e + \Delta x_w)} + \frac{4\alpha(\mathbf{r}'_w)}{\Delta x_w(\Delta x_e + \Delta x_w)} - \frac{4\alpha(\mathbf{r})}{\Delta x_e \Delta x_w}. \qquad 2.18$$

Here, $\alpha(\mathbf{r})$ is the thermal diffusivity at node $\mathbf{r}$, while $\mathbf{r}'_e$ and $\mathbf{r}'_w$ signify the locations halfway between node $\mathbf{r}$ and its neighboring in the east and west directions respectively. The value used for the thermal diffusivity at node $\mathbf{r}$ is obtained from the average of the diffusivities between nodes in the four surrounding directions. Note that the form Equations 2.17 and 2.18 differ from 2.15 and 2.16 by a factor of two due as they were derived from Taylor series expansions using a spacing of half the distance between nodes rather than the full distance. The derivatives in the y direction can be obtain in the same manner as discussed above for the temperature. Variable diffusivities are used when the fouling layer growth is included in the system and as such will be discussed in more detail in Section 2.4 of this chapter.

2.2.2 Boundary Conditions

The channel walls were kept at a constant temperature of $T_w = 0$ in all simulations. For simulations investigating heat transfer, periodic thermal boundary conditions were used at the inlet/outlet of the channel. This boundary condition is implemented by setting the dimensionless temperature to be periodic across the inlet/outlet.[97] The dimensionless temperature is defined by $\theta(\mathbf{r},t) = [T(\mathbf{r},t) - T_w]/[T_b(x) - T_w]$, where T_w is the temperature of the wall and $T_b(x)$ is the bulk temperature defined as:

$$T_b(x) = \frac{\int_z \int_y T(x,y,z)\|\mathbf{u}(x,y,z)\| dydz}{\int_z \int_y \|\mathbf{u}(x,y,z)\| dydz} = \frac{\sum_j \sum_k T(i,j,k)\|\mathbf{u}(i,j,k)\|}{\sum_j \sum_k \|\mathbf{u}(i,j,k)\|}. \qquad 2.19$$

In all simulations, the bulk mean temperature was set to $T_b(0) = 1$ at the inlet and was updated after each iteration of the implicit solver at the outlet. For simulations investigating fouling, a constant temperature boundary condition was implemented at the inlet with $T_w(0) = 1$ and the outlet temperature was extrapolated.[98]

2.2.3 Iterative Solver for System of Equations

When investigating heat transfer in wavy channels, the Gauss-Seidel method was used to iteratively solve the system of equations $\mathbf{AT} = \mathbf{b}$, where $\mathbf{A}$ is a $N \times N$ sparse matrix of coefficients, and $\mathbf{T}$ is a vectors with length N of the temperatures at each lattice node, $\mathbf{b}$ is a vector of constants with length N, and N is the total number of lattice sites in the domain. The Gauss-Seidel method was chosen for is simple implementation, reduced memory requirements compared to other iterative solvers as well as its increased rate of

convergence.[99] When modeling fouling layer development, the Jacobi method was utilized to iteratively solve the system of equations. The Jacobi method requires the storage of two $\mathbf{T}$ matrices, and has a slower rate of convergence compared to Gauss-Seidel. However, it can be parallelized, which was necessary as nearly all calculations performed in fouling simulations were done on GPU's.[99] This parallelization significantly reduced the time per iteration, overcoming the reduced rate of convergence of the method.

In order to reduce the memory required to hold the sparse matrix $\mathbf{A}$, only the values of the non-zero elements and their indices were stored, reducing the memory requirements from $O(N^2)$ to $O(N)$. Additionally, to reduce the computational cost of updating matrix $\mathbf{A}$ at each time step, the coefficients associated with the diffusive term in the transport equation are calculated once and stored in memory. This reduces the calculations performed at each time step to only updating the coefficients related to the convective term as they are a function of the unsteady velocity.

2.3 Brownian Dynamics Model

The sizes of diesel soot particles range from tens to hundreds of nanometers. This, coupled with the sufficiently small volume fraction of soot particles makes the Brownian dynamics model a suitable choice for simulating the particle motion and deposition.[100] In this model, the particles travel along trajectories that obey a stochastic-differential equation given by:[100, 101]

$$d\mathbf{r}(t) = \mathbf{u}(\mathbf{r}, t)dt + \sqrt{2D_0}\, d\mathbf{W}(t)\,. \qquad 2.20$$

The first term gives the advection due to the local fluid velocity $\mathbf{u}(\mathbf{r},t)$. The second term is the Brownian contribution, with D_0 being the particle diffusion coefficient and $d\mathbf{W}(t)$ being the differential of a Wiener process with unit variance.

We use a first order Euler method to solve Equation 2.20 which gives:[102]

$$\mathbf{r}(t+\Delta t) = \mathbf{r}(t) + \mathbf{u}[\mathbf{r}(t)]\Delta t + \sqrt{2D_0}\,\Delta\mathbf{W}(t). \qquad 2.21$$

Here, the increment $\Delta\mathbf{W}$ is sampled randomly from a truncated Gaussian distribution with unit variance. The fluid velocity at the particle position is obtained directly from the velocities at the LBM nodes by using linear interpolation between the neighboring nodes.[103]

2.3.1 Particle Properties

As the particle travel with the fluid, they are treated as tracers without mass or any excluded volume. Consequently, they do not experience inertial effects or particle-particle interactions, and do not induce any backflow effects on the fluid (only one way coupling). These assumptions are valid for sub-micron sized particles at a relatively low concentration, which are the conditions found in EGR heat exchangers.[102] When the particle is interacting with a surface, it maintains its lack of an excluded volume, but each particle is assigned a finite diameter that is used during interaction calculations. Additionally, this diameter is used when calculating the relevant particle properties.

To reduce computational costs, the particle diameters used in the model were divided into thirteen bins ranging from 50 nm to 290 nm, with each bin having a representative

mean diameter.[60] By doing so, the properties corresponding to each particle diameter were calculated once during initialization and stored in an array. Experimental investigations into the particle sizes found in diesel exhaust suggest that the particle diameters are log-normally distributed.[104] As such, number of particles in each bin was calculated from a lognormal distribution with a mean diameter of 130 nm and a standard deviation of 1.4.[60] A plot showing the percent of particles in each bin can be found in Figure 2.7.

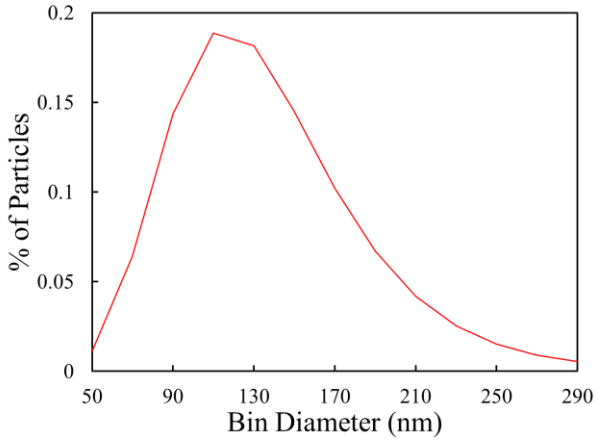

Figure 2.7 – Distribution of particle diameters used in Brownian dynamics method.

In physical EGR systems, the total number of particles within the cooler can reach numbers $>10^9$ and varies with time.[105] In our simulations, the number of particles is limited by its high computational costs. To increase computational efficiency and accuracy, the total number of Brownian particles is kept constant in the simulations. Moreover, each Brownian particle in the model represents multiple real particles. This allowed for our model to maintain a uniform concentration of particles entering the channel at the inlet in addition the ability to accurately simulate realistic concentrations of particles at a reasonable computational expense.

2.3.2 Thermophoretic Forces

Temperature gradients in the heat exchanger give rise to a thermophoretic force that drives particles toward the heat exchanger walls. The effects of the thermophoretic force is included into the model by adding a thermophoretic velocity to the particle velocity in Equation 2.21. This thermophoretic velocity is calculated from the Brock-Talbot correlation given by:[106]

$$V_T = -K_{th}\frac{\mu_g \nabla T}{\rho_g T_p} \tag{2.22}$$

where K_{th} is the thermophoretic coefficient, μ_g and ρ_g are the viscosity and density of the fluid, T_p is the temperature of the particle and ∇T is the temperature gradient in the fluid. Due to the small size of the particles, the particle temperature is assumed to be equal to the temperature of the fluid at that location. K_{th} is calculated according to:[107]

$$K_{th}\left(d_p\right) = \left(\frac{2C_s C_c\left(d_p\right)}{1+3C_m \mathrm{Kn}\left(d_p\right)}\right)\left(\frac{k_g/k_p + C_t \mathrm{Kn}\left(d_p\right)}{1+2k_g/k_p + 2C_t \mathrm{Kn}\left(d_p\right)}\right) \tag{2.23}$$

where $\mathrm{Kn}\left(d_p\right) = 2\lambda/d_p$ is the Knudsen number, λ is the mean free path for air, k_g and k_p are the thermal conductivities of the air and particles respectively, C_m is the momentum exchange coefficient, C_s is the thermal slip coefficient, C_t is a numerical factor obtained from kinetic theory, and C_c is the Cunningham slip correction factor is defined as:[108]

$$C_c(d_p) = 1 + \mathrm{Kn}\left(d_p\right)\left(A + Be^{-C/\mathrm{Kn}\left(d_p\right)}\right). \tag{2.24}$$

Here *A*, *B*, and *C* are experimentally determined coefficients. Values used for the coefficients C_m , C_s , C_t , *A*, *B*, and *C* are 1.14, 1.17, 2.18, 1.257, 0.4, and 1.1, respectively.[107, 109] The thermal conductivity of the particles was set to the experimentally determined value of $k_p = 0.057$ W/mK .[66]

The temperature and the velocity of each particle is obtained directly from the temperature and velocity at the four surrounding mesh nodes using bilinear interpolation. The temperature gradient is determined from the temperature difference between these nodes.

The effect of diffusion on particle motion is negligible compared to that of thermophoresis in systems with sufficiently large temperature gradients.[106] Because of this, we neglected the effects of diffusion in our model. We also note that simulating diffusion in a Brownian dynamics model requires the use of a random number generator capable of generating values from a normal distribution, which is a computationally expensive task.[110]

2.3.3 Particle Deposition and Removal Models

Experiments suggest that shear induced removal of deposits can have a significant impact on the growth of the fouling layer.[55] This can even lead to the layer thickness reaching a steady state as the increased fluid velocities caused by the narrowing of the channel result in the rate of removal offsetting the rate of deposition.[55] Higher flowrates also increase the kinetic energy of particles as they impact the wall. If this energy is sufficient to overcome the adhesive forces between the particle and the wall, the particle will rebound off the wall instead of depositing on it.[111] Therefore, in order to capture the

effect of the flowrate and wall shear on the deposition and removal of particles as they contact the surface, we implemented both a "sticking probability" and shear removal model.

2.3.3.1 Sticking Probability Model

"Sticking probability" models use the material properties of the surface and the impinging object as well as the kinetic energy of the object to calculate a probability that it will adhere to the surface.[112] In our model, the equation for the sticking probability, *Sp*, is given by:

$$Sp = \frac{Q_A}{m_p U_r^2 / 2} \tag{2.25}$$

which is the ratio of the adhesion energy acting to keep the particle at the surface to the kinetic energy of the rebounding particle (as depicted in Figure 2.8).[113]

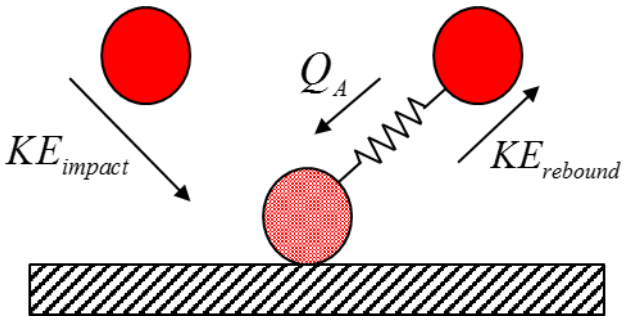

Figure 2.8 – Depiction of particle contacting surface.

Assuming no energy is lost to heat, the energy balance for the particle can be reduced to:[114]

$$\frac{m_p U_r^2}{2} = \frac{m_p U_c^2}{2} - Q'_A. \qquad 2.26$$

Here, m_p is the particle mass, U_r is the rebounding particle velocity, U_c is the velocity of the particle when it contacts the surface and Q'_A is the energy the particle must expend to break contact with the surface. This contact energy is given by:[115]

$$Q'_A = 7.09\left(\frac{\Gamma R^{*4}}{E_i^2}\right)^{1/3} \qquad 2.27$$

where $\Gamma = \sqrt{\gamma_p \gamma_s}$ is the work of adhesion, γ is the surface free energy with the subscripts *p* and *s* denoting the particle and surface, respectively, R^* is the effective radius of the particle when in contact with the surface which, assuming negligible deformation, is equal to the particle radius, and E_i is the effective Young's modulus of the particle-surface interface. The effective Young's modulus is a function of the Poisson's ratio, ν, and the Young's moduli of each material and is calculated from:[64]

$$E_i = \left(\frac{1-\nu_p^2}{E_p} + \frac{1-\nu_s^2}{E_s}\right)^{-1}. \qquad 2.28$$

When the particle is in contact with the surface, small deformations in both lead to the formation of a contact area rather than the single point of contact that would exist if no deformation occurred. Using the JKR theory of adhesive contact with zero contact pressure, the radius of this contact area, *a*, is given by:[64, 116]

$$a^3 = \frac{9\pi\Gamma d_p^2}{4E_i}. \qquad 2.29$$

Using this contact radius, the total interface adhesive energy, $Q_A = 2\Gamma\pi a^2$ can be calculated.

In all simulations the material properties used for the wall were those of stainless steel, as this material is commonly used for EGR heat exchangers walls.[117] Little information on the material properties of diesel soot particles is known. However, it is known that the graphite form of carbon is a major component of the soot. Therefore, the material properties of graphite were used.[118] The values used for the material properties are listed in Table 2.1. As the fouling layer forms, the particles begin to impact and make contact with soot deposits rather than the wall. To capture this change in the surface, once the thickness of the soot reaches 0.5 LB units, the material properties of graphite is used for the surface instead of those of stainless steel.

Table 2.1 – Values for material properties used in simulations.

	Soot (Graphite)	**Wall (Stainless Steel)**
Surface Free Energy	0.15 N/m	1.37 N/m
Young's Modulus	35 GPa	210 GPa
Poisson's Ratio	0.126	0.29

At each Brownian dynamics step, after the positions of the particles are updated, all particles located near the wall are checked to determine if their trajectories intersect with the wall. This is done in a manner similar to that used to calculate the distances in the interpolated bounce back method with the particle position before updating and the displacement vector of the particle replacing point $\mathbf{r}_l$ and vector $\mathbf{c}_7$, respectively. If the

particle trajectory intersects with a surface, the sticking probability is calculated. Additionally, a pseudo-random number generated from a uniform distribution of $x \in [0,1)$. If the random number is less than or equal to *Sp* or the rebound velocity $U_r \leq 0$, the particle deposits on the surface, otherwise it is specularly reflected from the surface with a velocity U_r , to a distance of $U_r \Delta t$. Here, Δt is the time step used in the Brownian dynamics method in LB units. When the particle rebounds, the new trajectory is examined in order to determine if it intersects with a different or the same surface and if it does the process is repeated.

2.3.3.2 Shear Removal Model

Initially, the deposition of particles is treated as temporary. It is during this temporary deposition period that the particles can be sheared from the surface and re-entrained in the flow. The length of the temporary deposition is sufficiently long to ensure that the deposited particle will experience the full range of the oscillating shear stress due to the unsteady flow at its deposit location before becoming permanent. This process is referred to as the shear removal model. In the shear removal model, the shear stress at the surface where the particle has deposited, τ_w , is compared to a critical shear stress, $\tau_{cr}\left(d_p\right)$ which is a function of the particle diameter.

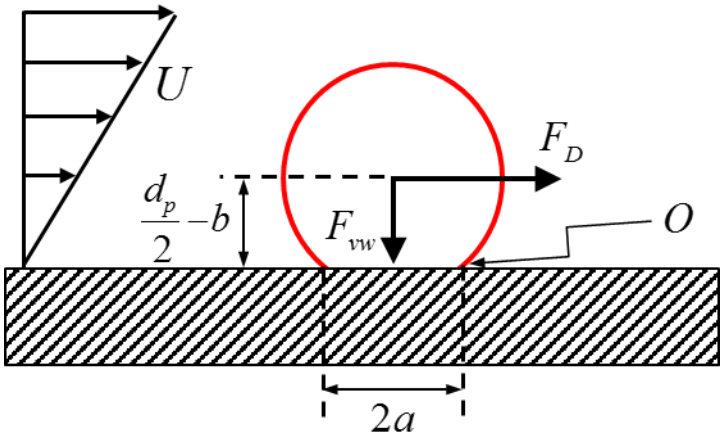

Figure 2.9 – Balance of moments on deposited particle.

The critical shear stress is calculated from a balance of moments acting on the particle at point *O* (see Figure 2.9). Drag from the fluid exerts a force on the particle directed parallel with the wall, while the Van der Waals force acts perpendicular to the wall surface. The weight of the particle and the lift force are both neglected as small compared to the adhesive Van der Waals force.[119] The drag force acting on the particle near the wall is calculated using Stokes' law with the wall correction term, $f = 1.7009$, given by:[120]

$$F_D = 3\pi\mu U d_p f \ . \qquad 2.30$$

Here, μ is the viscosity of the fluid, and *U* is the fluid velocity at the center of the particle. The Van der Waals force is defined as:

$$F_{vw} = \frac{A_H d_p}{12 z^2} \qquad 2.31$$

where $A_H = 10^{-20}$ J is the Hamaker's constant and $z = d_p/50$ is the separation distance between the particle and the surface.[8, 60]

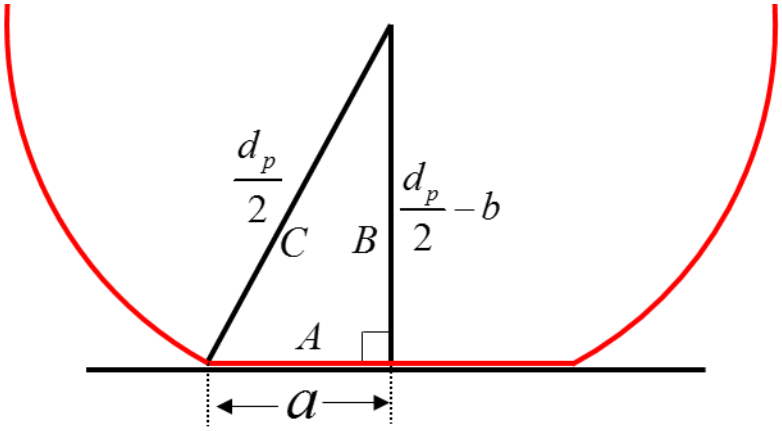

Figure 2.10 – Diagram of the particle deformation at the surface.

The particle will detach from the surface and be re-entrained in the flow provided the moment generated by F_D about point *O* (see Figure 2.9) is greater than that of F_{vw}. This is defined by the inequality:

$$F_D\left(\frac{d_p}{2} - b\right) > F_{vw}a\,. \tag{2.32}$$

Here, b is the distance the particle deforms when adhering to the surface and a is the contact radius defined in Equation 2.29. The shape of the deformed particle when adhered to the surface can be approximated as in Figure 2.10, with a right triangle formed between the center of the particle and the left and center locations of the contact line. Using the properties of the wall and particle defined above, we find that $a \approx 10^{-9}$ for a particle diameter of 100 nm. From the Pythagorean theorem, we can calculate the length of side *B* in Figure 2.10.

$$B = \sqrt{C^2 - A^2} = \sqrt{d_p^2/4 - a^2} \approx \sqrt{50^2 - 1^2} \approx 50\,\text{nm} \tag{2.33}$$

Therefore, since $B \approx d_p/2$, we can assume that $b \ll d_p$ and simplify Equation 2.32 to:

$$F_D d_p > 2F_{vw} a\,. \tag{2.34}$$

Due to the small particle sizes ($<1\mu m$), the velocity gradient across the height of the particle can be assumed linear. The velocity at the particle center is therefore given by:

$$U = \left(\frac{\partial U}{\partial n}\right)\frac{d_p}{2} \tag{2.35}$$

By combining Equations 2.30, 2.31, 2.34 and 2.35, and rearranging terms we obtain:

$$\mu\frac{\partial U}{\partial n} > \frac{1250 A_H a}{9\pi d_p^4 f}\,. \tag{2.36}$$

From this, we can define the critical shear stress as:

$$\tau_{cr}\left(d_p\right) = \frac{1250 A_H a}{9\pi d_p^4 f} = \frac{1250 A_H}{9\pi f}\left(\frac{9\pi\Gamma}{4 d_p^{10} E_i}\right)^{1/3}, \tag{2.37}$$

which describes the shear stress required to remove a particle of diameter d_p deposited on the wall.

In the lattice Boltzmann method, the i^{th} component of the wall shear stress vector at a given lattice node located at the boundary (i.e. has one or more distributions crossing the boundary) is given by:[121]

$$\tau_{w,i} = \frac{-\mu}{c_s^2 \rho\lambda} f_\alpha^{neq} c_{\alpha j} n_j \left(c_{\alpha i} - c_{\alpha i} n_i n_k\right). \tag{2.38}$$

Here, ρ is the fluid density, λ is the LBM relaxation parameter, c_s^2 is the lattice speed of sound, $f_\alpha^{neq} = f_\alpha - f_\alpha^{eq}$ is the non-equilibrium value of distribution α, and $c_{\alpha x}$ and n_x denote the components of the lattice vector $\mathbf{c}_\alpha$ and normal vector $\hat{\mathbf{n}}_b$ respectively (with x representing Einstein notation indices i, j, and k). Figure 2.11 provides a visual representation of the elements used in the shear stress calculations. As discussed previously, the normal vector at each surface element is well defined and can be readily calculated from its position information (solid red arrows in Figure 2.11). The vectors located at the boundary nodes normal to the surface, however, are ambiguous as a boundary node can be positioned near more than one surface element with different normal directions. In order to define the normal vector at these nodes, an average of the normal vectors of all surface elements neighboring the node is calculated according to:[121]

$$\mathbf{n}_b = \frac{1}{n_s} \sum_{n_s} \hat{\mathbf{n}}_s \,. \tag{2.39}$$

Here, n_s is the number of neighboring surface elements, $\hat{\mathbf{n}}_s$ is the unit normal of each neighboring surface. We define a neighboring surface element as any surface element located within a circle of radius, R_{nn}, around the boundary node (black circle centered on the fluid node in Figure 2.11). By normalizing $\mathbf{n}_b$ we obtain $\hat{\mathbf{n}}_b$ (black short-dashed arrow in Figure 2.11) used in Equation 2.38 to calculate the wall shear stress at the boundary node.

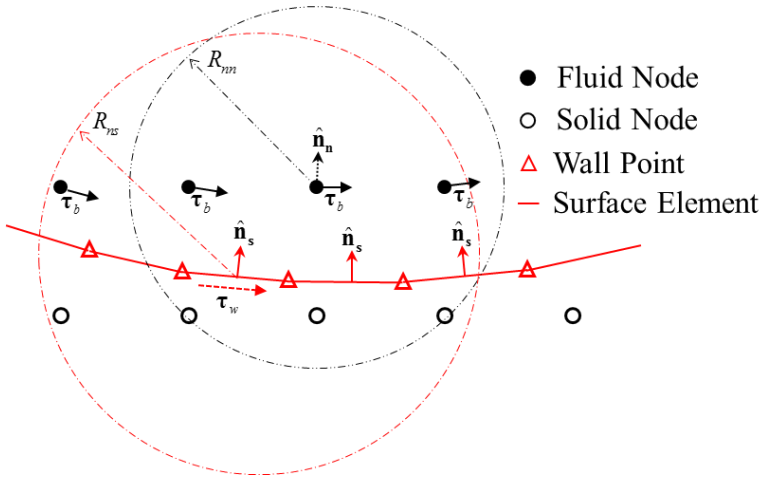

Figure 2.11 – Diagram depicting elements used in calculation of shear stress along the wall.

Using the shear stress values at the boundary nodes, the magnitude of the shear stress at each surface element can be determined. This is done by taking a weighted average of the shear stress magnitudes of the all boundary nodes neighboring a given surface element using the equation:

$$\tau_w = \left(\sum_i W_i \right) \sum_i W_i \left\| \boldsymbol{\tau}_b \right\| \qquad 2.40$$

Again, the neighboring nodes are defined as any node located within a circle of radius, R_{ns}, around the midpoint of the surface element (the red circle centered around the surface element in Figure 2.11). The weights, W_i, are calculated from the triweight kernel function given by:[122]

$$W_i(\bar{r}) = \frac{35}{32}\left(1-\bar{r}^2\right)^3 \mathbf{1}_{\{|\bar{r}|\le 1\}}. \qquad 2.41$$

Here, $\bar{r} = r/R_{ns}$ is the normalized distance between the surface midpoint and the boundary node, and $\mathbf{1}_{\{|\bar{r}|\leq 1\}}$ is the indicator function. This kernel function was chosen for its steep slope which heavily favors nodes near the given surface. Rather than calculating the direction of the shear stress vector, it is assumed to act tangentially to the surface (the red dashed arrow in Figure 2.11).

Once the shear stress is calculated for a given surface element, it can be compared to the critical shear stress for all particles temporarily deposited on it to determine if any particles are sheared from the surface. When a particle experiences sufficient shear stresses to be removed from the surface, an acceleration for the particle and its resulting displacement are calculated. The fluid induces two forces on the particle as it is dislodged from the surface, a drag force and a lift force acting in the tangential and normal directions to the surface, respectively. The drag force, as discussed previously, is calculated from the shear stress at the surface according to:

$$F_D = \frac{3\pi}{2} d_p^2 f \tau_w . \qquad 2.42$$

The lift force can be calculated from the expression developed by Leighton and Acrivos for the lift induced by shear flow over a spherical particle on a plane given by:[123]

$$F_L = 0.57 \rho d_p^4 \dot{\gamma}^2 . \qquad 2.43$$

Here, $\dot{\gamma} = \tau_w / \mu$ is the strain rate at the wall. From these two forces, the resultant force acting on the particle defined by the vector:

$$\mathbf{F}_R = F_D \operatorname{sgn}(\boldsymbol{\tau}_w \cdot \hat{\mathbf{t}}_\mathbf{s}) \hat{\mathbf{t}}_\mathbf{s} + F_L \hat{\mathbf{n}}_\mathbf{s}, \tag{2.44}$$

where $\hat{\mathbf{n}}_\mathbf{s}$ and $\hat{\mathbf{t}}_\mathbf{s}$ are the normal and tangential unit vectors defining the surface, and $\operatorname{sgn}(\boldsymbol{\tau}_w \cdot \hat{\mathbf{t}}_\mathbf{s})$ is the signum function which ensures that the drag force acts in the same direction as the shear stress.

The forces induced by the flow acting on the particle induce an acceleration, $\mathbf{a}_p = \mathbf{F}_R / m_p$, where $m_p = \pi d_p^3 \rho_p / 6$ is the mass of the particle with $\rho_p = 1770\,\mathrm{kg/m^3}$ used for the density of the particle.[66] Assuming the particle detaches at the beginning of the Brownian dynamics step and undergoes a constant acceleration throughout the entire time step, the location of the particle after it is removed from the surface is given by:

$$\mathbf{r}(t + \Delta t) = \mathbf{r}(t) + 0.5 \mathbf{a}_p (\Delta t)^2. \tag{2.45}$$

Here, $\mathbf{r}(t)$ is taken as the location where the particle first deposited on the surface.

After a set number of time steps, if the particle is still adhered to the surface it is assumed to be permanently deposited. When this occurs, the number of soot particles represented by the individual Brownian particle is added to the appropriate element of an array tracking the number of particles from each particle size bin deposited at each surface element. After the necessary information is stored, the Brownian particle is re-released at the inlet.

2.3.4 Inlet Boundary Conditions

Along with the particles that have permanently deposited on the surface, all particles reaching the outlet of the channel are removed from the simulation domain. After a set number of time steps, these removed particles are re-introduced in the computational domain at the inlet of the channel. This ensures that the total number of Brownian particles used in the model remains constant. The number of real particles represented by each Brownian particle re-released at the inlet is set at a value which enforces a uniform particle concentration in the entering fluid. The representative number of particles, denoted n_{rp}, is calculated according to:

$$n_{rp} = \frac{2C_p U_m h \Delta t_{rr}}{n_{bp}}, \tag{2.46}$$

where C_p is the particle concentration (with units $\#_{\text{particles}} / \Delta x^2$), U_m is the mean velocity of the fluid at the inlet, h is half the height of the channel, Δt_{rr} is the time between particle releases and n_{bp} is the number of Brownian particles being re-introduced.

Random numbers are generated in order to determine the location along the inlet at which a given Brownian particle is released as well as the diameter assigned to that particle. For the particle location, rejection sampling is used to generate a pseudo-random number from a probability distribution shaped like the velocity distribution at the inlet. The algorithm is implemented as follows:

1) Generate two random numbers, y_{rng} and u_{rng}, from uniform distributions $\left(y_{bottom}(t), y_{top}(t)\right)$ and $\left[0, U_{\max}(t)\right]$, respectively. Here, $y_{bottom}(t)$ and $y_{top}(t)$ are the y-locations of the bottom and top wall at the inlet at time t and $U_{\max}(t)$ is the maximum velocity at the inlet at time t.
2) Calculate $U_{inlet}\left(y_{rng}\right)$ by interpolating between velocities at the neighboring inlet nodes.
3) If $U_{inlet}\left(y_{rng}\right) \le u_{rng}$, the value of y_{rng} is accepted and the algorithm is complete. Otherwise, the value is rejected and the algorithm restarts at step 1.

The value of y_{rng} is subsequently used for the y position of the particle being released.

For the selection of the particle diameter, rejection sampling was also utilized (with a lognormal distribution being used in place of the velocity distribution). Additionally, because a discrete set of diameters is used to the represent a continuous range of diameter values, the number generated is rounded to fall within the discrete set of sizes. This process is repeated for all Brownian particles. With the representative number of particles, the location of release and the diameter known, the Brownian particle is ready to be released.

2.4 Fouling Model

The formation of a deposit layer along the walls of the heat exchanger has a significant impact on all aspects of the system.[9] As the thickness of the layer grows, the effective height of the channel decreases. This affects the flow by inducing higher fluid velocities leading to higher shear stresses at the surface.[55, 57] The high porosity of the layer

(~98%) allows for it to act as a highly effective thermal insulator.[65] This reduces the effectiveness of the cooler, reducing the temperature gradients in the fluid. In turn, the increased shear stresses and the decreased temperature gradients will influence the motion of particles entrained in the fluid as well as the continuing development of the fouling layer.[63] These are a few examples of the many, interconnected effects resulting from the development of the fouling layer. Because of this, in order to accurately model the fluid flow, heat transfer and particle motion/deposition in an EGR heat exchanger, a method to capture the growth of the fouling layer is a necessary addition.

Our fouling layer model consists of two steps: a shift step and an update step. In the shift step, the location of the surface elements defining fluid-solid interface are shifted to simulate the growth of the layer. The distance each element is shifted is proportional to the number of particles that have deposited on that surface since the last shift. With the location of the fluid-solid interface moved, the update step corrects the variables describing fouling layer to reflect the change in the fouling layer thickness. This update step ensures the fluid flow, heat transfer and particle motion are coupled to the growth of the fouling layer.

The model includes several computationally expensive calculations. Because of this, and the fact that relatively few Brownian particles deposit on the surface each time step, the two fouling layer steps are performed after a set number of simulation time steps rather than after each time step. The number of time steps selected for this update interval is chosen to achieve a maximum of $\sim 5\%$ of the lattice spacing for the distance the surface elements are shifted. This ensures that distances are small enough that the re-positioning of the surface can be treated as a quasi-static process.

2.4.1 Surface Relocation in Shift Step

In the shift step, the amount of growth of the layer is calculated and the boundary points are re-positioned to reflect the growth. At each boundary point, a weighted average of the particles deposited along the neighboring surface elements is calculated for each of the representative diameters. Here, the set of neighboring surface elements is defined as those with center points falling within a defined radius, R_{bp}, from the boundary point. The weight applied to each value is determined from the distance between the boundary point and the center of the corresponding surface element using a Gaussian kernel. An area of the deposit is calculated from the number of particles according to:

$$V_d = \sum_{i=1}^{N_d} \frac{\bar{n}\left(d_{p,i}\right)\pi d_{p,i}^2}{4(1-\phi)} \ , \qquad 2.47$$

where N_d is the number of representative particle diameters, $\bar{n}\left(d_{p,i}\right)$ weighted average of deposited particles for a given diameter, $d_{p,i}$ is the representative diameter and ϕ is the porosity of the soot. Dividing the area by the length of the distance between the midpoints of the surfaces to the left and right of the boundary point provides the thickness of the deposited particles. The boundary point is displaced a distance equal to this thickness. For every boundary point, its location is shifted in the same direction each time the update step is performed. This direction is calculated from the average of the initial (normalized) normal vectors defining the orientation of the surface elements to the left and right of the boundary point.

2.4.2 Lattice Boltzmann Update Step

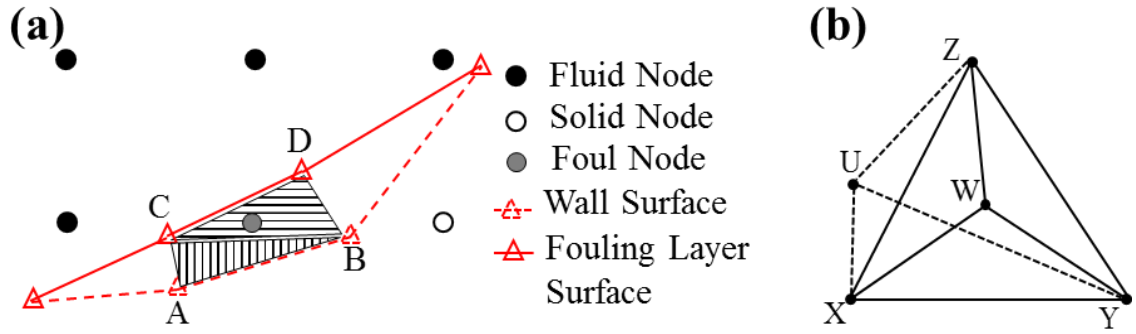

Figure 2.12 – Illustrations of update process for lattice Boltzmann method showing (a) process of locating node in the fouling layer and (b) geometric method of determining if a point is located inside of a given triangle.

After the location of the surface is updated to reflect the growth of the fouling layer, several updates need to be performed. This will ensure that the new thickness is accurately reflected in the three other computational methods. The update step starts with the lattice Boltzmann method variables. As particles deposit along the wall, a portion of the lattice nodes initially located inside the fluid region of the domain will begin to fall within the solid fouling layer. An illustration of the method used to determine if a lattice node is located within the fouling layer provided in Figure 2.12(a). In this process, the area between the initial and current locations of the surface element, which is a section of the fouling layer, is divided into two triangles (designated triangles ABC and BCD in Figure 2.12(a)). By testing if any lattice node located in the vicinity of the surface element is located within the tested, any node falling within this section of fouling layer can be determined (shown in Figure 2.12(a) with the foul node located inside of triangle BCD).

A simple method which is commonly utilized in computer graphics calculations is used to test if a point is located within a triangle. The method includes the following steps:

1) Form three triangles from the vertices of the triangle of interest and the point being tested (triangles XYW, YZW, XZW in Figure 2.12(b)).
2) For each of the four triangles (the triangle of interest and the three formed in previous step), subtract the position of one vertex from that of the other two to obtain two vectors defining each triangle (i.e., the vectors $\bar{\mathbf{v}}_{XY}$ and $\bar{\mathbf{v}}_{XW}$ define the triangle XYW in Figure 2.12(b)).
3) Calculate the area of each triangle by taking the magnitude of the cross product of the two vectors and dividing by two.
4) Subtract the areas of the three triangles found in step one from the area of the triangle of interest. If the difference is zero, the points resides within the triangle, otherwise it is outside.

Using the points U and W in Figure 2.12(b) as an example it can be seen that triangles XYW, YZW, XZW formed with point W are equal in area with the triangle XYZ as point W is located inside of the triangle. The triangles XYU, YZU, XZU formed with the point U, however, have a total area greater than that of the triangle XYZ as the point U is positioned outside of XYZ.

All nodes positioned in the fouling layer are considered as solid nodes. Therefore, the collision step will no longer be performed at it, and all distributions that previously propagated to the node during the propagation step will be bounced back from the fouling layer surface. Once the surface of the fouling layer is repositioned, the information used in the interpolated bounce back method must be updated to reflect the new position of the

boundary as well as the newly converted fouling layer nodes. This is done using the methods discussed in Section 2.1.3.

2.4.3 Finite Difference Thermal Model Update Step

Unlike in the lattice Boltzmann method, the temperature continues to be solved for at all nodes including those inside the fouling layer located within the channel using the finite-differences thermal model. In order to capture the effect of the fouling layer growth in this model, the thermal conductivity at nodes near and inside of the layer is varied to reflect the effective thermal properties. As such, the finite difference equation used in the thermal model includes an additional term provided in Equation 2.14 to capture the effects of a variable thermal diffusivity.

Due to its high porosity (~98%), the fouling layer consists mostly of air. Consequently the thermal conductivity and the heat capacity of the layer ($0.057\ \mathrm{W/mK}$ and $0.867\ \mathrm{J/gK}$, respectively) are similar to that of air ($0.0421\ \mathrm{W/mK}$ and $1.034\ \mathrm{J/gK}$, respectively). The density of the layer, however, is significantly larger than that of air (35 and $0.675\ \mathrm{kg/m^3}$, respectively).[66, 124] This is due to the individual soot particles having densities of $1800\ \mathrm{kg/m^3}$, which contribute significant mass to the layer even at this small volume fraction.[125] The considerable difference in their densities leads to the thermal diffusivity varying from $0.0602\ \mathrm{m^2/s}$ in the gas to $1.58\times10^{-3}\ \mathrm{m^2/s}$ in the fouling layer. Because of this considerable difference, the heat transfer occurring between a point in the fluid and a point in the fouling layer depends heavily on the exact location of the surface

between them. Therefore, in order to accurately capture the effect of the fouling layer, the location of its surface between nodes must be carefully considered.

As discussed in Subsection 2.2.2, the spatial derivative of the thermal diffusivity utilizes values representing the diffusivity between the given node and its neighbors. For nodes with neighbors positioned across the fouling layer surface, the distance from the node to the surface is incorporated in the calculation of this representative thermal diffusivity. This allows for the model to capture the thickness of the layer with more detail than would be possible if only a binary diffusivity of the fluid or fouling values are used. In order to determine the representative diffusivity, a thermal conductivity, density and heat capacity are calculated as a function of the distance between the node of interest and the surface, denoted δ (normalized by the spacing between the nodes). From these three values the representative thermal diffusivity is calculated according to:

$$\alpha\left(\mathbf{r}_n'\right) = \frac{\kappa\left(\delta\right)}{\rho\left(\delta\right)c_p\left(\delta\right)}, \tag{2.48}$$

where $\mathbf{r}_n'$ represents the value between the node and its neighbor in any direction $\mathbf{r}_n$, and κ, ρ and c_p are the thermal conductivity, density and specific heat, respectively.

The equation for the thermal conductivity can be obtained from an energy balance at the surface and is given by:[95]

$$\kappa\left(\delta\right) = \left(\frac{\delta}{\kappa\left(\mathbf{r}\right)} + \frac{1-\delta}{\kappa\left(\mathbf{r}_n\right)}\right)^{-1}, \tag{2.49}$$

The values for the density and the specific heat can be obtain from a linear variation between the values at the two nodes. For the density, this is:

$$\rho(\delta) = \rho(\mathbf{r})\delta + \rho(\mathbf{r}_n)(1-\delta), \qquad 2.50$$

while the specific heat can be calculated using the above equation with c_p replacing ρ.

This method is similar to the conjugate heat transfer method described by Patankar, which utilizes a single conservation expression for both the fluid and solid domains with the thermal conductivity at the interface calculated according to Equation 2.49.[95] This allows for the temperature to be solved across the entire domain without the need for coupling temperatures and fluxes across the interface.[126]

During the update step for the thermal model, the representative thermal diffusivities are calculated for the four neighboring directions of every node. If the surface of the fouling layer is crossed in a given direction between the node and its neighbor, the diffusivity for that direction is calculated from the above equations. Otherwise the diffusivity corresponding to the state of the node (either fluid or fouling layer) is assigned to that direction. Once these four diffusivities are known, the diffusivity of the node is calculated by averaging the four values. A process similar to that used to determine the locations of the boundary nodes and calculate their distance from the wall discussed in Section 2.1.3 is utilized when calculating the thermal diffusivities.

2.4.4 Brownian Dynamics Model Update Step

When the surface elements are shifted to mimic a growing fouling layer, a portion of the Brownian particles located close to the previous position of the boundary will be "swallowed" by the fouling layer as it grows (i.e. they will end up located inside the fouling layer). This "swallowing" of particles introduces two issues. The first is that if left unaddressed, it will introduce errors in the computational method which can lead to incorrect results. The errors would be the result of the "swallowed" particles being positioned inside the layer after it is updated. For the Brownian dynamics model, particles near the wall are tested to see if they cross the surface boundary when updated. If they are located inside the layer before being updated, they will not cross the surface and therefore can travel out of the domain which can induce unknown errors. The other issue that arises is that it introduces an unphysical aspect to the model. This unphysical behavior of particles being "swallowed" by the layer is a result of its discretized growth and would not occur with the continuous growth of the layer in a real system.

Three possible methods exist to mitigate the unphysical effects of the discretized growth causing particles to be swallowed as well as avoid computational errors. One approach is to remove the particles that have been swallowed and re-release them at the inlet. This addresses the errors, but results in particles near the surface that may soon deposit nearby no longer having an opportunity to deposit. This would not be an accurate model of a real system, and therefore is not a valid solution to the problem. The second method would treat any particle "swallowed" by the fouling layer as though it had deposited, before being re-released at the inlet. Again this addresses the computational errors, and provides a more accurate solution than the first method, as most of these

particles would deposit nearby within a few time steps. However, this nearby location may not be the same surface element it is currently beside, and the shear stress may be sufficiently high for some larger particles to not be able to deposit in the normal process.

Figure 2.13 – Illustration of particle relocation process.

We therefore use the third method that re-locates the particles "swallowed" by the fouling layer to a new position so they remain in the fluid near the wall after the surface is shifted. The following steps define the process applied to each particle in order to determine its new position:

1) Determine the surface located closest to particle before being shifted (the left surface in Figure 2.13).
2) Determine the vector between the un-shifted surface and the particle oriented normal to the surface (the vector $\mathbf{v}_n$ in Figure 2.13).
3) Calculate the distance from the left end of the surface to the vector found in step two, and the total length of the un-shifted surface element (L_p and L_{se} in Figure 2.13, respectively).

4) Calculate the distance from the left end of the shifted surface the new particle displacement vector will be placed by multiplying the ratio of the distances found in step 3 by the new length of the surface element (L_p' in Figure 2.13).

5) Determine the new particle position by displacing it from the location found in step 4 by a vector which oriented normal to the shifted surface with a length equal to that of the vector found in step 2 (the vector $\mathbf{v_n'}$ in Figure 2.13).

This method of dealing with the "swallowed" particles ensures that they remain near the surface for deposition to occur given the necessary conditions are met, while not forcing particles to deposit that would not be able to otherwise. Unlike the first two methods, however, in certain corner cases a particle may remain inside the fouling layer after relocation. The frequency at which this occurs is sufficiently low that any particle remaining in the fouling layer can be removed and re-released at the inlet without influencing the results. Despite the additional computational effort required to reposition the particles and test for any remaining in the fouling layer afterward, this method is best suited for mitigating the effects of the discretized fouling layer growth. As such, it is utilized in the Brownian dynamics model update step of the fouling layer model.

Along with addressing the particles "swallowed" by the fouling layer, the information used in calculating the shear stresses along the surface must be updated to reflect the new surface position. This update consists of repeating the same process as that used when initializing the information discussed in Section 2.3.3.2. Additionally, the implementation of the Brownian dynamics model requires a significant amount of stored information to couple it to the three other models and simulate a considerable number of

particles in an optimized manner. As a result, a large portion of this information must be updated to reflect the new surface location, all of which is done during this portion of the update step.

2.5 GPU Computing

During the collision step in the lattice Boltzmann method (the most computationally expensive step), the distributions at a given lattice site is updated from the current values of the distributions at that site. In the Brownian dynamics model, because interactions between particles and the effect of particles on the flow are neglected, at each time step, the particles can be updated independently of one another. Because of the localized nature of these two methods, significant performance gains can be achieved by performing them in parallel. Additionally, by utilizing a Jacobi method to solve the system of equations in parallel, modest gains in performance can be obtained in the finite-differences thermal model as well. With these three methods capable of improved performance when parallelized, they are well suited to exploit the large number of cores found in graphics processing units (GPUs).[127]

The advantage GPUs have over CPUs in performing computational physics calculations lies in its architectural differences. Modern CPUs need to be able to handle a wide range of tasks, most of which can be performed sequentially. As a result, they are designed with a few high power cores and are optimized for general purpose computing. Modern GPUs, on the other hand, are designed for very specific tasks involved in computer graphics which must be performed at substantial rates. GPUs are therefore designed with a large amount of simple processing cores each performing basic calculations all in parallel.

By reducing instruction fetching overhead using a method known as the single instruction multiple threads (SIMT) execution model, the GPU is able to hide latencies associated with memory access operations. This ensures consistently high utilization of every core, making the GPUs well suited for physics simulations when parallelizable methods are used.[127]

Due to the significant architectural differences, computational code written for execution on a CPU, especially when written in a low level language like C or C++, cannot be run on a GPU. As a result, code must be developed specifically for execution on the GPU (or, more generally, written for execution on a heterogeneous platform). Additionally, when compared with the progress made in programming on CPUs, development of GPU programming (often referred to as general purpose GPU or GPGPU programming) is still in its infancy. However, because of the substantial performance gains possible with their use, many methods (including frameworks, languages, standards, models, etc.) are being developed to reduce the complexity of GPGPU programming. From these, two have emerged as dominant: CUDA® and OpenCL™. CUDA® is a proprietary programming model developed by NVIDIA.[128] Although considered the most mature of all GPGPU programming methods, CUDA® can only be executed on NVIDIA GPUs, drastically reducing the selection of hardware that can be used for computations. OpenCL™ is an open source framework supported maintained by the non-profit consortium Khronos Group.[71] It is supported by a wide range of hardware manufacturers including both NVIDIA and AMD (the two largest GPU makers). Because of this, we chose to use OpenCL™ as our GPGPU programming method. In the following subsections we provide a short introduction to the OpenCL framework as well as a brief description of two open source OpenCL libraries utilized in our computational methods.

2.5.1 The OpenCL Programming Framework

The Open Computing Language, more commonly known as OpenCL™, is an open source framework for writing code capable of execution on various types of computational hardware devices. Although commonly used for GPU programming, software developed with OpenCL™ is capable of executing on CPUs, digital signal processors (DSPs), field programmable gate arrays (FPGAs) and other parallel computing "accelerators". The framework consists of a programming language and an application programming interface (API). The programming language is used to write code to be executed on the GPU, FPGA, etc. (referred to as a "device") and the API provides the "host" the ability to handle memory management and code execution on the device.

```
void Matrix_Mul(double* A, double* B, double* C,
 int M, int N, int P)

for( int i = 0; i < M; i++ )
{
        for( int j = 0; j < P; j++ )
        {
                double sum = 0;
                for( int k = 0; k < N; k++ )
                        sum += A[ i + k * M ] * B[ k + j * N ];
                 C[ i + j * M ] = sum;
        }
}
```

```
__kernel void Matrix_Mul(__global double* A,
        __global double* B, __global double* C,
        int M, int N, int P)
{
        int i = get_global_id(0);
        int j = get_global_id(1);

        double sum = 0;

        for( int k = 0; k < N; k++ )
                sum += A[ i + k * M ] * B[ k + j * N ];
         C[ i + j * M ] = sum;
}
```

Figure 2.14 – Side-by-side comparison of a matrix multiplication implemented in a standard C function (left) and an OpenCL kernel.

In OpenCL, code which will be executed on a device is implemented in specialized functions referred to as "kernels." This kernel defines a set of instructions to be performed by a single thread. When the host schedules a kernel for execution, a number of threads to be created is specified. That number of threads will be executed by the processing cores in the device, with each performing the kernel instructions on a separate piece of data.

Defining instructions in this way differs from the more common method used in most programming languages of explicitly defining the iteration through a data set with a for-loop (or while-loop). This can be seen in Figure 2.14 which shows the implementation of a matrix multiplication function in standard C as well as OpenCL.

The API included in the framework provides the host with the necessary tools for memory management as well as kernel scheduling. In a heterogeneous system, the host and device each possess their own regions of memory. Furthermore, the memory on the device consists of four regions:

1) Global memory – Read/write access for kernels as well as the host. Largest memory region, but high latency.
2) Constant memory – Read only access from host only. Small region, but low latency.
3) Local memory – Read/write access from group of processing elements. Second largest region, with second highest latencies.
4) Private memory – Read/write access from individual processing elements only. Small size, but very low latency.

Memory operations must be handled explicitly in OpenCL. Therefore, using the API, memory must be copied from the host to the device before it can be utilized by the device and vice versa. Furthermore, copies between regions on the device, such as from global to local memory, must be handled explicitly as well.

The need for explicit memory handling in OpenCL is quite different from the implicitly handled memory management of program execution on CPUs. This is the result

of OpenCL being a relatively new framework which is still in its early development. Well-developed programming languages, such as C, have advanced compilers which are capable of handling most of the memory management. Additionally, CPUs contain hardware specifically designed for handling memory, which is not often found on more specialized processors such as GPUs.[129]

The API also provides the tools necessary for compiling the kernels and scheduling their execution on the device. OpenCL kernels are compiled at run-time using the API functions called by the host code. This provides portability, as the intended device does not need to be known during compilation of the host code. Once the kernels are compiled, a "queue" is created on the device, which allows the host to perform actions on the device. These actions include memory transfers, kernel execution, etc. The operations submitted to the queues can either be executed in-order where they are performed in a first in, first out (FIFO) manner, or out-of-order where there is no guaranteed order of execution. The API provides tools for explicit synchronization of tasks, referred to as events, when out-of-order queues are utilized.

In order for a kernel to be executed on the device, it must be submitted to the queue. When submitted, the number work-items must be specified. A work-item is a single instance of the kernel performing its instructions. All work-items combined make up the work-space, which can be one, two or three dimensional. In the example of matrix multiplication provided in Figure 2.14, the work-space is two dimensional with $M \times P$ work-items each calculating a single element of matrix $\mathbf{C}$. In addition to the number of work-items, a work-group size can be defined when submitting. The work-group defines a set of work-items that execute on a single compute-unit. These work-items share a local

memory space and are capable of synchronization across the work-group. Once the kernel is submitted to the queue, the host can continue performing others tasks and even submit more kernels to the queue, while the device executes the tasks in its queue.[71]

2.5.2 Open Source Libraries

While the majority of our computational model was developed in-house, two open source libraries were utilized. These were the Bolt C++ library which provided a sorting function and the MWC64X pseudorandom number generator developed by David Thomas.[130, 131] These libraries were used rather than developing our own methods because they were able to be implemented in the code with relative ease, and had already undergone extensive optimization.

The Bolt C++ template library provides common sort, scan, reduce and transform algorithms implemented written in C++ and OpenCL for execution on both CPUs and GPUs, respectively.[130] In our model, we utilized the OpenCL implementation of the merge sort algorithm for sorting the array storing particle information. Using the method, the particles were sorted by their location in the domain defined by the four lattice points surrounding them. Merge sort is a comparison based sorting algorithm of order $O(n \log n)$ capable of parallelization.[132] In the Brownian dynamics method, the particles traveled distances much smaller than the lattice spacing each time step. Because of this, multiple time steps could occur between sorts (between 40 and 100). By sorting them, particles whose velocities and temperatures were obtained from the same lattice points were grouped together, thereby reducing the number of high latency reads from global memory. As the particles traveled distances much smaller than the lattice spacing each time step, multiple

time steps could occur between sorts (between 40 and 100). This, coupled with the reduced number global memory access, allowed for the OpenCL implementation of the Brownian dynamics model to simulate over one million particles on a GPU at significantly higher speeds than those possible using a CPU.

The MWC64X pseudorandom number generator (RNG) is based on a multiply-with-carry generator which utilizes two unsigned integers to produce a random number uniformly distributed between $\left(0, 2^{32}-1\right]$.[131] In a standard random number generator, a random number is calculated from the current state of the RNG before the state is updated and stored according to a set of rules. As a result, each state is a function of the previous state. When accessed in series, this does not create issues. If accessed in parallel (i.e. on a GPU), however, threads can read the same state and generate the same random number. This results in the RNG no longer providing pseudo-random numbers. In order to overcome this, multiple states (often referred to as streams) can be used. This ensures that no two threads try to access the same random number generator state. In our implementation, we utilized one stream for each particle. By dividing each random number by the max value, we obtained a uniformly distributed random number between 0 and 1.

2.6 Simulation Parameters

2.6.1 Simulation Domain

In our simulations, we use three different types of domains shown in Figure 2.15. The first type (Figure 2.15 (a)) consists of a single period of channel with periodic boundary conditions at the inlet and outlet. This allowed us to model the fluid flow and heat transfer

sufficiently far along the channel for the flow and temperature distribution to fully develop. The second type of domain (Figure 2.15 (b)) consists of multiple periods with periodic boundary conditions. The use of multiple periods ensures that the periodicity of the domain did not enforce unnatural frequencies when the flow became unsteady, while still simulating fully developed flow. The last type of domain (Figure 2.15 (c)) consists of multiple periods with a short straight section at the inlet and a long straight section at the outlet. The straight sections were necessary as periodic boundary conditions were used and these sections allow for oscillations in the fluid velocity to dissipate before returning to the inlet of the channel. This domain represents an entire heat exchanger channel and is used when simulating the formation of the fouling layer.

In our discussions, we make use of several terms to identify regions of the wavy domain. The regions, which include the centerline, midplane, peaks and furrows, are labelled on the diagram in Figure 2.15 (a). The centerline of the channel (dashed line) is the line centred halfway between the upper and lower walls at throughout the length of the channel. The midplane (dot-dashed line) is the horizontal line positioned halfway between the averaged heights of the upper and lower walls. The furrows of the channel are the crests and troughs of the upper and lower walls respectively while the channel peaks are the troughs of the upper wall and the and crests lower walls.

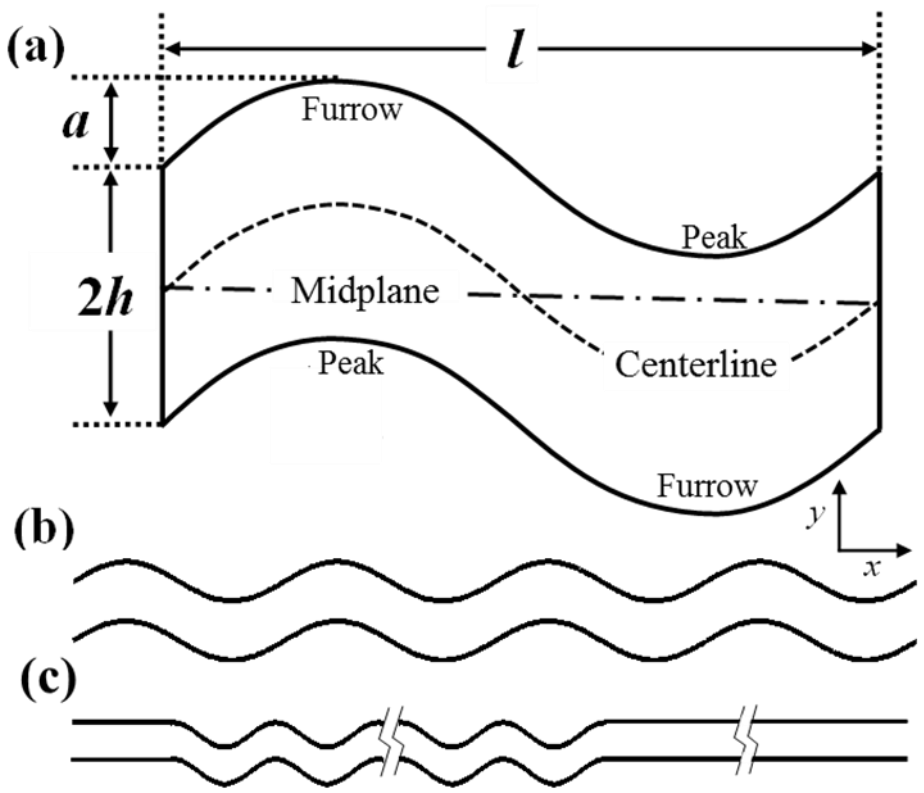

Figure 2.15 – Computation domain used when investigating (a) steady flows, (b) unsteady flows and (c) fouling layer development.

2.6.2 Geometric and Fluid Parameters

In all three domains, the upper and lower walls are separated by a distance $2h$, and the periodic shape of both walls is described by $f(x) = a\sin(2\pi x/l)$, where a and l are the amplitude and the period of the wall oscillations, respectively. In this study, we focus on channels in which the ratio a/l remains between $1/40$ and $1/3$. In all simulations, the flow is driven by a constant pressure gradient, $-p_x$. The parameters varied in each simulation are the normalized amplitude $A = a/h$, the normalized period or aspect ratio $L = l/h$, and the dimensionless pressure gradient $P = h^3 p_x/(3\rho\nu^2)$. Here, h is half the channel height, ρ is the density of the fluid, and $\nu = \mu/\rho$ is the kinematic viscosity of the

fluid. The dimensionless pressure gradient is chosen such that for a straight channel, it reduces to the Reynolds number, $\mathrm{Re} = u_m h/\nu$, where u_m is the mean velocity of the flow.

2.6.3 Heat Transfer Parameters

When investigating the heat transfer enhancement, both the single period and multiple period domains are used (see Figure 2.15 (a) and (b)). Periodic boundary conditions are used at the inlet and outlet of the channel for both the LBM and the FD thermal solver, with a bulk mean temperature at the inlet set to $T_b(0) = 1$. Along the wall, interpolated bounce back is used to enforce the no-slip boundary condition, and the wall temperature is set to $T_w = 0$. Again, the flow is driven by a constant pressure gradient, defined by the non-dimensional *P*. The heat transfer rate in the channel is characterized using both a local, Nu_l, and mean, Nu_m, Nusselt numbers defined as:[133]

$$\mathrm{Nu}_{\mathrm{l}}(x) = \frac{4a}{T_w - T_{m,x}}\left(\frac{\partial T_x}{\partial n}\right) \qquad 2.51$$

$$\mathrm{Nu}_{\mathrm{m}} = \frac{2h^2 u_m}{l\alpha}\ln\left(\frac{T_{m,in}}{T_{m,out}}\right). \qquad 2.52$$

Here, $\partial T_x/\partial n$ is the temperature gradient normal to the wall, T_m is the bulk mean temperature with subscripts and T_w is the wall temperature. The Nusselt numbers, Nu_{l} and Nu_{m}, define the ratio of convective to conductive heat transfer along the channel wall and across a full channel period, respectively. In all simulations, the Prandtl number was kept constant at $\mathrm{Pr} = 0.708$, which corresponds to that of air.

2.6.4 Fouling Layer Development Parameters

When investigating the heat transfer enhancement, the domain shown in Figure 2.15 (c) is used for all simulations. In each simulation, we set $h = 50$ lattice nodes. In order to maintain similar total channel lengths when using various values for L, we vary the total number of periods in the channel. Specifically, we use 27, 20 and 16 periods leading to lengths (for the wavy section of the channel) of 4050, 4000, and 4000 lattice nodes for $L = 3$, $L = 4$ and $L = 5$, respectively. Furthermore, the inlet length is set to the length of a single period, while the outlet has a length of 4000 lattice nodes. This provides sufficient length for oscillations induced in the flow to dissipate as periodic boundary conditions are used for the fluid solver.

As before, the flow is driven by a constant pressure gradient, defined by P. For the FDTM, the inlet and wall temperatures are set to constant values of $T_{in} = 1$ and $T_w = 0$, while an extrapolation boundary condition is used for the outlet. Along the wall, interpolated bounce back is used to enforce the no-slip boundary condition. For the Brownian dynamics solver, the particles are released at the inlet of the wavy section, and the method uses the boundary conditions described Section 2.3. The number of particles used in each simulation is kept constant at 2^{20} ($\sim 10^6$).

Due to limitations in simulating long time scales using the lattice Boltzmann method, a simulation length of 25 million time steps was used for each simulation. This allows for comparison across the various geometric and flow parameters. Additionally, by using a large particle number concentration, the effective throughput of the channel was equivalent to that experienced by an EGR heat exchanger channel after several hours of use. Because

we compare results across a constant simulation time span, we use the total simulation time, T_{total}, to define the time scale. For each simulation, we allow the fluid flow and heat transfer to fully develop before releasing the particles. It is this time, when particles are released, that is considered $t = 0$.

In order to quantify the effects of the fouling layer on the heat transfer occurring in the channel, both the local and mean Nusselt number defined above are used along with the heat exchanger effectiveness, defined as:

$$\varepsilon = \frac{T_{avg,inlet} - T_{avg,outlet}}{T_{avg,inlet} - T_w}. \tag{2.53}$$

Here, $T_{avg,inlet}$ and $T_{avg,outlet}$ are the average temperature (not bulk mean) at the inlet and outlet of the wavy section of the channel, respectively. To compare the shear stress in each channel, a normalized wall shear stress is used, which is defined as:

$$\bar{\tau}_w = \tau_w / \left(p_x h \right). \tag{2.54}$$

This normalization is chosen such that for a straight channel, it reduces to $\bar{\tau}_w = 1$. When displaying the distribution of $\bar{\tau}_w$, positive values are used to represent shear stresses acting in the downstream direction and negative values the upstream.

In order to convert between the units used in the model and real units, the density and kinematic viscosity of air at 473 K are used, which are $\rho = 0.675$ kg/m^3 and $\nu = 4.1 \times 10^{-5}$ m^2/s. This, along with a channel height of $h = 2$ mm and inlet and wall temperatures of $T_{in} = 673$ K and $T_w = 363$ K provides the necessary information to convert

between real and simulation units. The number concentration of particles used in each simulation is $10^{11}\ \#/m^3$, while the properties of air at 473 K are used for the working fluid.

CHAPTER 3. VALIDATION

In this chapter, we detail the simulations performed to validate out computer model. We performed four tests to validate each of the four models. In each case we compared results with those obtained from analytical solutions to verify each model.

3.1 Lattice Boltzmann Model

To validate our model, we compared the simulation results for wavy channels with those obtained using an analytical model valid for small A.[134] Figure 3.1 shows the longitudinal velocities at two different cross-sections of the channel for two test cases with different values for the pressure gradient and wave amplitude. We found close agreement between our simulations and the theory indicating that our model accurately captures the flow within a wavy channel. Figure 3.1 also includes the results from simulations using two different grid sizes, with respectively $h = 20$ nodes and $h = 40$ nodes. For both cases the two grid sizes provide nearly identical results. This indicates that the use of a grid with $h = 20$ nodes provides sufficiently accurate results while remaining computationally more efficient.

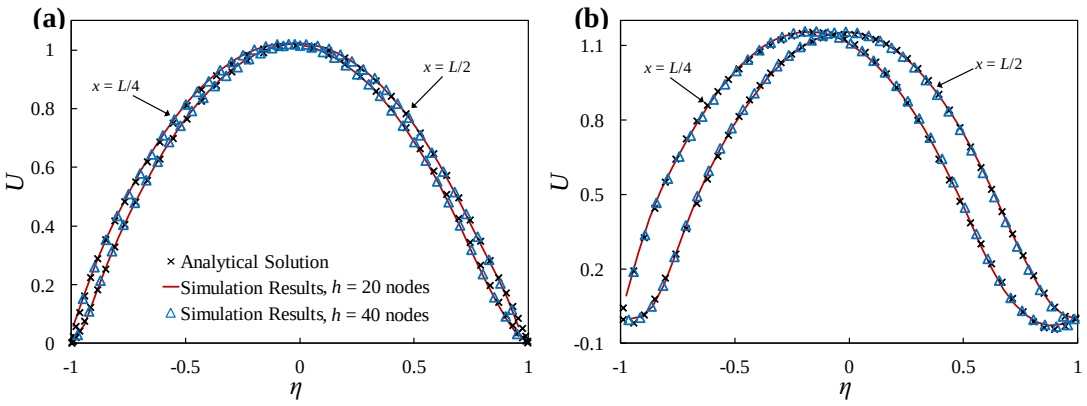

Figure 3.1 – Dimensionless longitudinal velocities at $x = L/4$ and $x = L/2$ for two test cases of wavy channels plotted against the dimensionless distance from the centerline, $\eta = \left[y - a\sin\left(2\pi/l\right) \right] / h - 1$. The velocity, U, is normalized by the maximum velocity in a flow in a straight channel with the same pressure drop. System parameters are (a) $A = 0.005$, $L = 2$, $P = 250$ and Re = 230.6 and (b) $A = 0.2$, $L = 3$, $P = 600$ and Re = 386.2.

3.2 Finite-Differences Thermal Model

We performed a validation test to ensure the accuracy of the thermal model and the implementation of the wall boundary conditions. The test consisted of simulating a flow of $\mathrm{Re} = 100$ and $\mathrm{Pr} = 0.708$ in a pipe with constant temperatures at the inlet and the walls. To perform this test, we extended our thermal model to three dimensions by including derivatives with respect to the *z* direction, and modified our lattice Boltzmann model to a three dimensional nineteen velocity (D3Q19). The results from our numerical model were compared with the results obtained from the Graetz series solution.[135, 136] A plot of the temperature contours obtained from our model and the analytical solution are shown in Figure 3.2. It can be seen the results from our model agree well with the analytical data indicating that our model provides accurate solution for this convective heat transfer problem.

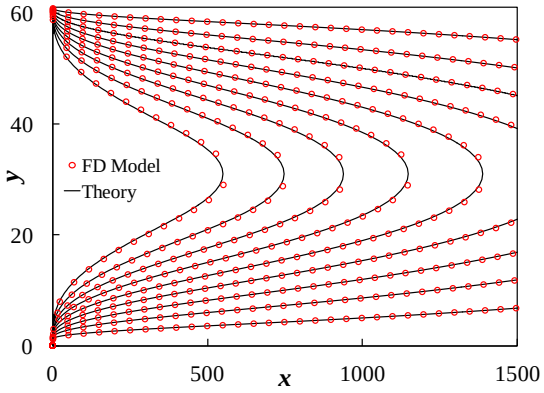

Figure 3.2 – Contour lines of temperature for flow through a pipe with Re = 100 and Pr = 0.708 and temperatures of 1 and 0 for inlet and walls respectively.

3.3 Brownian Dynamics Model

A third validation test was performed to verify accuracy of the thermophoretic and advection velocities calculated in the Brownian dynamics model. In this test particles were released along the heated inlet of a pipe with a constant cold temperatures along the walls. As with the finite-differences thermal model validation, the LBM, FDTM and BD models were extended to three dimensions to perform this test. The parameters used in our simulation were $\mathrm{Re}=120$, $\mathrm{Pr}=2$, $K_{th}=0.5$, a radius of 40 and $\theta^{*}=T_w/(T_{in}-T_w)=0.5$. The results obtained with our model and those calculated from an analytical solution[106] are shown in Figure 3.3. It can be seen that the results from our model agree well with the theory indicating that our model accurately captures the advection and thermophoretic motion of submicron sized particles.

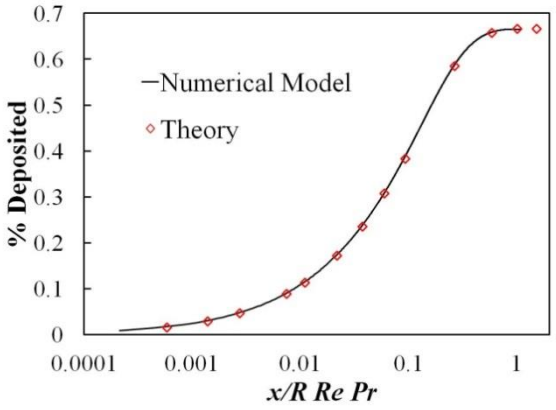

Figure 3.3 – Cumulative deposition of particles by thermophoresis along length of pipe obtained from numerical model (solid line) and analytical solution (markers). Simulation parameters were Re = 120, Pr = 2, K_{th} = 0.5, R = 40 and θ^* = 0.5.

3.4 Fouling Layer Model

In order to validate the fouling layer model we simulated particle laden flow through a plain channel. The parameters used in the simulation were $\mathrm{Re} = 100$, $\mathrm{Pr} = 0.708$, $h = 1\mathrm{mm}$, $T_{inlet} = 400^{\circ}\mathrm{C}$, $T_w = 90^{\circ}\mathrm{C}$, and a particle diameter of $d_p = 100\,\mathrm{nm}$. Properties of air at 250°C were used for the fluid and those provided in the methodology section were used for the particles with the exception of the Hamaker's constant. For this test, the Hamaker's constant was artificially reduced from 1E-20 J to a value of 5.45E-23 J in order for the critical shear stress to be reached when the fouling layer grew to a thickness of approximately 1.5 nodes. A domain size of 100×8000 nodes, a LBM relaxation parameter of $\tau = 0.52$, and a density of $\rho = 1$ (in LB units) were used in the simulation, and for non-dimensionalizing the other parameters. Fluid entered the domain with a parabolic velocity profile, at a constant temperature and with a uniform concentration of particles.

The critical shear stress for a 100 nm particle (using the reduced Hamaker's constant) is $\tau_{crit} = 5.67$ in lattice Boltzmann units. Assuming a parabolic velocity profile and flat wall, the shear stress along the wall is given by:

$$\tau_w = -\mu \frac{du}{dy} = \frac{3\mu U_m}{h}. \tag{3.1}$$

Here U_m and h are the mean velocity and half the height of the channel at the location of interest. From conservation of mass we know:

$$U_m h = U_{m,in} h_{in} = \mathrm{Re}\,\nu, \tag{3.2}$$

where the subscript *in* indicates the value at the channel inlet. Combining Equations 3.1 and 3.2 gives:

$$\tau_w(x) = \frac{3\mu\nu\,\mathrm{Re}}{\left[h_{in} - \delta(x)\right]^2}, \tag{3.3}$$

where $\delta(x)$ is the thickness of the fouling layer at a location x along the channel. With the height of the channel varying due to the fouling layer growth, the velocity profile will not remain parabolic throughout the length of the channel. Although this assumption was made when deriving Equation 3.3, it still should provide a reasonable estimate of the shear stress for a given height of the fouled channel. Therefore, with a critical shear stress of 5.67 we expect the thickness of the layer to stop growing at a height of ~1.5 LB units.

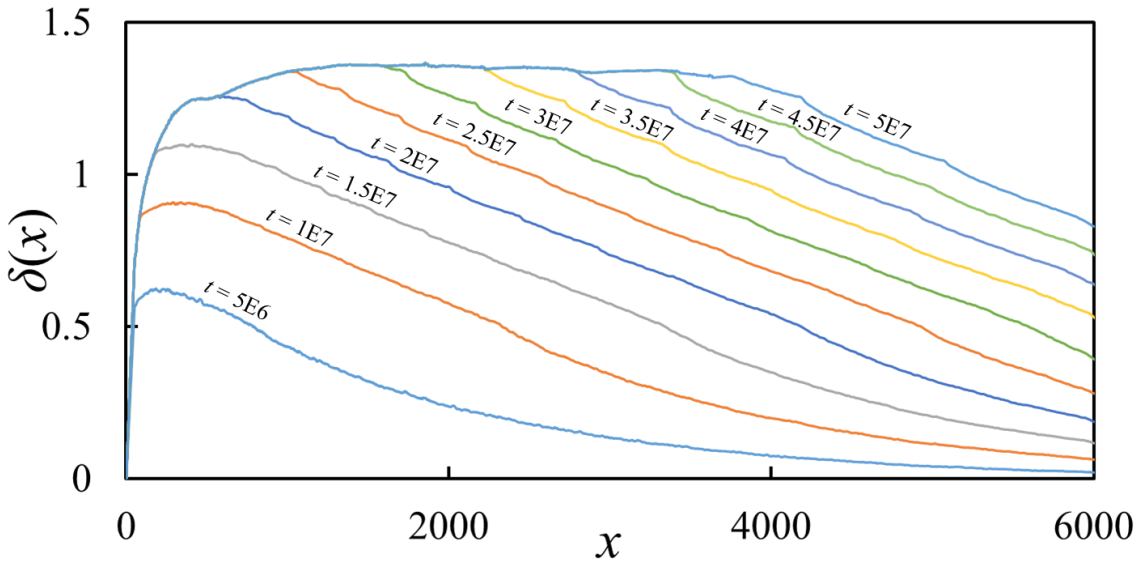

Figure 3.4 – Thickness of fouling layer along bottom of channel at several times.

The profile of the fouling layer at several points in time is provided in Figure 3.4. It can be seen in this figure that the fouling layer grows fastest at near the inlet, and the growth rate decreases along the length of the channel. Furthermore, the fouling layer continues to grow until the shear stress at the wall is sufficient to remove any additional deposits, which occurs at a thickness of ~1.35 LB units. This is slightly less that the 1.5 LB units predicted by Equation 3.3 because the flow is still developing from the channel narrowing as a result of the fouling layer growth. This increases the wall shear stress, reducing the thickness necessary to achieve the critical value. Near the outlet of the channel, the fouling layer does not reach its maximum thickness. This is a result of the simulation ending while it was still growing. If the simulation was continued, the thickness of the outlet would eventually reach the ~1.35 units as well.

Plots of the temporal distribution of the fouling layer thickness and the wall shear stress at $x = 1000$, $x = 3000$ and $x = 5000$ are provided in Figure 3.5(a), (b) and (c) respectively. It can be seen in Figure 3.5(a) that as the fouling layer grows the growth rate

decreases, which is the result of the temperature gradient decreasing with increasing thickness. The thermophoretic velocity decreases with the temperature gradient leading to a reduction in the deposition rate at that location. About halfway through the simulation, the growth rate abruptly drops to zero when the wall shear stress reaches the critical value for the particle diameter. The rate changes abruptly due to the reduced Hamaker's constant. Had it not been reduced, the thermophoretic velocities would continue to decrease with the temperature gradients causing the deposition rate to eventually decrease to zero. This would result in the thickness asymptotically approaching a final height without achieving the critical shear stress at the wall. Because of this, we reduced the Hamaker's constant in order to test the shear removal model. This would have occurred before the critical shear stress. Further down the channel at $x = 3000$, shown in Figure 3.5(b), it can be seen that the growth rate is slower, resulting in its maximum thickness not being reached until more than ¾ of the way through the simulation. Near the outlet, shown in Figure 3.5(c), the fouling layer is still growing due to the critical shear stress not being reached.

Both the wall shear stress calculated in the model and using Equation 3.3 are included along with the thickness in these plots. It can be seen that the shear has an initial value of ~5.27E-6 for all three locations, which agrees well with the expected value of 5.33E-6 plain channel flow and increases with the thickness of the fouling layer. The discontinuity in the model value of these three plots occurs when the surface is positioned extremely close to a lattice node. The size of the discontinuity is exaggerated by the narrow bounds of the axis and from Figure 3.5(d) it can be seen that the values calculated in the model deviate less than 2.5% from the theoretical value even at this location.

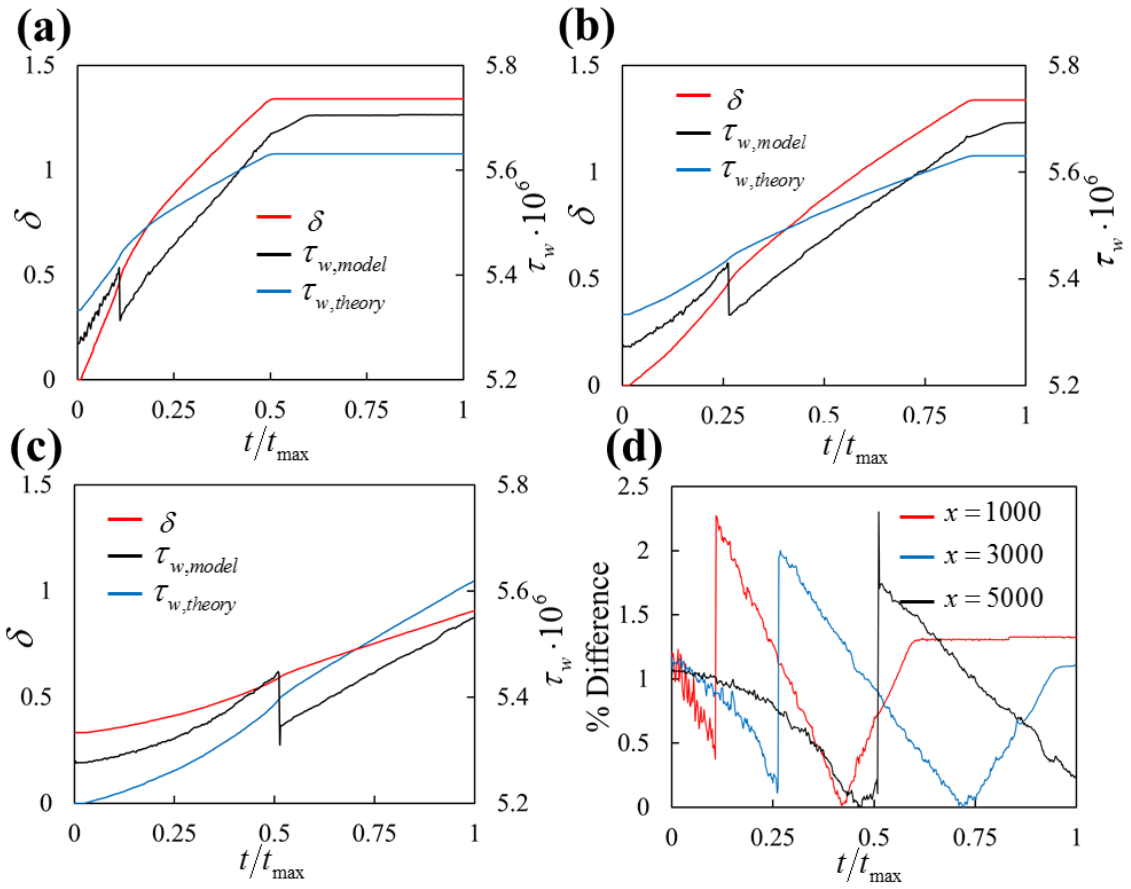

Figure 3.5 – Plots of the thickness wall shear stresses at (a) x = 1000, (b) x = 3000 and (c) x = 5000. Shear stress in plots include both those calculated in the model and those calculated using Equation 3.3. Percent difference between two shear stresses provided in (d).

From this test we can see that the model is able to simulate a growing fouling layer resulting from deposition of particles entrained in the flow. Additionally, the wall shear stresses calculated by the model agree well with theory and the model accurately captures the effect of deposit removal when these shear stresses are sufficiently high. Without an analytical model or experimental data to compare to, we cannot provide a more robust validation of the model. However, the we believe that the above validation provides adequate proof that our fouling layer model is well suited for simulating the formation of the fouling layer in a wavy walled EGR heat exchanger.

CHAPTER 4. FLUID FLOW

4.1 Introduction

Due to their ability to induce chaotic flows at relatively low Reynolds numbers, the wavy walled geometry is well suited for many engineering applications. As such, many investigations have been performed to understand its effect on the flow. Despite the significant body of research, little information exists regarding the onset of circulatory, unsteady flow and chaotic flows over a wide range of geometric parameters. In this chapter, we employ computer simulations to systematically investigate a laminar pressure-driven flow in a two-dimensional wavy walled channel with asymmetric sinusoidal walls.

Our examination begins with the influence that the amplitude and period of the sinusoidal walls, as well as the magnitude of the pressure drop have on the flow structures in the steady regime as well as immediately after transition to unsteady. Because the ability of wavy walled channels to induce unsteady flows is the primary reason for their use, we investigate how the pressure drop at which the flow becomes unsteady varies with the amplitude and period of the walls. Furthermore, we determine the minimum pressure drop necessary for unsteady flows. We continue our investigation be examining how subsequent bifurcations affect the flow through the channel and as it transitions from laminar to chaotic. Here we utilize both visual examination of the flow as well as several techniques used to examine dynamical systems during our analysis. From our results we construct a phase diagram of the flow regimes found for the various geometries and pressure drops investigated. Finally, we conclude with an examination of the frictional losses associated with the wavy walled geometry.

4.2 Computational Setup

In our investigation of the fluid flow, we utilize two different domain types. When simulating steady flow, a domain consisting of a single period is used (see Figure 2.15 (a)). For simulating unsteady flow, we use a domain containing seven or more periods (see Figure 2.15 (b)). The use of multiple periods ensures that the periodicity of the domain does not enforce unnatural frequencies in the unsteady flow. In both domains, we use periodic boundary conditions at the inlet and outlet, and the flow is driven by a constant pressure gradient. This allowed us to model the fluid flow sufficiently far along the channel for the flow to fully develop.

4.3 Analysis Methods

In our investigation of unsteady flows in the wavy walled geometry, we make use of multiple methods for analyzing and comparing flows occurring at different stages in their transition from time-periodic to chaotic. This includes examination of the time evolution of flow structures using snapshots of the flow at various times. In these snapshots, we visualize flow structures using instantaneous streamlines as well as color contour plots of the normalized pressure distribution defined as:

$$\overline{p}(x,y) = \frac{\left(\rho(x,y) - \rho_o\right)c_s^2}{p_x h}. \tag{4.1}$$

Here $\rho(x,y)$ is the local density, $\rho_o = 1$ is the simulation density, c_s is the speed of sound and p_x is the pressure gradient driving the flow. These snapshots allow for an

understanding of how the geometry influences the flow, and to compare how the flow changes as it bifurcates.

An example of the format which we will use to present snapshots of the unstable flow in is provided in Figure 4.1. In each figure we will provide a single snapshot showing two full wall periods Figure 4.1 (a) as well as several zoomed in views of a furrow along the upper wall, each of which are taken at equally spaced intervals in time. In this example we show six snapshots (Figures 4.1 (c) – (h)) each spaced one sixth of the oscillation period (in time) apart. However, more than six snapshots may be provided when examining more complex flow patterns. Additionally, the plot in Figure 4.1 (b) shows three periods of oscillation in the u velocity component at the location indicated by the white dot in each of the snapshots (this position is also indicated in Figure 4.2). The *x* shaped markers along the line, indicate the time that the corresponding snapshot in Figures 4.1 (c) – (h) represents.

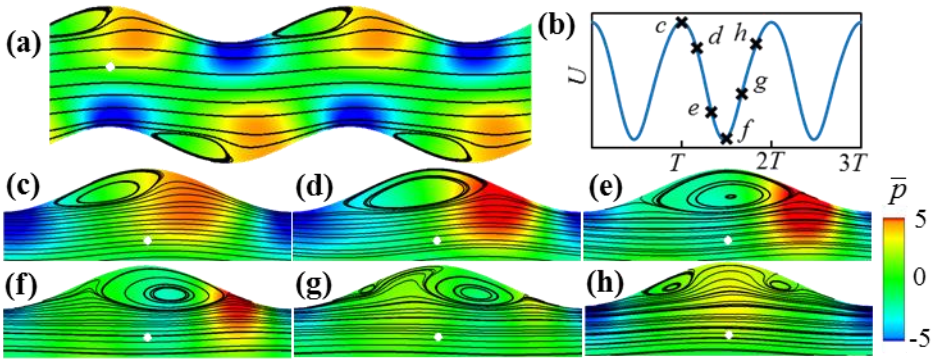

Figure 4.1 – Example of figure containing snapshots used in subsequent discussion

In addition to the qualitative examination of the flow structures, an analysis of the velocity at a representative point in the domain provides a quantitative evaluation of the various flows. The representative point from which the velocity is obtained, shown in Figure 4.2, is located along the centerline of the channel above the middle of the lower wall

peak. In this analysis we compare how the temporal evolution and Fourier power spectrum of the velocity changes for the various flow conditions. Here, the u and v components of the velocity are presented in terms of the instantaneous local Reynolds numbers $\mathrm{Re}_{l,u}(t) = u(t)h/\nu$ and $\mathrm{Re}_{l,v}(t) = v(t)h/\nu$, respectively. These variables are plotted as a function of the normalized time $\bar{t} = th^2/\nu$ to show their temporal evolution. The Fast Fourier Transform (FFT) function built into the MATLAB software is used to obtain the power spectrum of $\mathrm{Re}_{l,u}(\bar{t})$. The amplitudes obtained for the power spectrum are plotted as a function of the non-dimensional frequency $\bar{f} = \bar{t}^{-1}$.

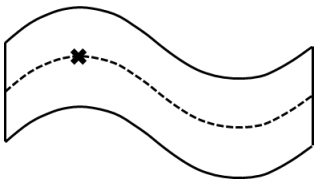

Figure 4.2 – Diagram showing location where velocity measurements are taken (position indicated with x).

Further analysis is performed on the local velocity data using dynamical system analysis techniques to investigate how the flow bifurcates and to determine when the flow becomes chaotic. These techniques include reconstructing the pseudo-phase space as well using Poincaré sections to reduce the dimension of the attractor. In pseudo-phase space reconstruction, an *n*-dimensional pseudo-phase space, $\mathbf{X}(t)$, is obtained from a single scalar time series, $x(t)$, according to:[137, 138]

$$\mathbf{X}(t) = \{x(t), x(t+\tau), x(t+2\tau), ..., x(t+n\tau)\}, \qquad 4.2$$

where τ is the time delay. The value for the time delay is calculated using the method of mutual information developed by Fraser and Swinney.[139] In this method, the time delay is determined as the value which minimizes the mutual information between the sets $x(t)$ and $x(t+\tau)$. Using this time delay, we reconstruct a three dimensional pseudo-phase space defined as from the data set $\bar{\mathbf{U}}(t)=\{\bar{U}(t),\bar{U}(t+\tau),\bar{U}(t+2\tau)\}$ were the $\bar{U}$ is the u velocity component normalized to the range $[-1,1]$. We plot this pseudo-phase space in order to examine the attractor defining the system. This examination is aided through the use of Poincaré sections which reduce the three-dimensional phase space to a two-dimensional plane. The Poincaré is obtained by selecting a plane which cuts through the attractor and determining the locations at which the attractor intersects the plane from a single direction.[140]

4.4 Results and Discussion

4.4.1 Steady Flow Structures

The wavy walls of a parallel plate channel induce a velocity in the cross-stream y direction. In the Stokes regime representing a flow with $\mathrm{Re}<<1$, the flow streamlines closely follow the wavy channel shape and the maximum velocity is located approximately halfway between the walls throughout the channel (Figure 4.3 (a) and (d)). Furthermore, the x component of the flow velocity is always positive; therefore we refer to this low-Reynolds-number flow regime as unidirectional. As the flow rate increases, fluid inertia causes the fast flow to be localized in the center of the channel, whereas the flow in the channel furrows is characterized by a relatively slow motion. This situation is illustrated in

Figure 4.3 (b) and (e) showing unidirectional flows in channels with two representative amplitudes of wavy walls. As can be seen in these figures, the curvature of the streamlines is smaller than that of the channel walls and it further decreases for streamlines that are located closer to the channel centerline. Additionally, the flow develops a slight back-forward asymmetry. This is in contrast to a fully symmetrical flow in the Stokes regime shown in Figure 4.3 (a) and (d).

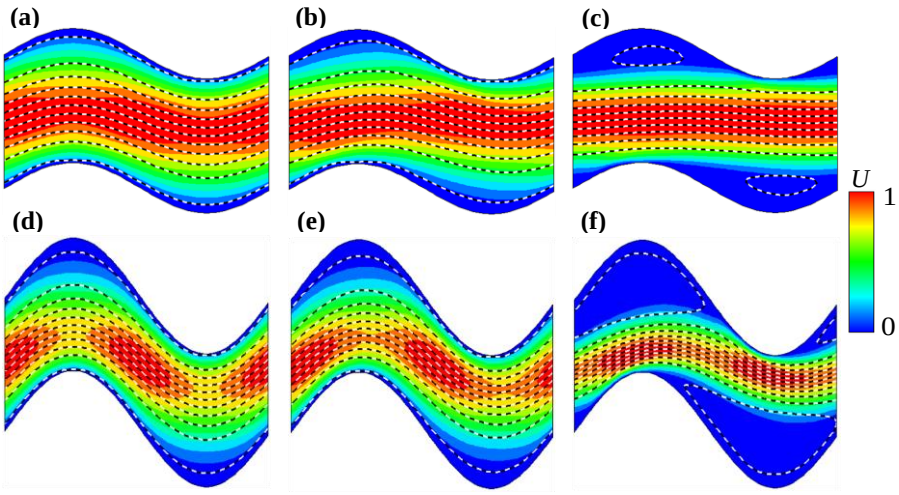

Figure 4.3 – Streamlines and velocity magnitudes for steady unidirectional and circulatory flow regimes in a sinusoidal channel with wall period L = 4: (a) A = 0.375, Stokes flow (Re = 0); (b) A = 0.375, P = 20, Re = 13; (c) A = 0.375, P = 340, Re = 137.9; (d) A = 0.875, Stokes flow (Re = 0); (e) A = 0.875, P = 20, Re = 5; (f) A = 0.875, P = 430, Re = 38.1. The dotted lines show flow streamlines that are distributed such that the flow rate is constant between each pair of streamlines. The magnitude of flow velocity U is normalized by the maximum velocity in the flow.

When the driving pressure gradient is increased over a critical value, the shear stresses between the fast moving part of the flow at the center of the channel and the nearly stagnant fluid in the channel furrows lead to the formation of steady fluid circulations located in the channel furrows (Figure 4.3 (c) and (f)). We refer to this flow regime as circulatory and designate the critical pressure leading to the transition from the

unidirectional regime to this circulatory regime as P_{cr1}. In this regime, the vortices are characterized by enclosed streamlines, whereas the streamlines located near the channel centerline are more straightened and have smaller curvature compared to those in the unidirectional regime (*cf* Figure 4.3 (b) and (c) and Figure 4.3 (e) and (f)).

4.4.2 Time Periodic Flow Structures

As the flow rate in the channel is increased further and the pressure exceeds a second critical value the circulatory flow becomes unsteady through a supercritical Hopf bifurcation. We designate this critical value for the pressure that leads to the transition to unsteady flow as P_{cr2}. This flow regime is characterized by time periodic variations of the fluid velocity and by repeating changes in the vortex shape and topology.

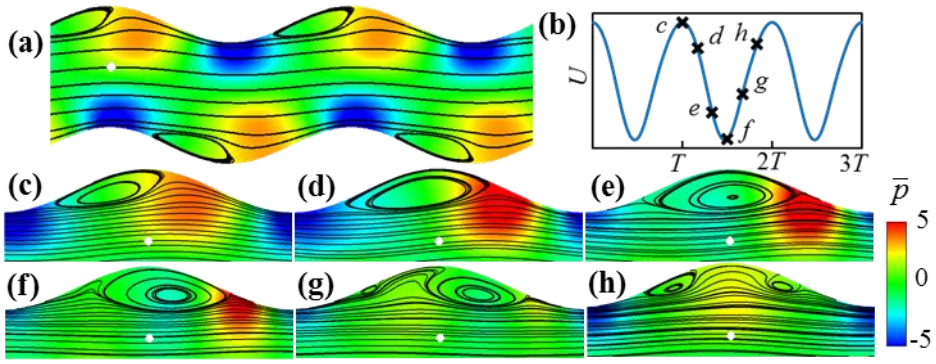

Figure 4.4 – Streamlines and pressure field in *A* = 0.3, *L* = 4 and *P* = 400 channel.

We find for channels with small wall amplitudes that the unsteady motion of the fluid results from a continuous cycle of vortex generation, growth and contraction in the furrows. This can be seen in Figure 4.4 which provides snapshots of the streamlines and pressure field at various points in time for a channel with $A = 0.3$, $L = 4$, and $P = 400$. In each oscillation period, an adverse pressure gradient along the backside of the wall peak results

in the flow separating from the wall, producing a vortex, which can be seen on the left side of the furrow in Figure 4.4 (g). As fluid is ejected from the contracting vortex in the upstream furrow, it travels along the wall peak into the newly formed vortex as it grows (Figure 4.4 (h)). This growth continues (Figure 4.4 (c) and (d)) until the vortex fills nearly all of the furrow as seen in Figure 4.4 (e). Eventually, the vortex detaches from the wall and contracts toward the right side of the furrow (Figure 4.4 (f)). As the vortex contracts, fluid is ejected out and into the next furrow, while the vortex in the upstream furrow does the same. The inertia of the fluid entering from the upstream furrow is sufficiently high for the flow to separate from the wall and generate a new vortex as the cycle repeats (Figure 4.4 (g)).

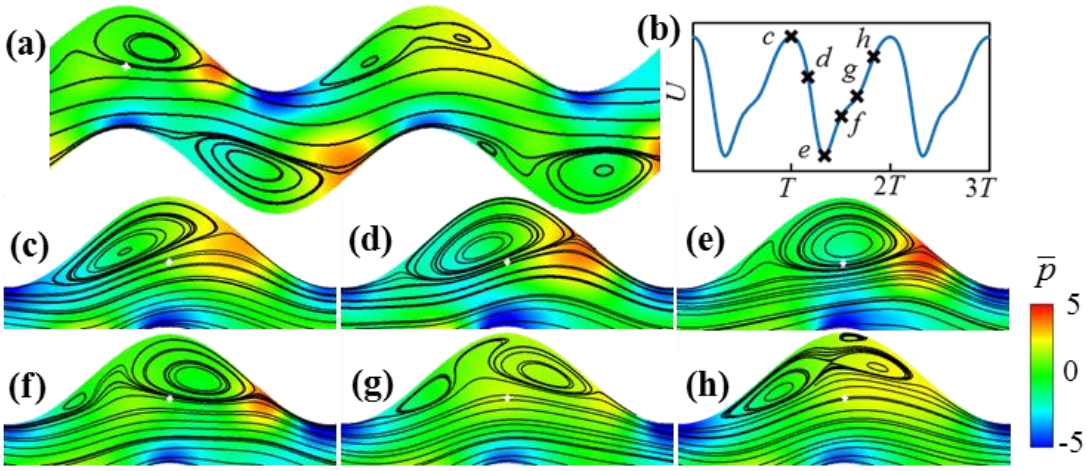

Figure 4.5 – Streamlines and pressure field in A = 0.7, L = 5 and P = 300 channel.

For channels with larger wall amplitudes, the unsteady motion of the fluid still results from the generation of vortices in the furrows. However, when a new vortex is generated it combines with the vortex already existing in the furrow rather than replacing it. This causes the vortices to undergo significant changes in size and shape as well as the momentary formation of a third vortex as the two vortices combine. The process can be

seen in the snapshots contained in Figure 4.5, which are from a channel with $A = 0.7$, $L = 5$, and $P = 300$. As the existing vortex in the furrow travels to the right side of the furrow, fluid travels into the furrow to fill the area left behind it. This flow separates from the wall, and new vortex is generated (Figure 4.5 (f)). The vortex grows in size and strength as it entrains fluid ejected from the upstream furrow. After only a small amount of growth, it blocks the fluid flowing in behind the existing vortex as it travels to the right (Figure 4.5 (g)). This diverts the flow under the existing vortex, causes it to travel backward, into the top of the furrow (or bottom for furrows along the lower wall). As this occurs, it approaches and is eventually absorbed by the stronger, newly generated vortex. During this process, a small amount of fluid becomes trapped between the vortices and the wall, leading to the momentary formation of a third, smaller vortex (Figure 4.5 (h)). This vortex is absorbed as well, leading to the single vortex seen in Figure 4.5 (c), which grows to fill the entire furrow (Figure 4.5 (d)). The vortex eventually detaches from the wall and begins contracting as it moves to the right side of the furrow (Figure 4.5 (e)). As this fluid flows to fill the area left behind the contracting vortex, it eventually separates from the wall and the process repeats (Figure 4.5 (f)). In what follows, we will refer to the unsteady flow regime corresponding to the flow pattern shown in Figure 4.4 as the shedding regime, whereas the regime shown in Figure 4.5 will be referred to as the oscillatory regime.

In addition to the evolution of the vortices generated in the furrows, we observe two other distinguishing characteristics of these two regimes. The first can be seen in the snapshots shown in Figures 4.4 (a) and 4.5 (a). At any point in time in the oscillatory regime, the vortices in each furrow are at a different stage in their cycle. This can be seen in Figure 4.6 which shows the time distribution of the u velocity component (normalized

as the local Reynolds number $\mathrm{Re}_{l,u}$) sampled at identical locations within three consecutive periods of the channel. Here we see that while the velocity undergoes identical periodic oscillations in each period of the channel, they occur out of phase from one another. Unlike the oscillating regime, the flow pattern in the shedding regime repeats across every (spatial) period of the channel as seen in Figure 4.4 (a). Furthermore, the evolution of the vortices in the furrows of the upper and lower walls occur in phase as well, leading to identical flows occurring across every furrow simultaneously.

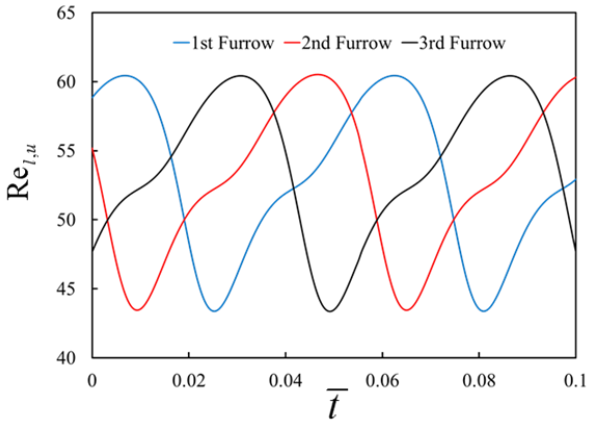

Figure 4.6 – Time distribution of local *u* velocity component sampled from representative location in three successive periods of a channel with *A* = 0.7, *L* = 5 and *P* = 300.

The second characteristic distinguishing the shedding and oscillatory regime is visible in the evolution of the u velocity component shown in Figures 4.4 (b) and 4.5 (b). In the shedding regime, the generation, growth and contraction cycle of the vortices is relatively simple. Furthermore, the vortices remain above the location from which the velocity is sampled throughout their entire cycle. This results in the velocity having the nearly sinusoidal shape seen in Figure 4.4 (b). Unlike the shedding regime, however, vortices in the oscillatory regime undergo more complex changes in their shape and

location. This, coupled with the vortices traveling over the sampling location leads to the temporal distribution of the velocity component having a saw-tooth-like shape, which can be seen in Figure 4.5 (b).

4.4.3 Transition To Unsteady Flow

Our simulations indicate that the transitions between different flow regimes in a pressure driven flow in wavy channels depend on the magnitude of the wall amplitude A and period L. To characterize the conditions at which these transitions take place, we constructed a phase diagram that shows the magnitudes of the critical pressures P_{cr1} and P_{cr2} for different values of the wall amplitude. These pressures are shown in Figure 4.7 by respectively empty and filled symbols for different values of the channel period L.

Pressure P_{cr1} indicating the transition between unidirectional flow and circulatory flow monotonically decreases with increasing wave amplitude. Larger amplitudes of the wavy walls focus the flow closer to the midplane of the channel, leaving larger areas of slow moving fluid in the furrows (*cf.* Figure 4.3 (b) and (e)). In this situation, the circulatory vortices are able to form at a lower value of P. We find this behavior for all L considered in our study; However, the magnitude of P_{cr1} is smaller for smaller L. This suggests that the larger magnitude of the relative depth of the furrows A/L facilitates a more rapid development of the vortices, thereby leading to a lower P_{cr1} at which the circulation emerges.

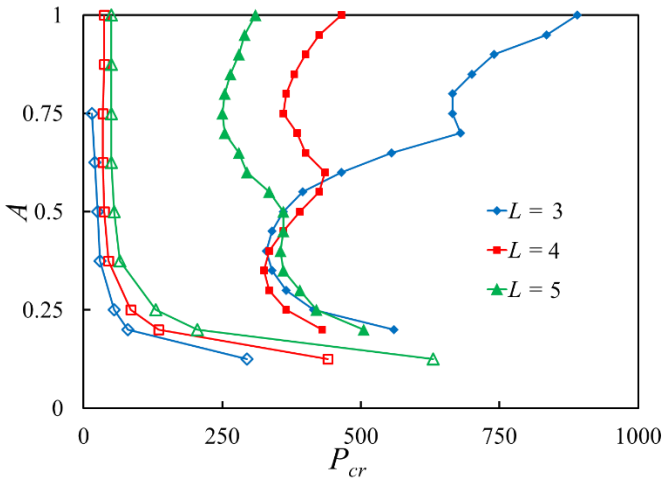

Figure 4.7 – Diagram displaying the critical pressure gradients P_{cr1} (the empty markers) and P_{cr2} (the filled markers), at which the respective transitions between the unidirectional and circulatory flow regimes and between the circulatory and unsteady flow regimes occur for various wall amplitudes A.

Unlike the transition from a unidirectional to a circulatory flow, the relationship between the critical pressure drop indicating the onset of unsteady flow P_{cr2} and the wall amplitude A is more complex (Figure 4.7). Specifically, P_{cr2} has two minima, P_L and P_U, that correspond to flows in channels with relatively small and relatively large wall amplitudes. Furthermore, the shape of the curve separating the regions with circulatory and unsteady flow strongly depends on the period L.

In the following discussion, we refer to the amplitudes at which P_{cr2} has the respective minimum values P_L and P_U as A_L and A_U. Furthermore, we refer to A_M as the amplitude at which P_{cr2} has a local maximum, P_M, between the two minima P_L and P_U; thus, $A_L < A_M < A_U$.

Figures 4.4 and 4.5 show snapshots of the unsteady flow at pressures slightly above the critical ones for, respectively, A_L and A_U in a channel. When the wall amplitude is

smaller than A_L, the critical pressure P_{cr2} decreases with increasing A (Figure 4.7). This decrease of P_{cr2} can be related to larger disturbances that are created in the flow by walls with larger waviness. Larger wall amplitudes, on the other hand also increase viscous dissipation and reduce the flow rate in the channel. This latter effect has a stabilizing effect on the flow and, when A is increased beyond A_L, a further increase of the wave amplitude requires an increased pressure to maintain the sufficiently large flow rate enabling the development of an unsteady flow. Thus, when A is less than A_L, P_{cr2} decreases with A. However, when A exceeds A_L and is in the range $A_L < A < A_M$, P_{cr2} increases with A.

For A greater than A_M, the critical pressure P_{cr2} decreases with A until the amplitude reaches A_U. In this case, an increasing depth of furrows filled with a slow moving fluid assists the development of unsteady flow, resulting in a decreased P_{cr2}. However when A is greater than A_U, this trend reverses and P_{cr2} increases due to the growing viscous dissipation in the channel further suppressing the flow.

Figure 4.7 indicates that the critical pressures P_L and P_U depend on the channel period L. In Figure 4.8, we plot both these pressures for different values of L in a range between 2 and 10. This figure shows that minimum values exist for both the critical pressures. The minimum in the curve corresponding to P_L occurs at $A = 0.35$ and $L = 3.5$ (see inset in Figure 4.8). This minimum pressure is equal to $P_{cr2} = 320$ which results in a Reynolds number of $\mathrm{Re} = 128$. The critical pressure P_U has a minimum at $L = 8$ and $A = 0.81$, in which case it is equal to $P_{cr2} = 202$ and at a Reynolds number of $\mathrm{Re} = 81.2$.

Note that the critical pressure P_U changes by only about 10% for a range of L between 6 and 10. In Figure 4.8, we report values of P_L for L less than 5 because this regime no longer exists for the amplitudes $0.125 \le A \le 1$ for larger values of L. We also find that P_U only exists for $L \ge 3$. Thus, the critical pressure has two minima for periods $3 \le L \le 5$ and amplitudes $0.125 \le A \le 1$, whereas for longer and shorter channel periods only one minimum, either P_L and P_U exists. Furthermore, we find that the amplitudes A_L and A_U both depend on the wall wave period, although A_L seems to be more sensitive to the changes of L than A_U (see inset in Figure 4.8).

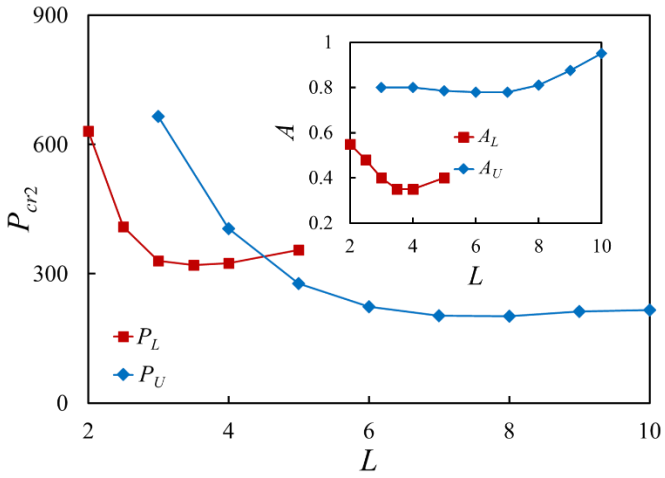

Figure 4.8 – Minimum critical pressure gradients, P_L and P_U, for unsteady regimes as a function of the channel period. The inset shows critical amplitudes, A_L and A_U, at which P_L and P_U occur for each of the channel period lengths.

4.4.4 Route to Chaos

As discussed previously, when the pressure driving is increased beyond a critical value, P_{cr2}, the flow undergoes a supercritical Hopf bifurcation resulting in unsteady, time-periodic oscillations in the fluid velocity throughout the channel. This periodic regime is

characterized by a single fundamental frequency. At even higher pressure drops, the flow undergoes a second Hopf bifurcation leading to a quasi-periodic regime with two fundamental frequencies. With continued increases to the pressure drop, the flow experiences further Hopf bifurcations, each adding a new frequency to the system, as the flow transitions to chaos. This is known as the Ruelle-Takens-Newhouse scenario of the onset of chaotic flow. It has been shown that after the third bifurcation, the flow exhibits chaotic behavior.[141, 142]

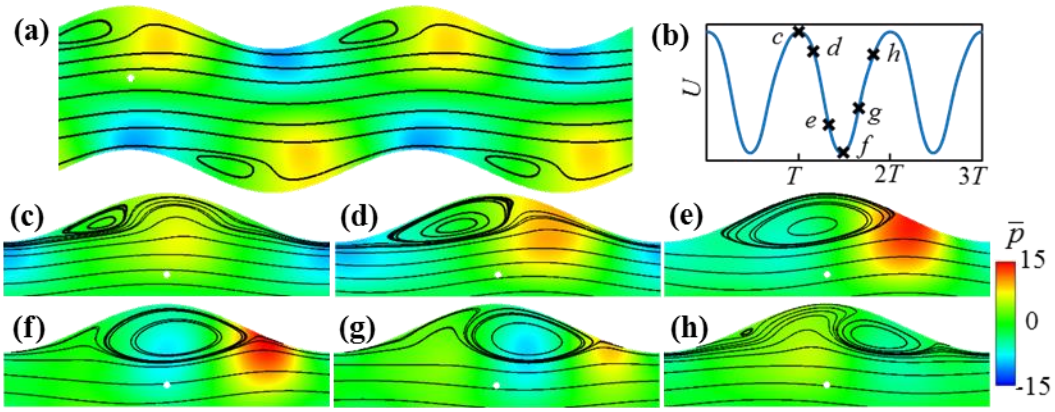

Figure 4.9 – Streamlines and pressure field in *A* = 0.3, *L* = 4 and *P* = 600 channel.

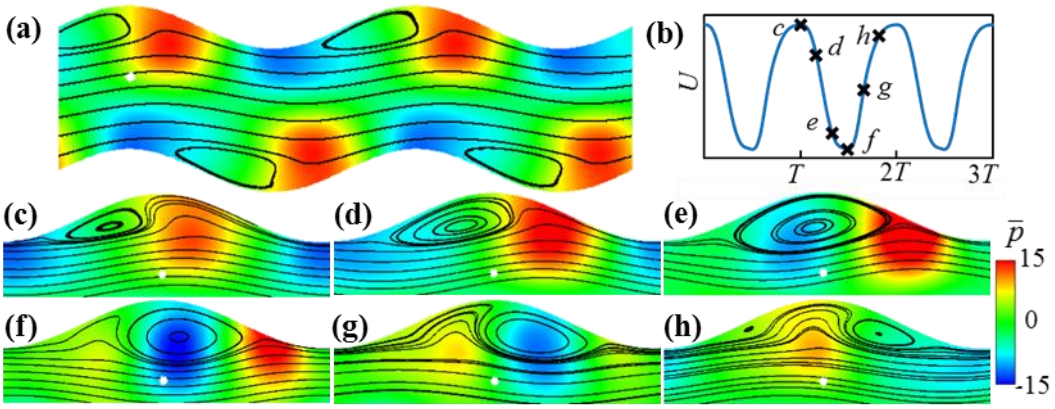

Figure 4.10 – Streamlines and pressure field in *A* = 0.3, *L* = 4 and *P* = 900 channel.

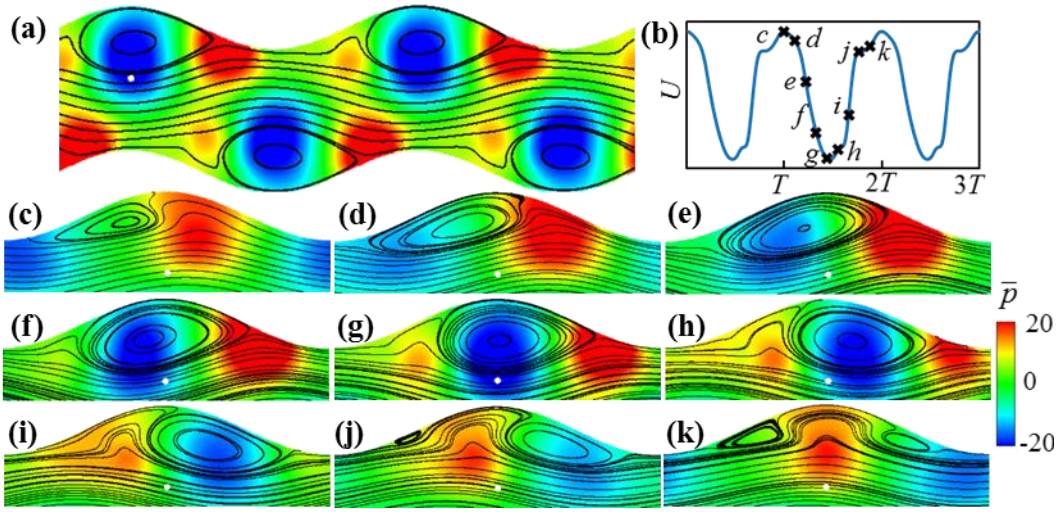

Figure 4.11 – Streamlines and pressure field in A = 0.3, L = 4 and P = 1800 channel.

After transitioning to unsteady flow, the small amplitude channel begins to experience an increased shedding frequency, and subsequently an increased fundamental frequency of the flow, as the pressure gradient is increased. For the initial increases in the driving pressure, the higher shedding frequency has little impact on how vortices evolve in the furrows. This can be seen by comparing Figures 4.4, 4.9, 4.10 and 4.11 which contain snapshots of a channel with $A = 0.3$ and $L = 4$ at $P = 400$, $P = 600$, $P = 900$ and $P = 1800$ respectively. In these snapshots we see that while there is an increase in the magnitude of the pressure field, the vortices maintain the same generation-growth-contraction cycle as the pressure gradient is increased from $P = 400$ to $P = 900$. Furthermore, this cycle continues to be synchronized across each furrow, resulting in the channel maintaining its spatial periodicity.

Although the higher pressure gradient does not affect the cycle each vortex undergoes, it does increase the size and strength of the vortices as they travel along the furrow. This is due to the larger flowrates along the center of the channel imparting more

energy into the vortex as it grows, which induces a larger vortex diameter. Using the maximum height of the vortex normalized by the height of the channel as the characteristic diameter, D_V we measure diameters of 0.61, 0.72, 0.80, and 0.94 for $P = 400$, $P = 600$, $P = 900$ and $P = 1800$ respectively. Therefore, at $P = 400$ the maximum diameter is approximately the same as the height of the furrow (Figure 4.4 (e)), but when P is increased to 1800, the vortex grows to nearly half the height of the channel. At this diameter, more than one third of the vortex is protruding out of the furrow (Figure 4.11 (g)), resulting it having an increased influence on the flow through the center of the channel. The effect of the increasing diameter in each of these four flows can be seen in Figure 4.12, which contains the time distributions of the u and v velocity components (normalized as the local Reynolds number) sampled from the location indicted in Figure 4.2. Here we see that for $P = 400$ when the vortex remains within the furrow, that both velocity components are nearly sinusoidal. When the vortex protrudes out into the flow at $P = 1800$, nearly reaching the location where the velocity is sampled, we see that both velocity components have transformed from sinusoidal shaped the shape seen in Figure 4.12 (d).

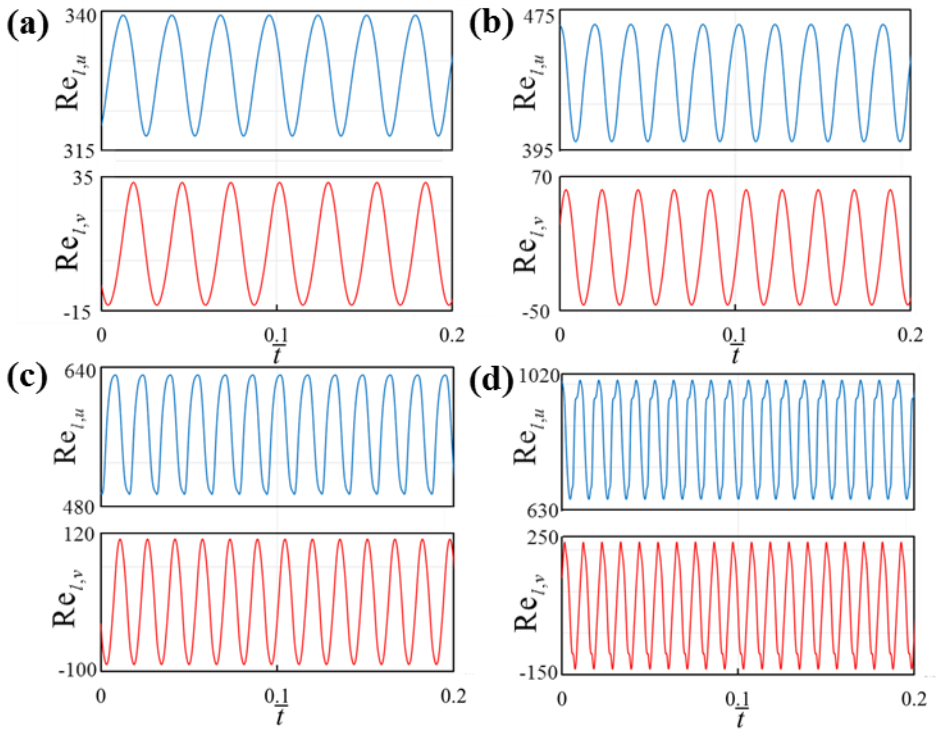

Figure 4.12 – Time distribution of the *u* and *v* velocity components sampled from representative location in *A* = 0.3 and *L* = 4 channel with (a) *P* = 400, (b) *P* = 600, (c) *P* = 900 and (d) *P* = 1800.

Although the time distribution of the local velocity undergoes a more complex pattern of oscillation, it maintains its single fundamental frequency. This can be seen in Figure 4.13, which contains the Fourier power spectrums of the u velocity components provided in Figure 4.12. Here we see that for all four driving pressures, the velocity indeed maintains a single fundamental frequency. This indicates that the flow in the system does remain periodic with fundamental frequencies of $\bar{f}_0 = 36$, $\bar{f}_0 = 48.6$, $\bar{f}_0 = 64.6$ and $\bar{f}_0 = 94.3$ for $P = 400$, $P = 600$, $P = 900$ and $P = 1800$, respectively. Along with increasing the fundamental frequency, larger driving pressures act to increase the energy in the super-harmonics frequencies. This results in the complex oscillatory pattern of the velocity components in the channel with $P = 1800$.

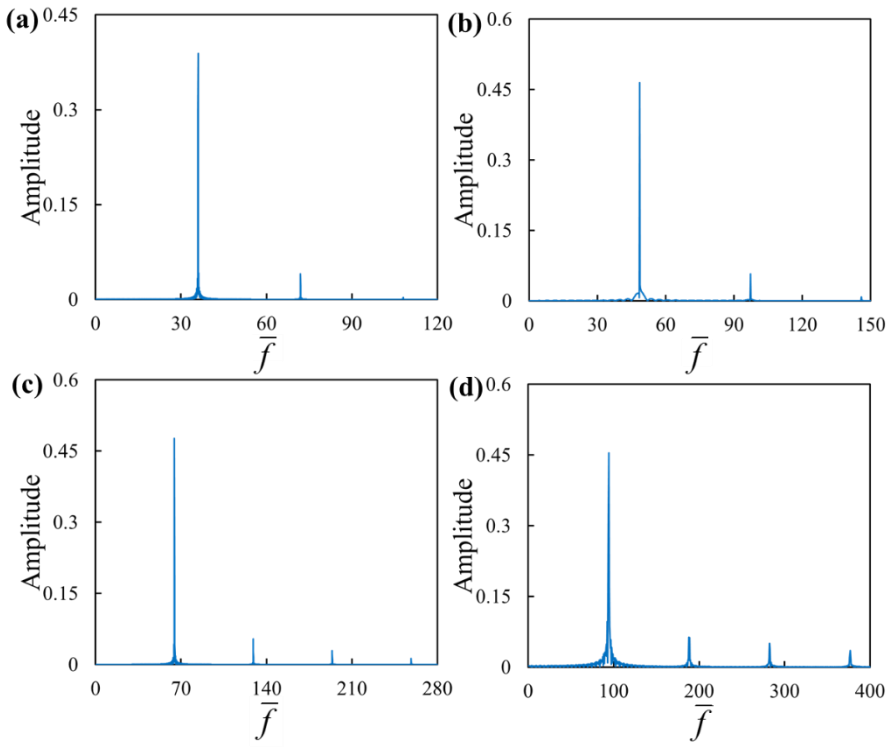

Figure 4.13 – Fourier power spectrum of *u* velocity component sampled from representative location in *A* = 0.3 and *L* = 4 channel with (a) *P* = 400, (b) *P* = 600, (c) *P* = 900, and (d) *P* = 1800.

The reconstructed pseudo-phase space obtained from the u velocity component for each of the four driving pressures is provided in Figure 4.14. Here we see that, as expected, the pseudo-phase space for each velocity distribution contains a limit cycle indicating the flow is periodic. As with the velocity components, the deformation seen in the limit cycle is a due to the contributions of the super-harmonic frequencies.

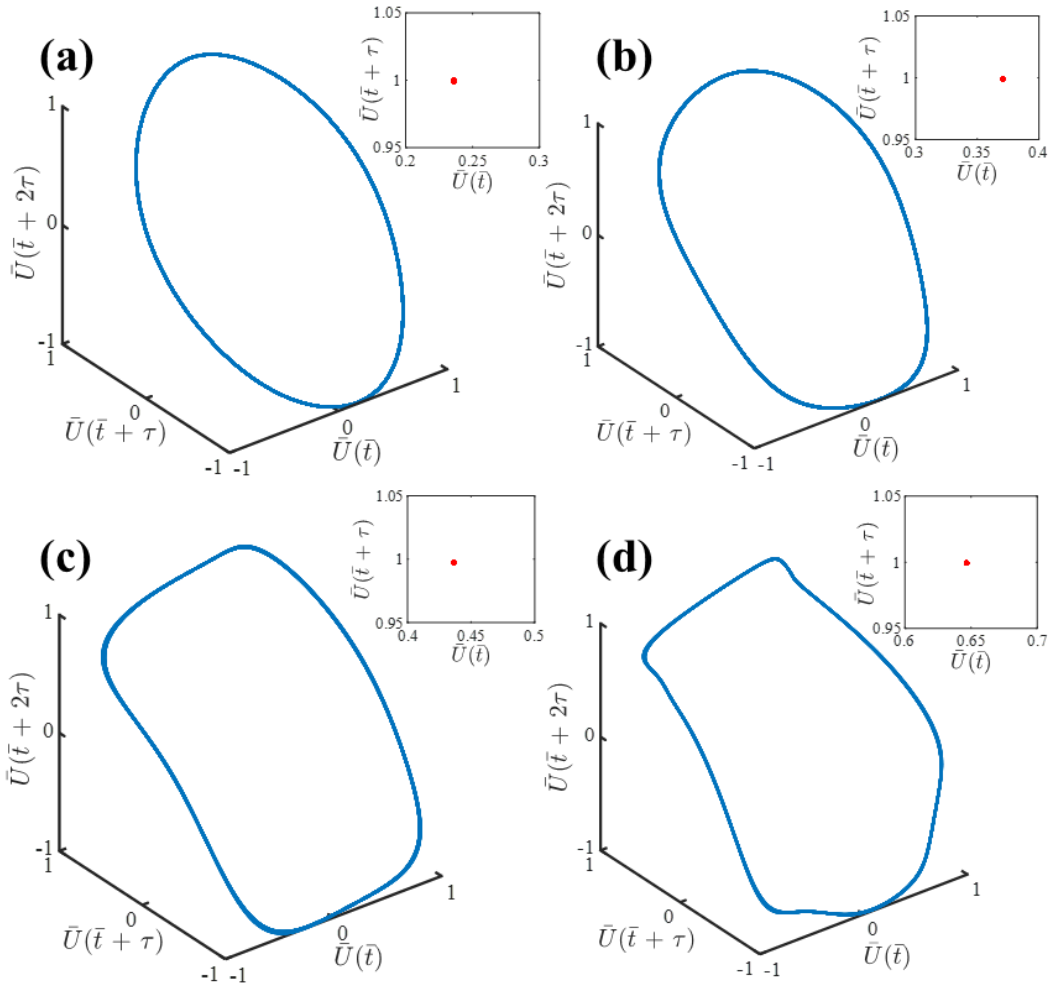

Figure 4.14 – Pseudo-phase space reconstructed from the time distribution of the *u* velocity component sampled from representative location in *A* = 0.3 and *L* = 4 channel with (a) *P* = 400, (b) *P* = 600, (c) *P* = 900, and (d) *P* = 1800. Poincaré sections provided in top right inset of each plot.

Increasing the pressure gradient beyond a critical value, P_{cr3} results in the flow undergoing a second supercritical Hopf bifurcation, leading to quasi-periodic oscillations in the fluid velocity characterized by two fundamental frequencies. As with the periodic regime, this regime is characterized by a vortex generation-growth-contraction cycle. Snapshots of a quasi-periodic flow in a channel with $A = 0.3$, $L = 4$ and $P = 2100$ are provided in Figure 4.15. Here we see in Figure 4.15 (i) and (j), as with the periodic regime, a new vortex is generated in the furrow, as the existing vortex shrinks. Unlike in the

periodic regime, however, this generation of a new vortex is quickly followed by the production of a second vortex at a new separation point along the wall. This separation point forms further up the wall peak, closer to its center. Due to their close proximity, these vortices rapidly combine (Figure 4.15 (k) and (c)). Once combined, the resulting vortex detaches from the second separation point, growing as it travels along the furrow (Figure 4.15 (d)). As the vortex travels to the right, fluid enters into the furrow to fill the area it previously occupied. Due to the high inertia of the fluid, the flow separates from the wall, forming an additional vortex (Figure 4.15 (e) and (f)). The formation of this vortex impedes the flow of fluid into the furrow, slowing the translation of the large vortex. When this occurs, the close proximity of the two vortices leads to the momentary formation of a third counter rotating vortex (Figure 4.15 (g)). This counter rotating vortex further reduces the flow into the furrow and, in doing so, sufficiently decreases the fluid inertia for the flow to reattach to the wall. When this occurs, the smaller vortices dissipate leaving only the large vortex to continue its translation to the left (Figure 4.15 (h)). As the vortex resumes contracting, the flow once again separates along the backside of the wall peak, creating another vortex (Figure 4.15 (i)). When this vortex forms, however, the rear of the shrinking vortex is sufficiently far away for fluid to enter the furrow unimpeded. With this fluid flowing in, the newly generated vortex grows as the previous vortex dissipates. (Figure 4.15 (j)).

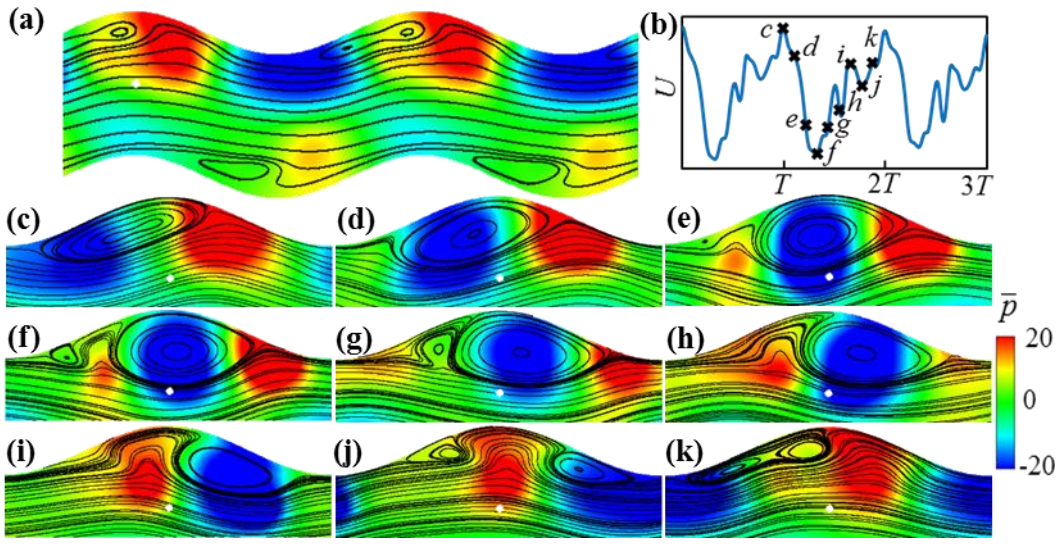

Figure 4.15 – Streamlines and pressure field in in *A* = 0.3, *L* = 4 and *P* = 2100 channel.

This generation of a new, temporary vortex is the result of the high flowrate in the channel causing vortices to generate faster than the previously generated one can dissipate. As a result, the newly generated vortex quickly dissipates as seen in Figure 4.15. Although, short-lived, the effects of this vortex introduces a second fundamental frequency into the system. In order to examine the variations in the velocity more closely, we have provided the time distribution of the velocity components in Figure 4.16 (a). Here, we see that the velocity distribution has the appearance of a periodic shape. However, due to the effect of the second fundamental frequency, these distributions will not repeat as they are quasi-periodic.

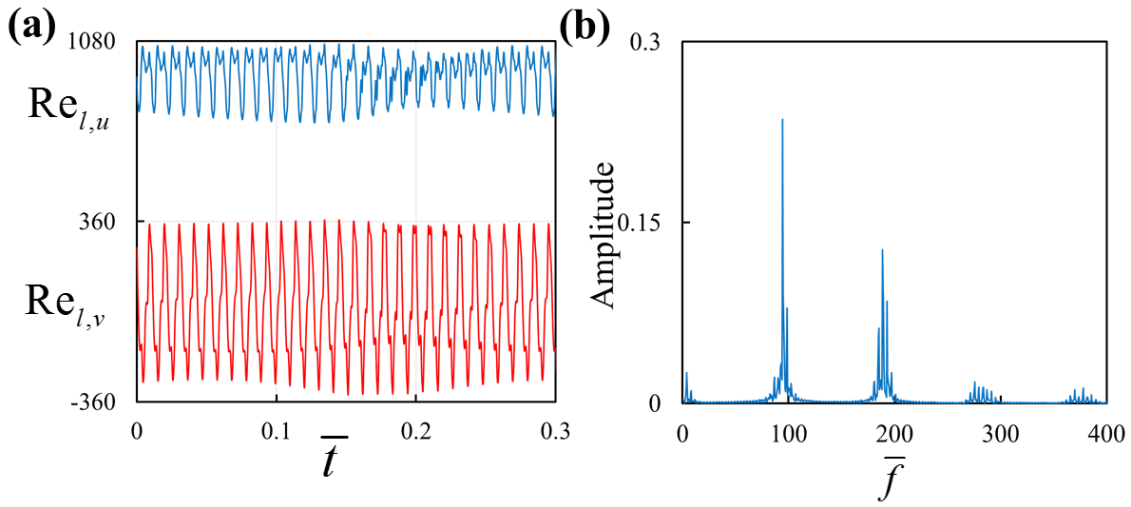

Figure 4.16 – Plots showing (a) the time distribution of the *u* and *v* components of the velocity and (b) the Fourier power spectrum of the *u* component sampled from a channel with *A* = 0.3, *L* = 4 and *P* = 2100.

In order to see the frequencies in the distribution, we have provided a plot of the Fourier power spectrum in Figure 4.16 (b). Here we see that the two fundamental frequencies and their linear combinations produce multiple peaks in the spectrum. The first fundamental frequency at $\overline{f} = 94$ still dominates the system, providing the time distribution with its nearly periodic shape. When we reconstruct the phase space, we see that, due to the second frequency, the limit cycle has been replaced with a limit torus. This can be seen in Figure 4.17. Here, we see that the two dimensional limit cycle has transformed into a three dimensional T^2 torus. As with the velocity distribution for $P = 1800$, the harmonic frequencies distort the shape of the attractor. Taking a Poincaré section, we obtain a two-dimensional closed line, rather than the single point as with the limit cycle, verifying that this is indeed quasi-periodic flow.

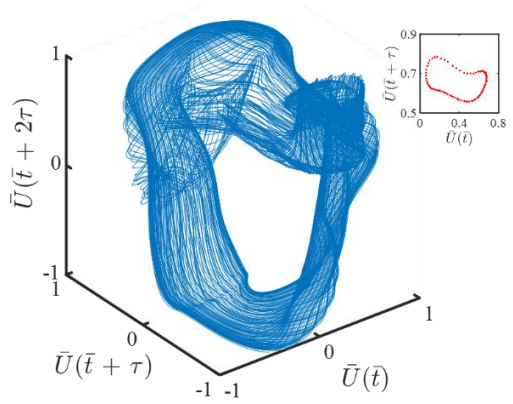

Figure 4.17 – Pseudo-phase space reconstructed from the time distribution of the *u* velocity component sampled from a channel with *A* = 0.3, *L* = 4 and *P* = 2100. Poincaré sections provided in top right inset the each plot.

As the pressure gradient increases further, beyond a fourth critical value denoted P_{cr4}, the flow bifurcates a third time causing the evolution of the vortices to become even more complex. This can be seen in Figure 4.18, which contains snapshots of the flow in a channel with $A = 0.3$, $L = 4$, and $P = 2500$. Here, we can see that no discernable frequency exists in the velocity distribution due to the three fundamental frequencies of the system. Furthermore, the snapshots show significant variation in the size, shape and number of vortices contained within the furrow.

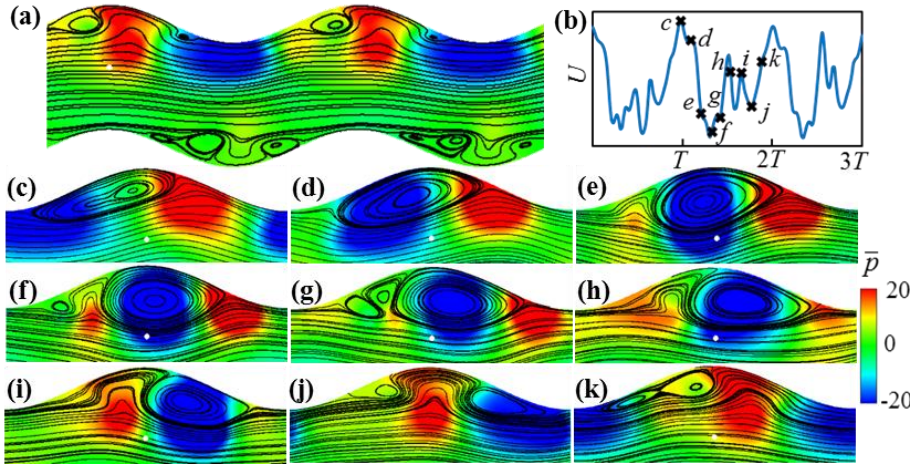

Figure 4.18 – Streamlines and pressure field in *A* = 0.3, *L* = 4 and *P* = 2500 channel.

Figure 4.19 (a) contains the time distribution of the velocity components. Here, we see the effects of the third fundamental frequency giving the distribution the appearance of random noise. Furthermore, when we view the Fourier power spectrum of the distribution, provided in Figure 4.19 (b), we find that the second and third fundamental frequencies are no longer discernable from the harmonics. When we reconstruct the pseudo-phase space, we see that, due to the inclusion of a third frequency, the limit torus has been transformed into a strange attractor. This can be seen in Figure 4.20. In the inset we have provided a Poincaré section obtained from the attractor. Here, we see that, due to the additional dimension of the attractor, the Poincaré section now contains an area filled with points, indicating that this is a indeed T^3 torus. From the work of Newhouse et. al., due to the sensitivity to initial conditions indicated by the presence of a strange attractor, this flow exibits the behavior of a chaotic system.[142]

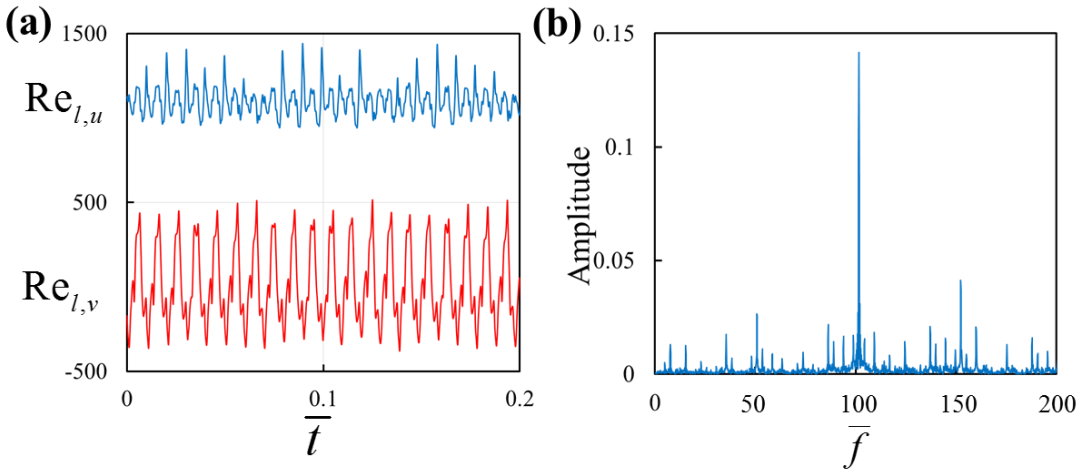

Figure 4.19 – Plots showing (a) the time distribution of the *u* and *v* components of the velocity and (b) the Fourier power spectrum of the *u* component from a channel with *A* = 0.3, *L* = 4 and *P* = 2500.

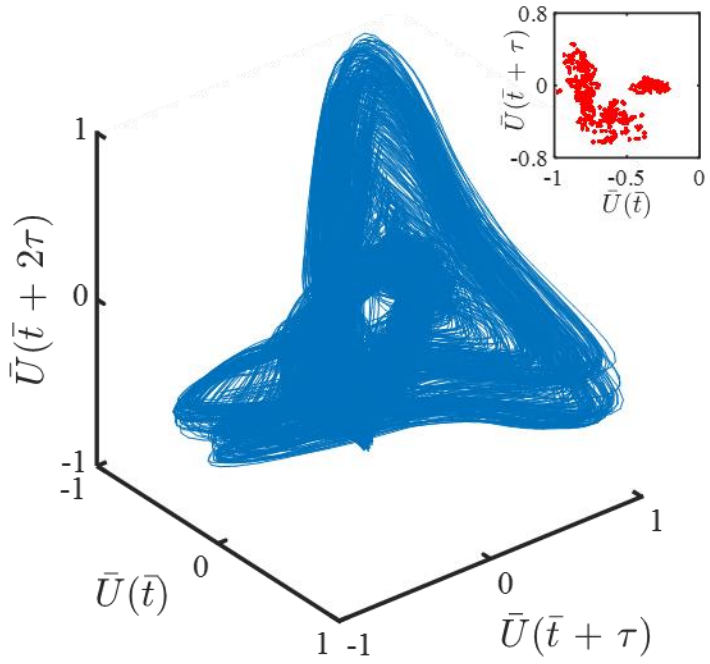

Figure 4.20 – Pseudo-phase space reconstructed from the time distribution of the *u* velocity component sampled from a channel with *A* = 0.3, *L* = 4 and *P* = 2500. Poincaré sections provided in top right inset the each plot.

In addition to the Hopf bifurcations experienced by the flow as the driving pressure increases, for certain larger amplitude channels the flow undergoes a period doubling bifurcation as the pressure drop increases. The effect of this bifurcation leads to a change in the evolution of vortices located in the furrows. We refer to the critical pressure gradient necessary to achieve this bifurcation at $P_{cr,pd}$. This can be seen in Figure 4.21, which contains snapshots of the flow after undergoing a period doubling bifurcation in a channel with $A=0.7$, $L=5$ and $P=700$. Here we see that, like the flow at $P=300$, as a new vortex is generated in the furrow, it grows and combines with the existing vortex eventually filling the entire furrow (*cf.* Figures 4.5 (c)-(h) and 4.21 (d)-(h)). As a new vortex is generated (Figures 4.5 (f) and 4.21 (i)), the cycle repeats for the flow with $P=300$, while the vortex evolution cycle continues for the flow at $P=700$. In this latter stage of the

cycle, the existing vortex is sufficiently small for fluid to continue flowing into the furrow unimpeded by the newly generated vortex (Figure 4.21 (j)). This forces the fluid entrained in the existing vortex out of the furrow, leading to its dissipation, while the new vortex grows behind it (Figure 4.21 (j) and (k)). As the growing vortex detaches from the wall, a new vortex is generated and the full cycle is repeated.

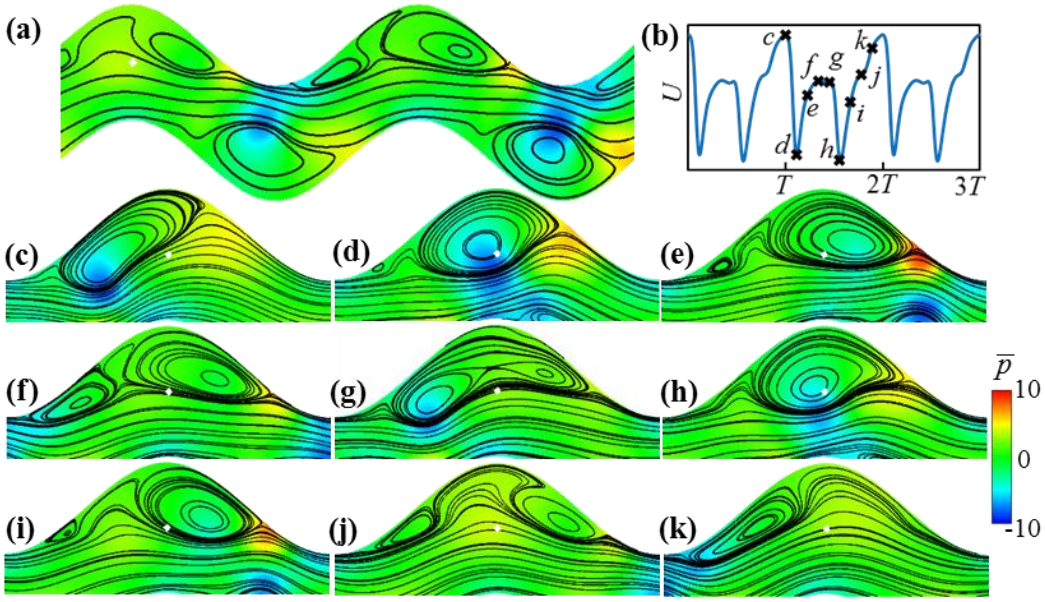

Figure 4.21 – Streamlines and pressure field in A = 0.7, L = 5 and P = 700 channel.

This second cycle doubles the length of the oscillation period, halving the fundamental frequency of the flow. The effect of this period doubling can be seen in the time distribution of the velocity components provided in Figure 4.22. Here, for comparison we show the distributions just before and just after transition at $P = 650$ and $P = 700$, respectively. In this figure we can see that the velocity at $P = 650$ completes slightly less than 10 cycles, while completing just over 5 cycles at $P = 700$. Furthermore, we see that the full cycle $P = 650$ closely resembles the corresponding half of the doubled cycle where the vortices in the furrows combine. When examining the Fourier power spectrum provided

in Figure 4.23 we see that, due to the period doubling, the fundamental frequency of the system has been halved, reducing it from $\overline{f} = 33.4$ at $P = 650$ to $\overline{f} = 17.6$ at $P = 700$. Here, the frequency is slightly larger than half due to its increase with increasing P for $P > P_{cr,pd}$.

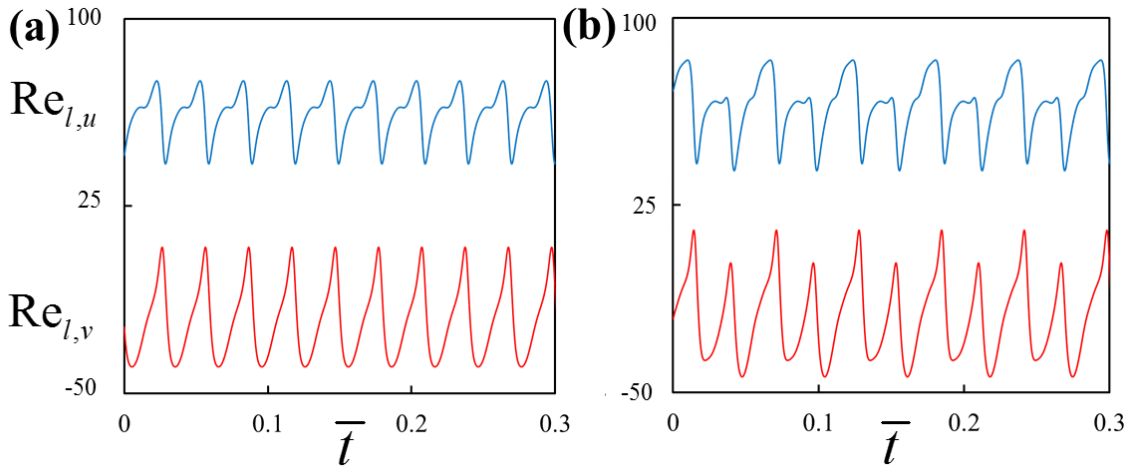

Figure 4.22 – Plots showing the time distribution of the *u* and *v* components of the velocity in a channel with *A* = 0.7, *L* = 5 at (a) *P* = 650 and (b) *P* = 700.

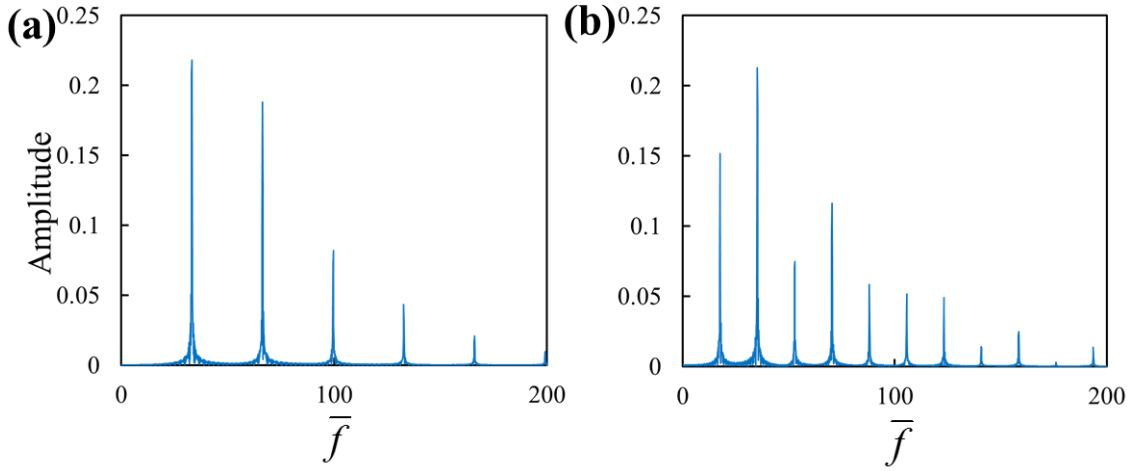

Figure 4.23 – Plots showing the Fourier power spectrum of the *u* component of the velocity from a channel with *A* = 0.7, *L* = 5 at (a) *P* = 650 and (b) *P* = 700.

When we reconstruct the pseudo-phase space using the u component of the velocity, we find that both flows contain a single limit cycle. This can be seen in Figure 4.24, which contains the pseudo-phase space for both flows along with a corresponding Poincaré section. Here we see that while both flows contain a limit cycle, the period doubled flow at $P = 700$ completes two loops before returning to its starting point, indicating that the flow has undergone a period doubling bifurcation. This is verified by the Poincaré section included in the inserts of the plots which contains two points where the limit cycle passes through the plane in each loop. The flow at $P = 650$, on the other hand, contains a single loop in its limit cycle and, as a result, a single point in its Poincaré section.

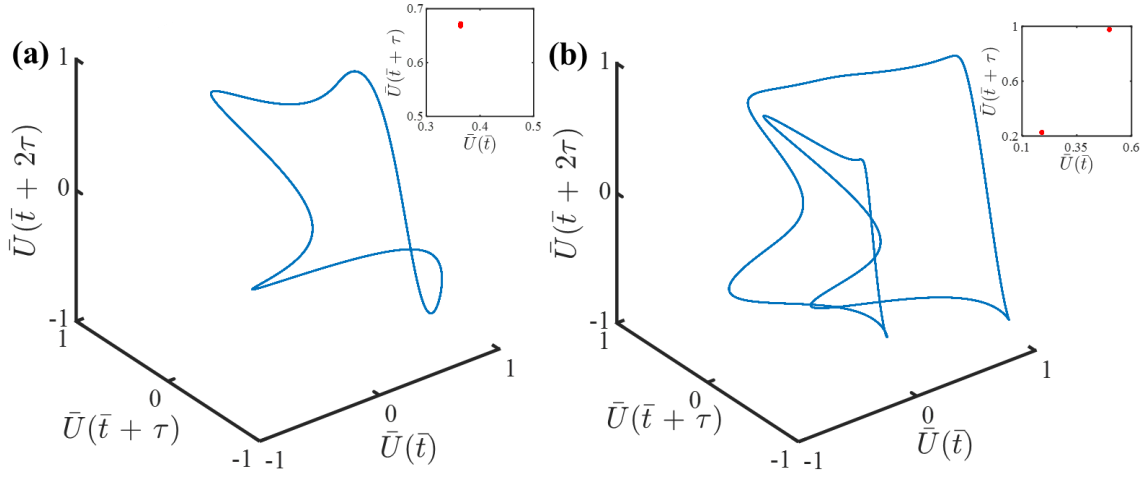

Figure 4.24 – Plots showing the pseudo-phase space reconstruction and the corresponding Poincaré sections for a channel with A = 0.7, L = 5 at (a) P = 650 and (b) P = 700.

As the pressure drop is increased further after the flow undergoes a period doubling bifurcation, the flow experiences a 2nd supercritical Hopf bifurcation for each geometric configuration investigated. This can be seen in the plots of the of the time distribution of the velocity components and Fourier power spectrum provided in Figure 4.25, which have

been obtained from a flow through a channel with $A = 0.7$, $L = 5$ and $P = 1100$. Here, we see that the distribution of the velocities have an appearance of a periodic shape. However, the addition of the second frequency has transitioned the distribution to quasi-periodic. Furthermore, when we examine the Fourier power spectrum, we see the two frequencies along with their harmonics.

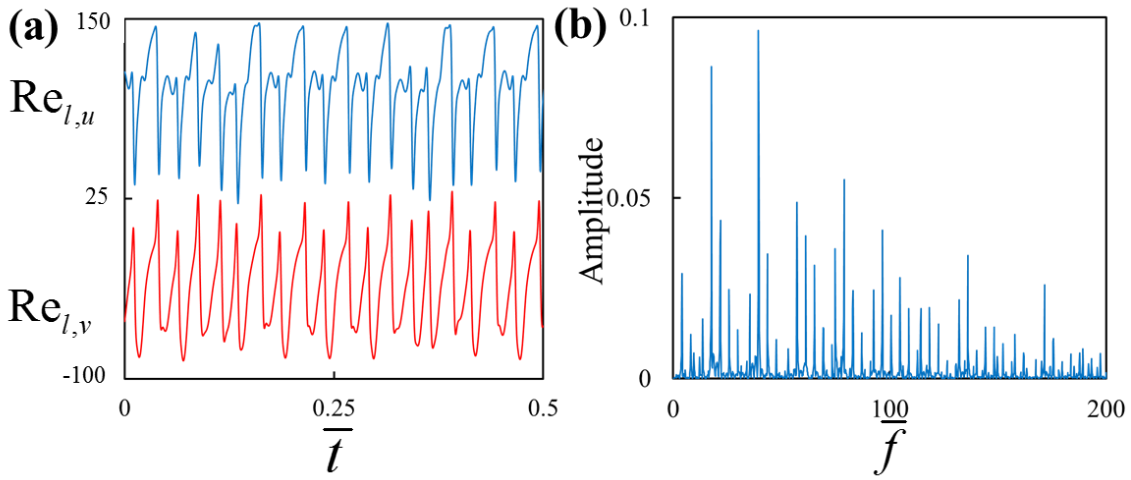

Figure 4.25 – Plots showing (a) the time distribution of the *u* and *v* components of the velocity and (b) the Fourier power spectrum of the *u* component from a channel with *A* = 0.7, *L* = 5 and *P* = 1100.

When reconstructing the pseudo-phase space from the u velocity component, we find that the attractor has taken the form of a limit torus, which can be seen in Figure 4.26. As stated previous, this is indicative of a Hopf bifurcation, which introduces a second fundamental frequency into the system. Examination of the Poincaré section verifies that this is indeed a limit torus, as the section contain multiple points defining a closed line. As with the flow in smaller amplitude channels, further increases in the driving pressure result in a third Hopf bifurcation as the flow follows the Ruelle-Takens-Newhouse scenario on its route to chaos.

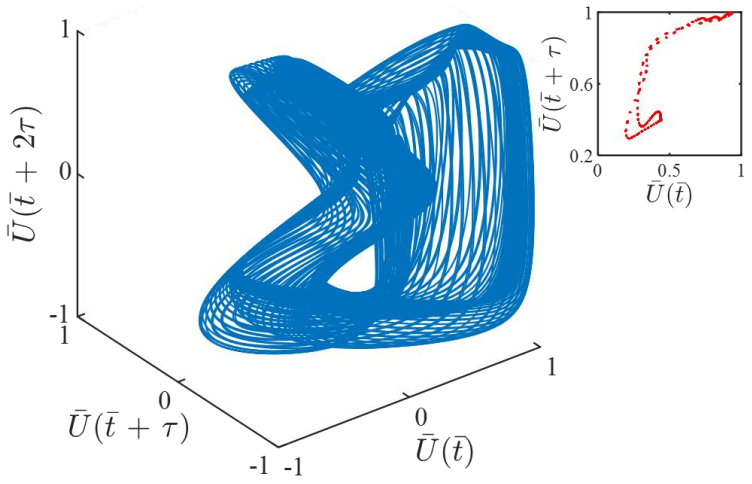

Figure 4.26 – Plot showing the pseudo-phase space reconstruction of the attractor and its corresponding Poincaré section for a channel with *A* = 0.7, *L* = 5 and *P* = 1100.

In order to understand how the geometric parameters and driving pressure influence the flow regime, we systematically varied these parameters while using the methods discussed above to determine the state of the flow. Specifically, we vary A between 0.2 and 1.0 at step sizes of 0.1 and P between 0 and 2500 at step sizes of 50 for period lengths of $L=3$, $L=4$ and $L=5$. Figure 4.27 shows the phase map for $L=3$. Here we see that for pressure drops less than $P=2500$, only two of the wall amplitudes, $A=0.7$ and $A=0.8$, achieve quasi-periodic flow, which occurs at $P=1100$ and $P=1500$, respectively. These correspond to Reynolds numbers of $\mathrm{Re}=67.1$ for $A=0.7$ and $\mathrm{Re}=54.4$ $A=0.8$. Furthermore, the critical pressure gradient P_{cr4} is not found for any of the amplitudes for the range of driving pressures $0\le P\le 2500$. The majority of the wall amplitudes fail to reach P_{cr3} due to the lower velocities resulting from the larger relative wall amplitudes. Therefore, we find that decreasing the wall period length L has a stabilizing effect on the flow.

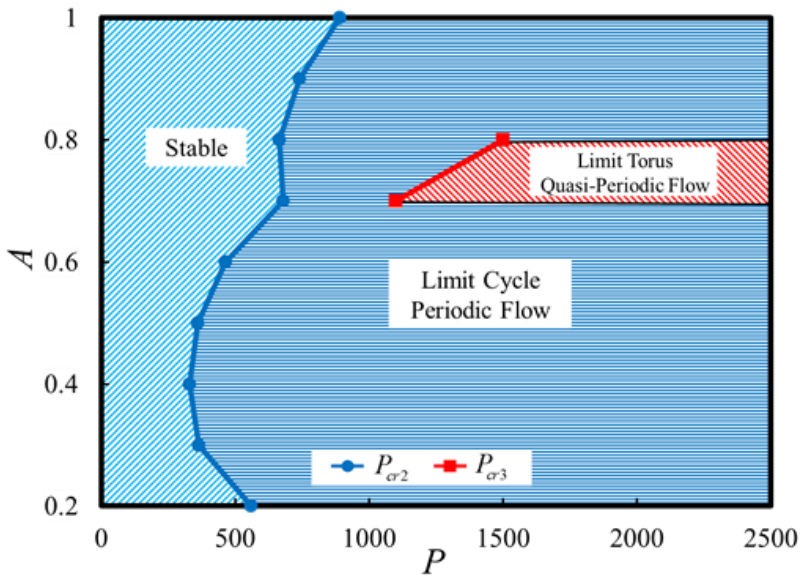

Figure 4.27 – Phase map of flow regimes for period length *L* = 3.

When L is increased to $L=4$, the flow achieves each of the regimes discussed above within the range of driving pressures investigated. This can be seen in Figure 4.28, which contains the flow regime map for $L=4$. Here we see that, for smaller amplitude channels, P_{cr3} contains a minimum at $A=0.5$ and $P=700$. Furthermore, the flow reaches the quasi-periodic regime for each of the wall amplitudes with $A \le A_m$. Additionally, for $A=0.4$ and $A=0.5$, this period length achieves chaotic flow, with critical pressure gradients $P_{cr4}=1900$ and $P_{cr4}=2250$, respectively. These correspond to $\mathrm{Re}=371$ for $A=0.4$ and $\mathrm{Re}=269$ for $A=0.5$. For larger wall amplitudes where $A > A_m$, each of the flows experiences a period doubling bifurcation. While for $A=0.7$ and $A=0.8$, this period doubling bifurcation is followed by a second Hopf bifurcation at $P_{cr3}=2300$ and $P_{cr3}=2400$, respectively.

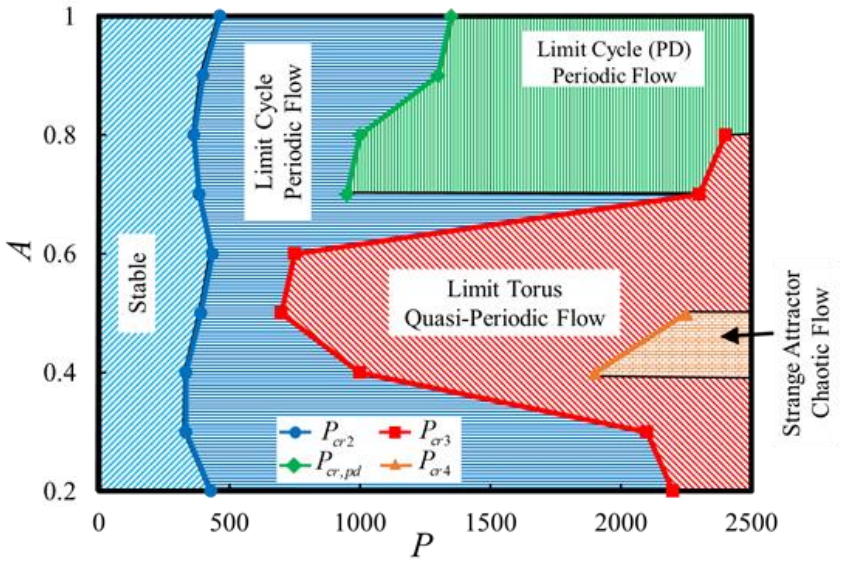

Figure 4.28 – Phase map of flow regimes for period length of *L* = 4.

Similar to those with $L=4$, for the range of amplitude and driving pressures investigated, each of the flow regimes can be found when $L=5$ as seen in Figure 4.29. Here we see that for all amplitude of $0.2 \le A \le 1$ the third critical pressure gradient within the range of pressures $0 \le P \le 2500$. The minimum critical pressure gradient for the second Hopf bifurcation occurs at $A=0.4$ for a pressure drop of $P_{cr3}=550$. Furthermore, in the range of pressure gradients investigated each of the channels with $0.2 \le A \le 0.8$ achieves chaotic flow. The minimal critical pressure gradient for this third Hopf bifurcation occurs for $A=0.4$ at $P_{cr3}=1400$. For this period length, the minimum flowrate necessary to induce chaotic flow is found in $A=0.8$ at a Reynolds number of $\mathrm{Re}=85$.

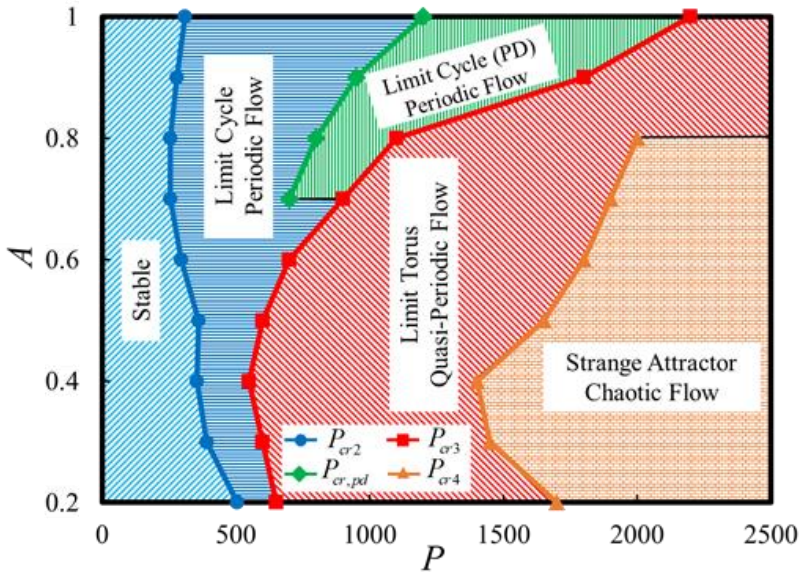

Figure 4.29 – Phase map of flow regimes for period length of L = 5.

4.4.5 Frictional Losses

To quantify the effect of wall structure on the viscous dissipation in a wavy channel, we calculated the friction factor $f = 6P/\mathrm{Re}^2$ that characterizes viscous losses in the channel flow. The friction factor is plotted in Figure 4.30 as a function of the applied pressure gradient P for channels with period lengths of $L = 3$, $L = 4$ and $L = 5$ at several wall amplitudes A. In this figure, we also plot the friction factor in a straight channel $f = 6/P$. As can be expected, the wavy channel walls increase the friction factor compared to the straight channel and this increase is more significant for channels with larger A. When the flow is in the unidirectional regime the friction factor decreases with P at a rate that is close to that of the decrease in a straight channel. When the flow transitions to the circulatory regime, the decrease with P slows down and, for $P > P_{cr2}$, f levels off for the wavy geometry while it continues decreases for the straight channel.

The dependence of f with P shown in Figure 4.30 can be related to an increase of viscous dissipation taking place in the flow due to the development of vortices in the channel furrows. Moreover, the dissipation increases even more when the flow becomes unsteady, thereby requiring greater pressure gradients to transport the fluid with the same flow rate. However, after the initial Hopf bifurcation and transition to unsteady flow, subsequent bifurcations do not act to further increase the effects of the channel geometry.

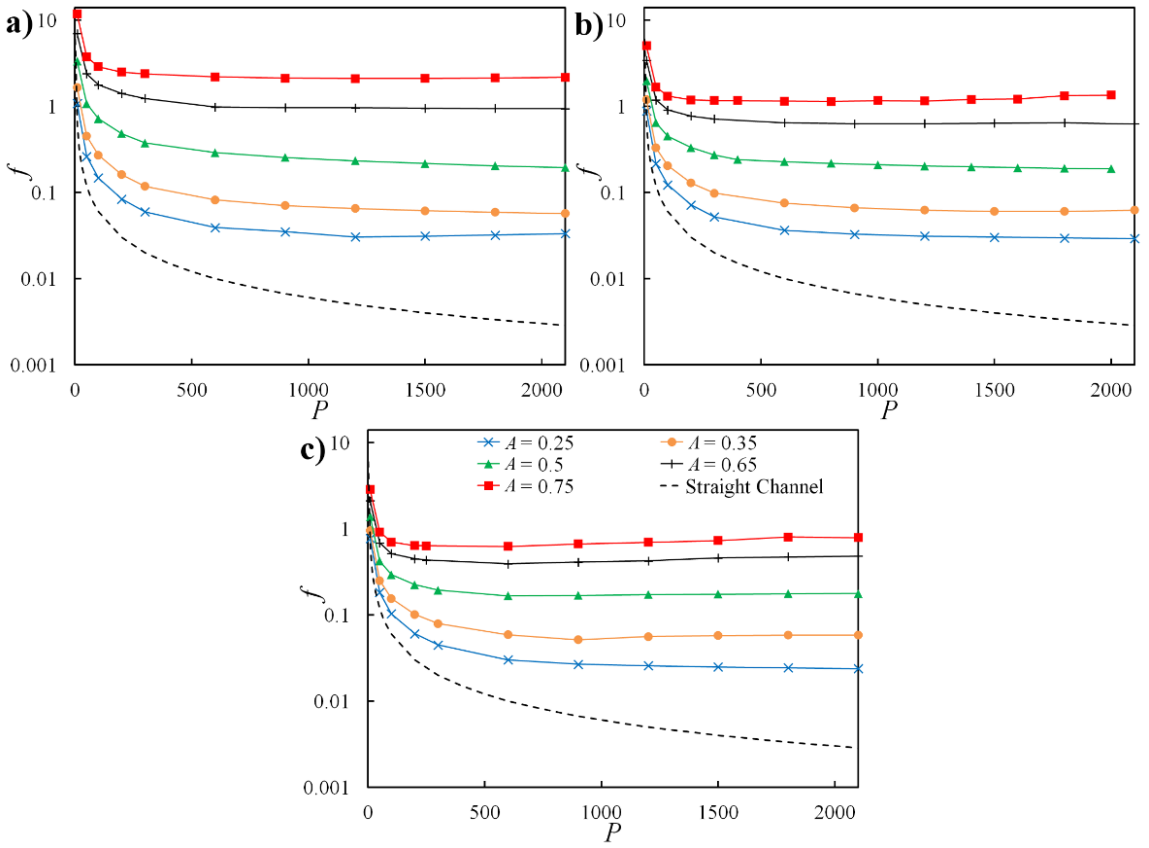

Figure 4.30 – Channel friction factor, *f*, as a function of normalized pressure gradient in a wavy channel at different wall amplitudes for wall period lengths of (a) *L* = 3, (b) *L* = 4 and (c) *L* = 5.

4.5 Summary

We used two-dimensional computer simulations to investigate laminar pressure-driven flow in a channel with sinusoidal walls. In particular, we probed the effects of wall amplitude and period on the development of different flow regimes and the onset of chaotic flows within the wavy channel. The results are summarized using flow regime diagrams in terms of the driving pressure gradient and the channel wall amplitude, which are provided in Figures 4.7, 4.27, 4.28 and 4.29. The first of these diagrams indicates the boundaries between conditions at which a unidirectional flow, a circulatory flow, and an unsteady flow emerge in wavy channels, while the other three provide the boundaries between time-period, as well as two and three frequency quasi-periodic flows. Due to its sensitivity to initial conditions, indicated by the strange attractor in the pseudo-phase space, this three frequency quasi-periodic flow exhibits the characteristics of chaos.[142]

Through our initial investigations, we found that at a critical pressure drop, P_{cr1}, the flow transitions to circulatory while remaining steady, and at a second critical pressure drop, $P_{cr2} > P_{cr1}$, the flow transitions to time-periodic unsteady motion through a supercritical Hopf bifurcation. Here, we considered channels with $0.125 \le A \le 1$ and $2 \le L \le 10$. We note that for the channel geometries outside of the investigated range this behavior may not hold. In our subsequent investigations, we found that the flow undergoes additional supercritical Hopf bifurcations at a third and fourth critical pressure drop, $P_{cr4} > P_{cr3} > P_{cr2}$, with each of these bifurcations adding a new fundamental frequency to the system. Moreover, we found that for certain large amplitude channels, the flow undergoes a period doubling bifurcation at a critical pressure gradient $P_{cr,pd} > P_{cr2}$.

The simulations reveal that the transitions to each of the unsteady flow regimes exhibits a nontrivial dependence on the channel wall amplitude. The transition is related to an interplay among fluid inertia, disturbances introduced by wavy walls, and channel confinement. For small amplitude channels, the unsteady flow is characterized by vortex shedding and the absence of trapped vortices. New vortices periodically form within the channel furrows and, after they grow sufficiently large, are shed and transported downstream by the flow. In channels with larger wall amplitudes, confinement effects result in the trapping of vortices, which oscillate within the furrows as shed vortices combine with them. These oscillations are accompanied by periodical changes in vortex size.

We have identified two channel geometries minimizing the magnitude of the critical pressure gradient leading to the unset of an unsteady flow. In the first case, the wall amplitude is $A = 0.35$ and the period is $L = 0.35$, yielding $P_{cr2} = 320$ and $\mathrm{Re} = 128$. The second minimum occurs for channels with $L = 8$ and $A = 0.81$, in which case $P_{cr2} = 202$ and $\mathrm{Re} = 81.2$. The latter pressure is the minimum pressure at which an unsteady flow can be generated in a wavy channel.

In our investigation of the subsequent bifurcations in the flow after transition to unsteady, we found a strong dependence of the critical pressure drops on the period length of the channel. Due to this dependence, we found only two amplitudes which contain P_{cr3} within the range of pressure drops investigated ($0 \le P \le 2500$). For $L = 5$, on the other hand, each of the amplitudes examined contained P_{cr3} within the range of pressures studied. Additionally, the range of amplitudes $0.2 \le A \le 0.8$ contain critical pressure

gradients $P_{cr4} \geq 2500$. From our simulations we were able to determine the minimum P_{cr3} and P_{cr4} for the range of parameters investigated which are $P_{cr3} = 550$ and $P_{cr4} = 1400$, both of which occur in a channel with $A = 0.4$ and $L = 5$. Furthermore, we found that the asymmetric wavy wall geometry is capable of inducing the onset of chaotic flow at a minimum Reynolds number of $\mathrm{Re} = 85$ in a channel with $A = 0.8$ and $L = 5$.

Lastly, we characterized the effects of the wavy walled geometry in terms of the viscous losses it generates. We showed that the geometry of the channel induces significant friction coefficients compared to a straight channel. Further, we demonstrated that the friction coefficient is nearly independent of the driving pressure when the flow is unsteady. Moreover, we showed that, after the initial bifurcation and transition to unsteady flow, additional bifurcations do not induce significant changes in the friction coefficient.

The unsteady flow emerging in wavy channels at relatively low flow rates induces constantly evolving local flow circulations and, therefore, can be potentially harnessed for enhancing heat and mass transport, key processes of many practical applications. Since this unsteady flow remains laminar even when exhibiting chaotic behavior, we anticipate the mixing enhancement can be accomplished for a relatively low increase in friction losses compared to a turbulent flow with similar transport characteristics.

CHAPTER 5. HEAT TRANSFER

5.1 Introduction

Although a substantial amount of research has been conducted to better understand the effects of wavy walled channels on heat and mass transfer, we are still missing a comprehensive and systematic picture of how the heat transfer changes for a wide range of system parameters. In this chapter, we systematically investigate laminar pressure driven flow in two-dimensional wavy channels with asymmetric sinusoidal walls. We probe the dependence of the heat transfer occurring in the channel on the amplitude and period of the walls and the magnitude of the pressure drop driving the flow. Our investigation begins by examining the heat transfer occurring at low flow rates when the flow is steady. Next, larger flow rates where the flow experiences time-periodic oscillations are studied. Lastly, the heat transfer enhancement is weighed against the cost of increased frictional losses induced by the wavy geometry using a thermal-hydraulic performance factor in order to determine the overall performance of wavy walled channels.

5.2 Computational Setup

Please refer to Section 2.6.3 for a detailed discussion of simulation parameters used in this investigation. Before starting our investigation into the heat transfer enhancement, four simulations of heat transfer in a wavy channel were performed with various grid sizes to determine the necessary grid spacing for our simulations. The parameters of the simulations were $P = 50$, $A = 0.35$ and $L = 4$ with grid sizes corresponding to $h = 20$, $h = 40$, $h = 60$, and $h = 80$ (in LB units). A plot of Nu_l along the top wall for all four

grid sizes is provided in Figure 5.1. It can be seen in the plot that all four grid sizes yield nearly identical results with the exception of the points obtained near $x/l = 0.67$ with $h = 20$, which deviate slightly from the results obtained with other grids. Table 5.1 contains the values of $\mathrm{Nu_m}$ and Re calculated for each grid resolution along with their percent differences from the values obtained for $h = 80$. It can be seen in this table that the values of $\mathrm{Nu_m}$ and Re obtained using $h = 40$ nodes only differ from those obtained using $h = 80$ by 0.09% and 0.14%, respectively. Because the grid with $h = 40$ nodes provides nearly identical results with those of higher resolution at significantly lower computational costs, we used this grid size in our investigation.

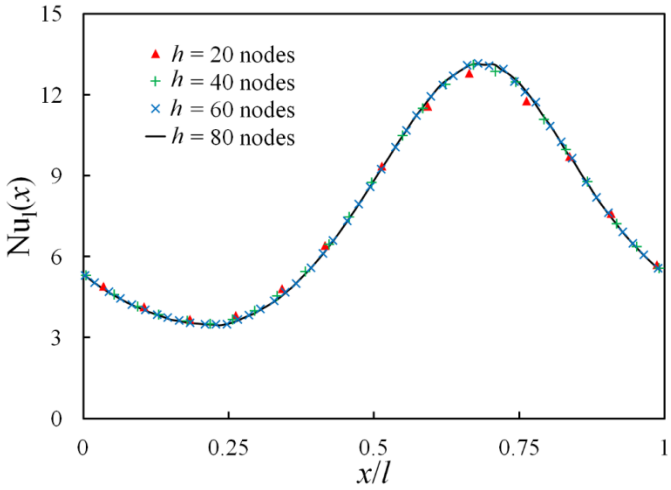

Figure 5.1 – Local Nusselt number Nu_l across top wall of channel for various grid sizes obtained from grid independence tests with P = 50, A = 0.35 and L = 4.

Table 5.1 – Results from grid independence test with P = 50, A = 0.35 and L = 4.

Nodes	$\mathrm{Nu_m}$	% Change	Re	% Change
20	8.132	0.0277	28.10	1.41
40	8.135	0.0857	28.50	0.144
60	8.141	0.0736	28.54	0.0196
80	8.148	-	28.55	-

5.3 Results and Discussion

Pressure-driven flow through sinusoidally-shaped channels results in three unique flow regimes which we refer to as unidirectional, circulatory, and unsteady. At low flow rates, in the unidirectional regime, the flow follows the shape of the channel. As the flow rate increases and the flow transitions to circulatory, steady vortices form in the furrows of the channel walls. Further increases of the flow rate leads to an unsteady flow characterized by a time dependent vortex topology. A more detailed discussion of these different flow regimes can be found in Chapter 4.

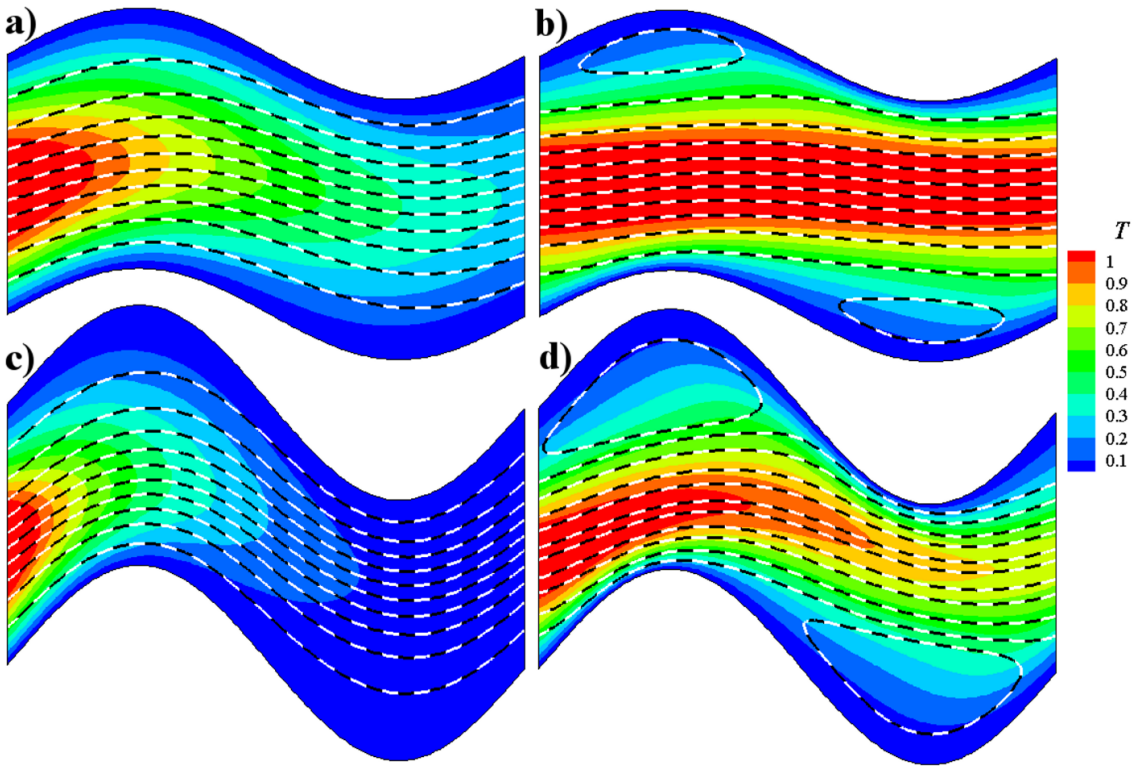

Figure 5.2 – Temperature distributions and streamlines for unidirectional and circulatory flows in (a) A = 0.35, L = 4 and P = 10 (b) A = 0.35, L = 4 and P = 100, (c) A = 0.75, L = 4 and P = 10 and (d) A = 0.75, L = 4 and P = 100.

5.3.1 Steady Flow Regimes

Figure 5.2 shows the temperature distribution and streamlines for both small and large amplitude wavy walls ($A = 0.35$ and $A = 0.75$) in the unidirectional and circulatory flow regimes. For small amplitude channels with unidirectional flow (Figure 5.2 (a)), the streamlines closely follow the channel shape. This leads to the heated fluid located in the center of the channel, which we refer as the hot fluid core, remaining near the center of the channel and away from the cold walls, resulting in a minor increase in Nu_m compared to a straight channel. When the wall amplitude is increased, the fluid deviates from the channel geometry, causing the flow streamlines converge closer to the crest and trough of the lower and upper walls, respectively (Figure 5.2 (c)). As a result, the hot fluid at the core is brought closer to the cold walls, increasing Nu. When the flow rate increases and the flow transitions to the circulatory regime, the formation of vortices focuses the core flow along the midplane of the channel (Figure 5.2 (a) and (d)). This further results in the heated fluid being brought closer to the walls near the crest and troughs of the lower and upper walls, respectively.

To gain insight into the dependence of the heat transfer on *P*, *A*, and *L*, we systematically varied these parameters and plotted the resulting $\mathrm{Nu}_l(x)$ along the top wall of a single period as well as Nu_m across the entire channel. The plots in Figure 5.3 show the dependence of Nu_l and Nu_m on *P* for small and large amplitude channels, respectively. It can be seen in these two figures that as *P* increases, the local Nusselt number experiences increasingly larger variations with the minimum and maximum values corresponding to the peak and trough of the top wall, respectively. The increase in Nu_l

near $x/l \approx 0.67$ as P increases is the result of the fast flowing fluid which has a higher temperature being squeezed into the midplane of the channel as the flowrate increases (Figure 5.2 (b) and (d)). This leads to the hot fluid coming close to the cold wall near the trough of the upper wall, increasing Nu_l at that location.

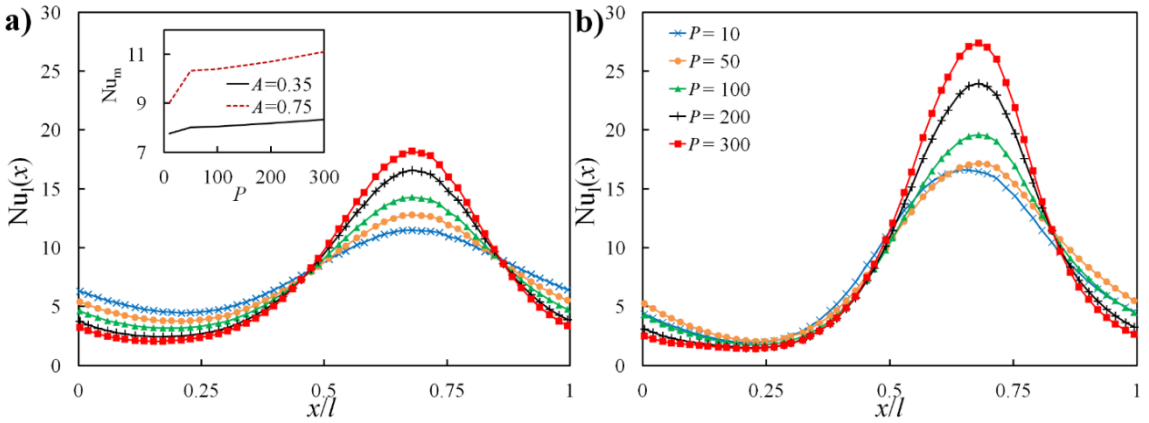

Figure 5.3 – Local Nusselt number Nu_l along top wall of single wall oscillation period for varying values of P in the steady flow regimes. Channel geometries kept constant at (a) A = 0.35, L = 4 and (b) A = 0.75, L = 4. Inset of the left plot contains Nu_m corresponding to each line in the main plots.

When the flow becomes circulatory, the formation of stationary vortices further inhibits the transfer of heat to the walls along the furrows. This is due to the vortices focusing the flow along the midplane. Additionally, since they are stationary, diffusion is the only mechanism for heat in the fluid moving downstream to be transported into the vortices. With diffusion being a slow transport process, the majority of the thermal energy is convected downstream with a relatively small amount diffusing into the vortices and reaching the wall of the furrows. Because of this, the vortices act as a barrier, decreasing the heat transfer along the wall of the furrow.

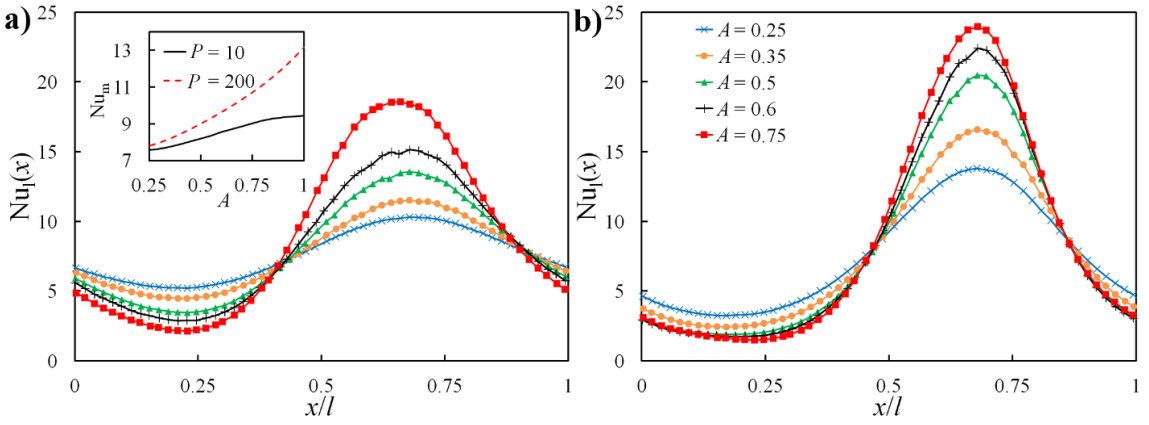

Figure 5.4 – Local Nusselt number Nu_l along top wall of single wall oscillation period for various A in the steady flow regimes with $L = 4$. P held constant at (a) $P = 10$ and (b) $P = 200$. Inset of the left plot contains Nu_m corresponding to each line in the main plots.

For both the unidirectional and circulatory flow regimes the increasingly larger values of Nu_l near $x/l \approx 0.67$ are accompanied by decreases in Nu_l around $x/l \approx 0.33$ as P increases. As a result, Nu_m only undergoes minor increases with increasing P (see inset in Figure 5.3 (a)). This indicates that in the steady flow regimes, the heat transfer rate is only weakly dependent on P, and subsequently the flow rate. The significantly higher Nu_m for the larger amplitude compared to the smaller amplitude indicates a strong dependence of heat transfer on the wall amplitude.

Figure 5.4 (a) and (b) show Nu_l and Nu_m in the unidirectional and circulatory regimes respectively for several amplitudes and constant pressures $P = 10$ and $P = 200$, respectively. Similar to the effect of increasing P, the variations in Nu_l undergo increasingly larger changes as A increases. When the flow is unidirectional, the location of the maximum Nu_l moves to the left with increasing A. For circulatory flow, the maximum Nu_l no longer depends on A, and remains near $x/l \approx 0.67$. When increasing P, the overall

shape of Nu_l remains unchanged while the increasingly larger values of Nu_l near the trough of the wall are offset by the decreases around the crest. Alternatively, as *A* is increased, Nu_l experiences considerable changes in its shape as its values near the trough and crest increase and decrease, respectively. At small *A*, the line resembles a sinusoid and as *A* increases the line transforms to have a prominent crest with a shallow trough. Because of this, the increases in Nu_l are no longer offset by the corresponding decreases leading to an increase in Nu_m as *A* increases. This can be seen in the inset of Figure 5.4 (a). This dependence is significantly stronger for circulatory flow than unidirectional flow, which accounts for the noticeable increase in Nu_m seen in the inset of Figure 5.3 (a) when $A = 0.75$ transitions from unidirectional flow at $P = 10$ to circulatory flow at $P = 50$.

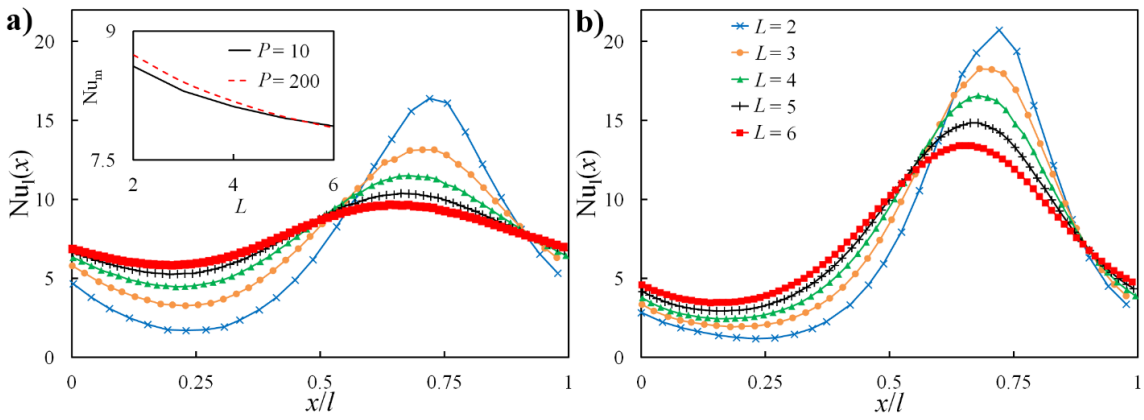

Figure 5.5 – Local Nusselt number Nu_l along top wall of single wall oscillation period for varying values of *L* in the steady flow regimes. Other parameters kept constant at (a) *A* = 0.35, *P* = 10 and (b) *A* = 0.75, *P* = 200. Inset of the left plot contains Nu_m corresponding to each line in the main plots.

Figure 5.5 (a) and (b) show the Nu_l distribution for several values of *L* with $A = 0.35$ and $P = 10$, and with $A = 0.75$ and $P = 200$, respectively. It can be seen in these plots that as *L* decreases, the magnitude of the variation in Nu_l increases. As with

increasing *A* and *P*, this is the result of the streamlines being unable to follow the sinusoidal shape of the channel as *L* decreases, causing the heated fluid at the core to move closer to the cold walls. For both $P = 10$ and $P = 200$, the lines intersect in the vicinity of $x/l \approx 0.91$ and $x/l \approx 0.81$, respectively. This indicates that the location where the hot fluid begins to diverge from the wall is dependent on *P*, but not on *L*, with larger *P* resulting in faster divergence. At the section of the channel where Nu_l is increasing with *x*, the lines do not maintain a common intersection point. Instead, Nu_l shifts to the right as *L* decreases. This is due to the flow being focused along the midplane as *L* decreases. This focusing of the flow results in the hot fluid remaining far from the wall near the furrows, but coming much closer near the wall peak, which leads to the wide trough and narrow crest in the line representing the smaller period $L = 2$. Unlike the effects of increasing *P* and *A*, Nu_m decreases as *L* increases. This is a result of the relative amplitude decreasing as *L* increases and *A* remains constant.

5.3.2 Unsteady Flow Regime

As *P* is increased beyond a critical value, the flow transitions to an unsteady regime. This regime is characterized by the shedding of vortices from the troughs and crests of the upper and lower walls, respectively, which induces periodic variations of the fluid velocity and temperature distribution throughout the channel. Figure 5.6 shows the instantaneous temperature distribution overlapped with the flow streamlines for $P = 600$ and $P = 2000$ in both small and large amplitude channels at equally spaced times throughout a single flow oscillation period. It can be seen in these snapshots that oscillations in the flow lead to large oscillations in the location of the hot fluid core, decreased distances between the

core and the walls, and heated fluid being convected into the troughs of the channel. These characteristics act to significantly enhance heat transfer.

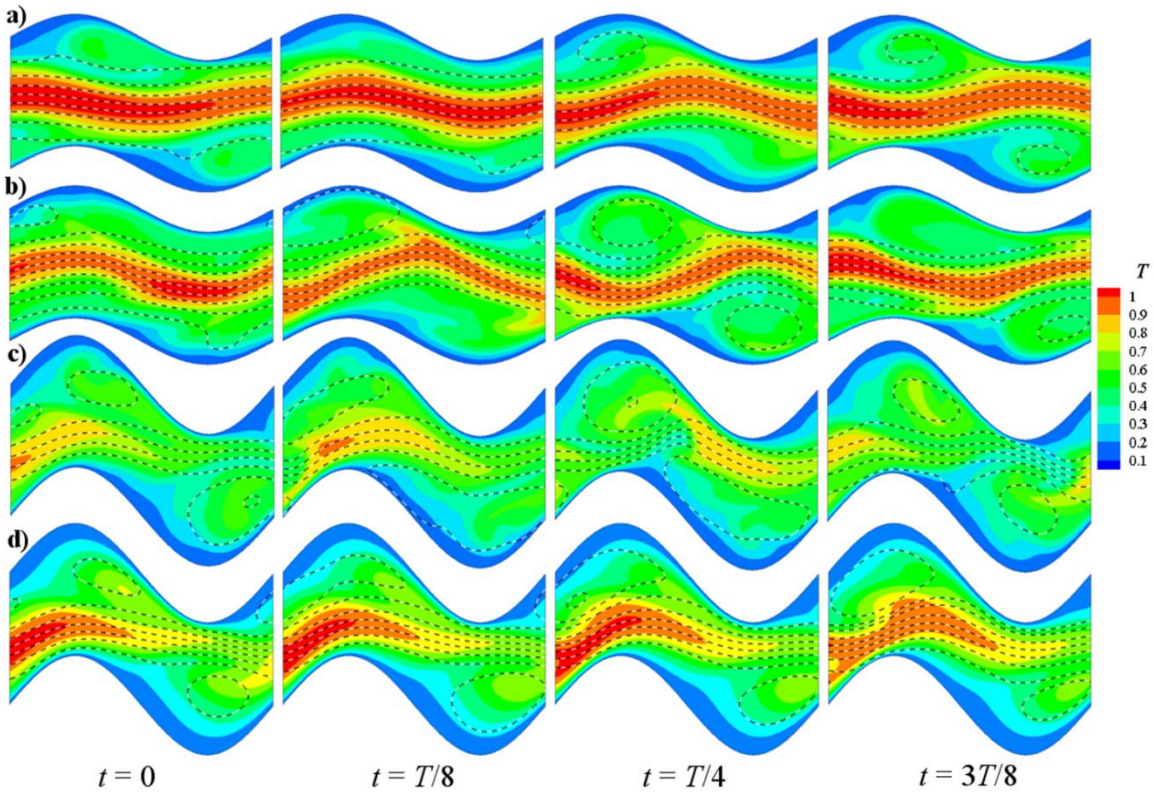

Figure 5.6 – Instantaneous temperature distributions and streamlines for unsteady flows in small and large amplitude channels. Columns correspond to time intervals equally spaced across half of the period of oscillation in the flow. The rows correspond to (a) A = 0.35, L = 4, P = 600, (b) A = 0.35, L = 4, P = 2000, (c) A = 0.75, L = 4, P = 600 and (d) A = 0.75, L = 4, P = 2000.

Because the larger amplitude walls increase flow resistance, the flowrates for $A = 0.75$ shown in Figure 5.6 (c) and (d) are considerably lower than that of $A = 0.35$ shown in Figure 5.6 (a) and (b) for the same P. As a result, for larger A the fluid remains in contact with the cooled walls for a longer period of time allowing for more heat to be removed, which is indicated by the larger area of cool colors (green, yellow and blue) in the contour plots of Figure 5.6 (c) and (d). This comes at the cost of a decrease in the

throughput of an individual channel and although the temperature of the fluid is more significantly reduced, does not necessarily lead to a greater Nu_m.

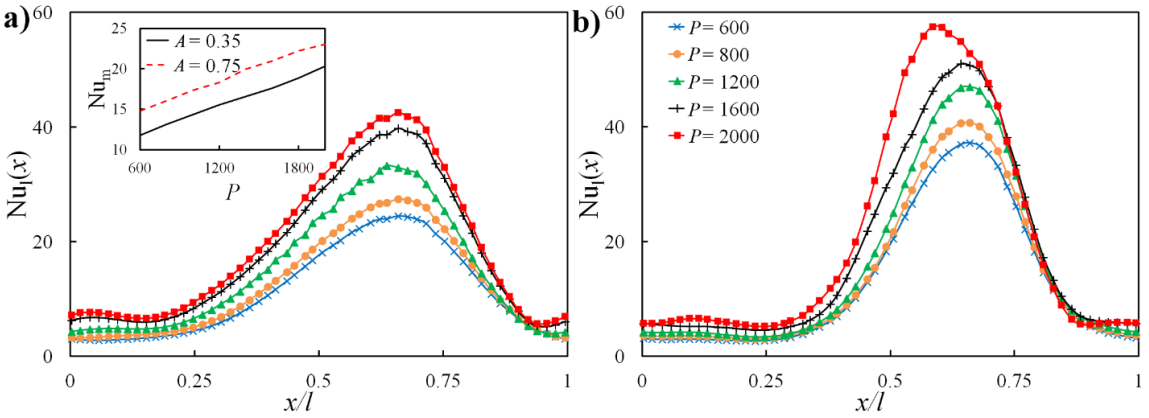

Figure 5.7 – Local Nusselt number Nu_l along top wall of single wall oscillation period for varying values of *P* in the unsteady flow regime. Channel geometries kept constant at (a) *A* = 0.35, *L* = 4 and (b) *A* = 0.75, *L* = 4. Inset of the left plot contains Nu_m corresponding to each line in main plots.

Figure 5.7 (a) and (b) presents plots showing the period averaged values of Nu_l along the top wall at different *P* values for $A = 0.35$ and $A = 0.75$, respectively. It can be seen in these plots that as *P* increases, the maximum values of Nu_l increase as well, going from ~24 (~37) at $P = 600$ to ~42 (~57) at $P = 2000$ for $A = 0.35$ ($A = 0.75$). The increase at the peak value is coupled with slight increases in Nu_l along the entire channel. This is in contrast to the distribution of Nu_l seen in the steady regimes where the increases in the maximum values around $x/l \approx 0.67$ are offset by the decreasing values around $x/l \approx 0.33$ as *P* increases. This difference in the shape of the Nu_l distribution for steady and unsteady flows is the result of the unsteady motion of the vortices in the channel that is a characteristic of the unsteady flow regime. As discussed above, the stationary vortices developing in the circulatory regime act as a thermal barrier by preventing convective

transport of heat from hot fluid stream traveling in the center of the channel into the channel furrows. Conversely, in the unsteady regime the vortices in the furrows are no longer stationary and their motion facilitates convective transport of heat into the furrows. This removes the barrier-like behavior of the vortices, allowing for more heat transfer to occur along the furrow wall and reducing the dip in Nu_l along the wall of the channel furrow. It also allows for the increased flow rates associated with larger values of P to result in an increase in Nu_l along the furrow. With the increases in Nu_l near $x/l \approx 0.67$ no longer counterbalanced by decreases around $x/l \approx 0.33$ as P increases, Nu_m increases from ~12 to ~20 for $A = 0.35$ (~14 to ~22 for $A = 0.75$) as P is varied from 600 to 2000 (inset of Figure 5.7 (a)). This indicates that in the unsteady regime the heat transfer rate depends on P. Furthermore, the nearly identical slope of the lines shown in the inset suggests a reduction in the dependence of the heat transfer rate on A.

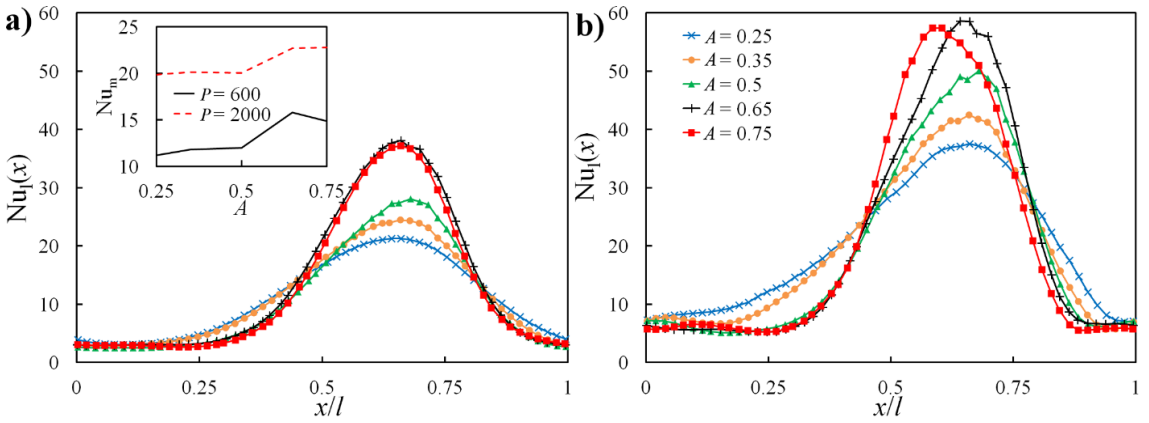

Figure 5.8 – Local Nusselt number Nu_l along top wall of single wall oscillation period for varying values of A in the unsteady flow regime with L = 4. P kept constant at (a) P = 600 and (b) P = 2000. Inset of the left plot contains Nu_m corresponding to each line in main plots.

To investigate the effect of the amplitude on the heat transfer rate in unsteady flows, we plotted Nu_l for varying amplitudes with $P = 600$ and $P = 2000$ in Figure 5.8 (a) and (b), respectively. In both plots there is a significant difference in the shape of the Nu_l curve between smaller amplitudes ($A = 0.25$ and 0.35) and for larger amplitudes ($A = 0.65$ and 0.75). The differences in the shapes of Nu_l are a result of the different flow structures developing in the large and small amplitude channels. For small *A* (see Figure 5.6 (a) and (b)), a vortex sheds from the trough of the upper wall, grows as it travels along the furrow before being ejected. The shedding and subsequent ejection of the vortices creates large oscillations in the location of the heated core, which results in it coming in close proximity with a larger portion of the wall. This increases the length of the wall interaction with hotter fluid leads to the wider peak of Nu_l, but at the same time lowers the magnitudes of the period averaged values of Nu_l.

When *A* is large, two types of vortices develop. There are vortices that remain trapped in the channel furrow whereas other shed vortices travel closer to the channel centerline causing the trapped vortex to undergo periodic oscillations and deformation. As a result, the hot fluid core does not undergo significant variations in its location (see Figure 5.6 (c) and (d)) and subsequently narrows the section of wall in which it comes near. Because the hot fluid approaches a smaller section around the trough of the top wall, Nu_l has a tall narrow peak when averaged over time.

This large amplitude unsteady regime is similar the steady circulatory regime which is also characterized by vortices trapped in the furrows. However, the motion of the trapped vortex in the unsteady regimes allows it to bring heated fluid from the flow core towards

the wall and resulting in a flat Nu_l rather than the dip seen in the steady regime. The mean Nusselt number, Nu_m, is plotted in the inset of Figure 5.8 (a) as a function of *A* for $P = 600$ and $P = 2000$. Again it follows from this plot that when the flow transitions to unsteady, Nu_m begins to show a stronger dependence on *P* rather than *A*, as found in the steady regimes.

5.3.3 Heat Transfer Enhancement

Figure 5.9 contains plots of the mean Nusselt number as a function of *P* for several amplitudes with periods fixed to *L* = 3, 4, and 5. These plots show a strong dependence of Nu_m on *A* and weak dependence on *P* for steady flows. When the flow transitions to unsteady, Nu_m increases rapidly with increasing *P*, whereas the dependence on both *A* and *L* remains similar to that at the steady regime. Because of this and the fact that large amplitudes induce greater increases in Nu_m while in the steady regime, these amplitudes maintain slightly greater values of Nu_m than smaller amplitudes in the unsteady regime. This relationship is complicated by the fact that the values of *P* at which the flow transitions to unsteady depend on both *A* and *L*. However, as shown in the inset of Figure 5.9 (a), the largest values of Nu_m are obtained by larger amplitude channels throughout the range of *P* investigated. Based on Nu_m, the optimum heat transfer is achieved by $A = 0.75,\ L = 3$ for $P < 500$ and $P > 1200$ and by $A = 0.65,\ L = 3$ for $500 < P < 1200$.

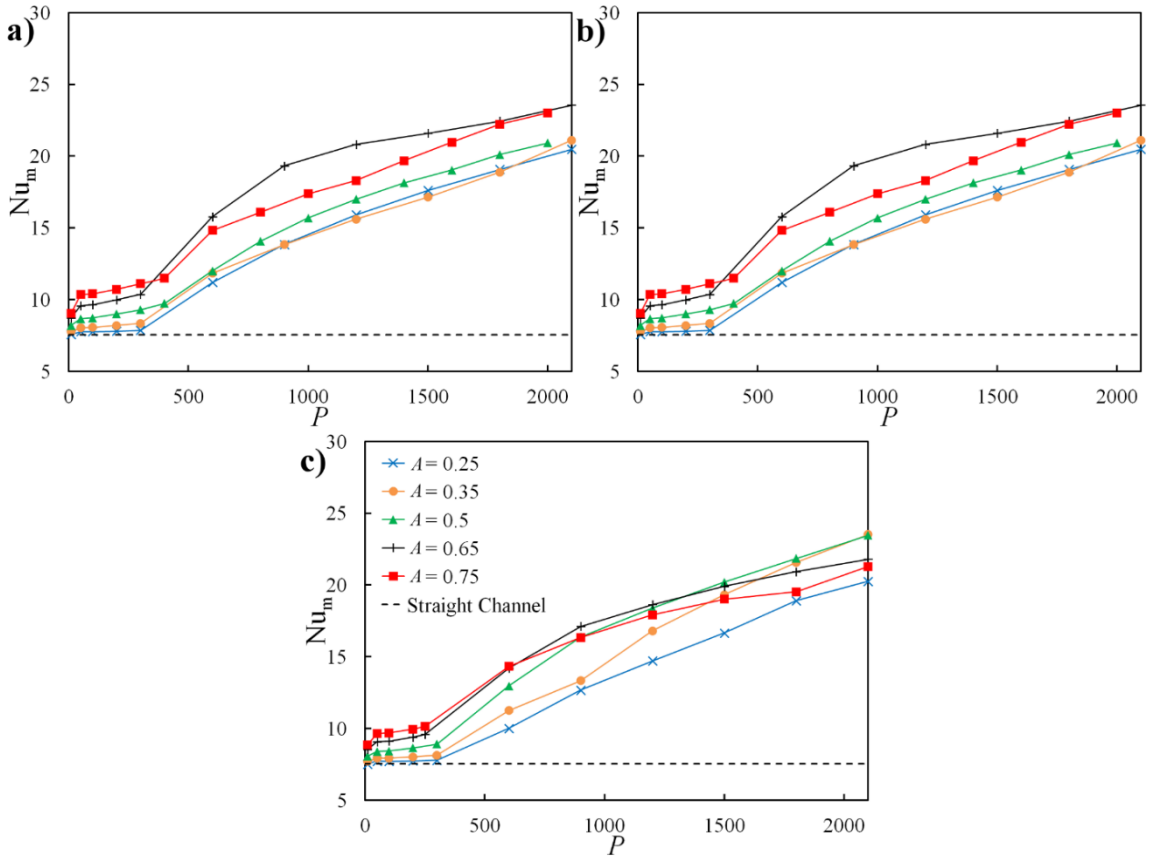

Figure 5.9 – Mean Nusselt number across channel period for *P* ranging from 10 to 2100. Each plot contains several amplitudes with (a) *L* = 3, (b) *L* = 4 and (c) *L* = 5. The dashed line in each plot represents that of a straight channel (Nu_m = 7.54). Inset of the top left plot displays the geometries providing the greatest values of Nu_m for the range of *P* investigated.

As with other passive methods for heat transfer enhancement utilizing complex geometries, the improvement in heat transfer comes at the cost of increased frictional losses.[143] As discussed previously (Section 4.4.5) the walls in an asymmetric wavy channel can induce significant frictional losses, with the magnitudes heavily dependent on both *A* and *P*. Thus, even though the use of Nu_m allows us to isolate the flow regimes with increased heat transfer, this parameter fails to describe the overall performance of the system.

In order to quantify the overall thermal performance of the wavy channels, we chose to use the thermal–hydraulic performance factor given by:[50]

$$\eta = \frac{\mathrm{Nu}_m / \mathrm{Nu}_0}{\left(f / f_0 \right)^{1/3}} . \qquad 5.1$$

Here, $\mathrm{Nu}_0 = 7.54$ and $f_0 = 6/P$ are the mean Nusselt number and friction factor for a straight channel.[124, 144] This parameter indicates the ratio between the increases of heat transfer and friction factor normalized by their respective values for a straight channel.

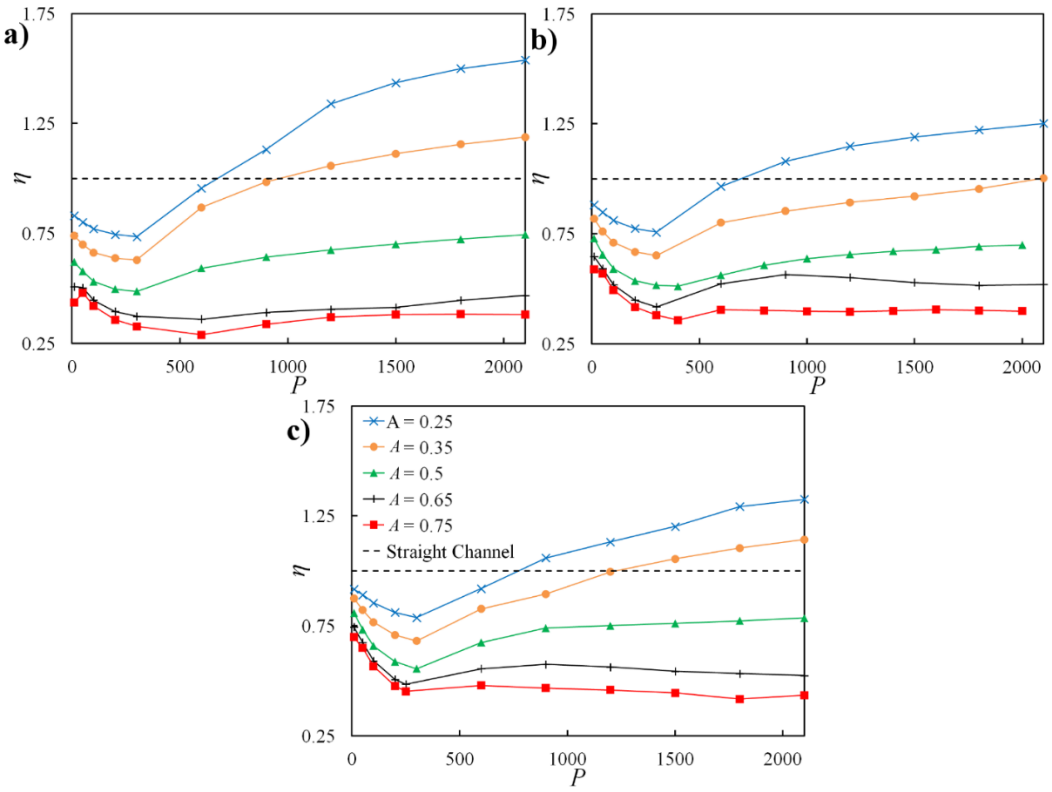

Figure 5.10 – Thermal–hydraulic performance factor for *P* ranging from 10 to 2100. Each plot contains range of amplitudes with (a) *L* = 3, (b) *L* = 4 and (c) *L* = 5. The dashed line represents *η* for a straight channel.

Figure 5.10 shows η plotted against P for the same ranges of A and L as in Figure 5.9. As with the plots of Nu_m, η increases as P increases. Unlike Nu_m, however, η shows strong dependence on A and weak dependence on L, with the smallest amplitudes and periods having the highest values of η. The strong dependence on A is due to Nu_m being independent of A while f is strongly dependent on it. Therefore, as A is increased, f increases while Nu_m remains nearly constant leading to a decrease in η. Interestingly, even in the steady regime where Nu_m is strongly enhanced with larger A, the increased friction factors generated in these large amplitude channels leads to overall lower values of η. These plots also indicate that even though the wavy walled channels act to enhance heat transfer, the increased friction factors associated with the geometry can lead to a thermal–hydraulic performance lower than that of straight channels. This is especially relevant for small pressure drops where the channel has yet to achieve significant increases in Nu_m associated with the unsteady flow regime, and for large A where the large amplitude of the channel walls induces substantial frictional losses. From Figure 5.10 we conclude that small amplitudes and short periods achieve the largest values of η for wavy walled channels and that these channels will exhibit enhanced performance compared to straight channels provided that P is sufficiently large.

Lastly, because the throughput is oftentimes an important design parameter, in Figure 5.11 we plotted η against Re rather than P to allow for comparison across different flow rates. Due to the increased losses associated with wavy walled channels, the Reynolds numbers for different amplitudes have significantly different ranges for the same range of P values. As a result, for $A = 0.75$ Re remains less than 200 for each L investigated. As

with the plots in Figure 5.10, the plots of η vs Re indicate that smaller amplitudes and shorter periods provide the largest increases in thermal performance. Unlike the plots in Figure 5.10, however, the dependence on A is not monotonic and $A = 0.35$ produces the largest value of η for a portion of the Re values investigated. This is due to the higher frictional losses of $A = 0.35$ causing its line to shift further to the left than that of $A = 0.25$ when η is plotted as a function of Re. As a result, the increase in g seen in the unsteady regime occurs earlier, allowing $A = 0.35$ to generate the larger η for certain Re.

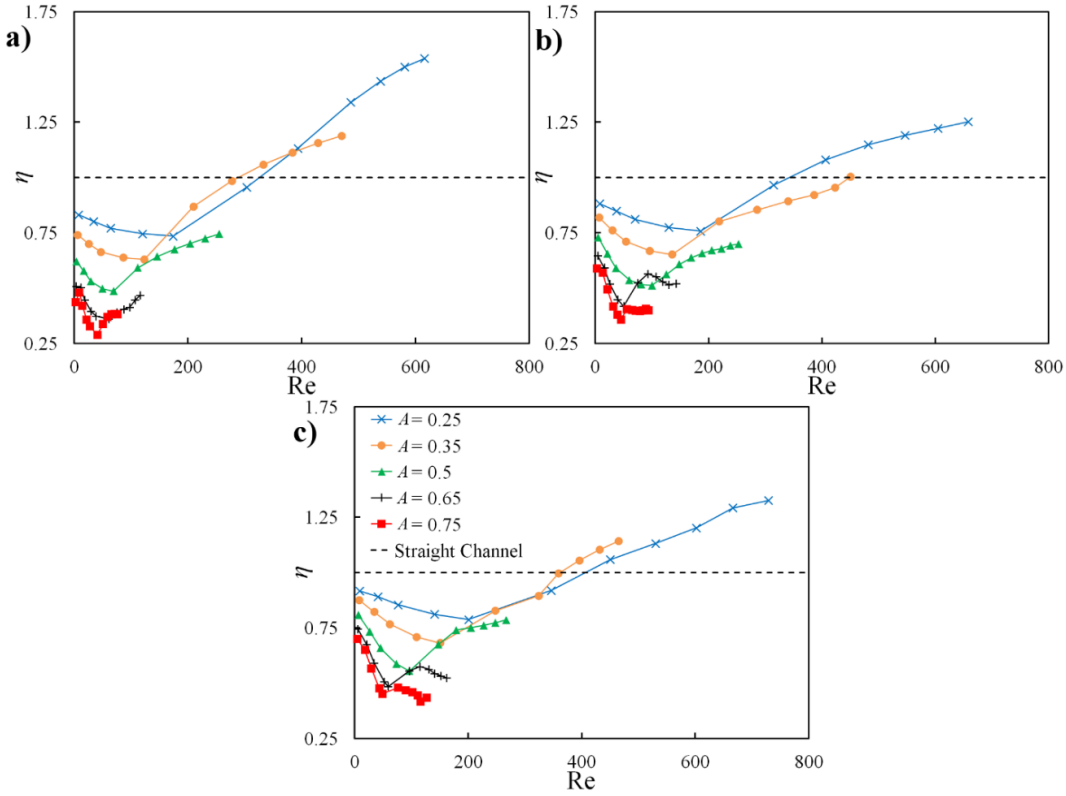

Figure 5.11 – Thermal–hydraulic performance factor plotted as a function of the Reynolds number. Each plot contains range of amplitudes with (a) L = 3, (b) L = 4 and (c) L = 5. The dashed line represents η for a straight channel.

We therefore summarize our simulation results as follows. For small $\mathrm{Re} < 280$, the friction penalty of the wavy channel results in a straight channel being the optimum

geometry. For $280 < \mathrm{Re} < 385$, the combination of $A = 0.35$ and $L = 3$ has the largest η values and for $\mathrm{Re} > 385$ the optimum geometry becomes $A = 0.35$ and $L = 3$. This indicates that small amplitudes provide the greatest thermal–hydraulic performances provided that the flow is laminar and sufficiently far into the unsteady regime.

5.4 Summary

At low pressure drops, when the flow remains in the unidirectional and circulatory regimes, the values of Nu_l along the upper wall experience large increases near the trough of the top wall (around $x/l = 0.67$). These increases are accompanied by decreasing values along the furrow. In these regimes, the maximum Nu_l increases with increasing P, but these increases are offset by decreasing Nu_l along the furrows. As a result, the average Nusselt number along the entire channel, Nu_m, remains nearly independent of P. The mean Nusselt number Nu_m, on the other hand, does exhibit dependence on A, and increases with increasing A. This resembles the results obtained by Wang and Chen who found that the heat transfer enhancement in converging-diverging channels increases with increasing amplitude when the flow is steady.[145]

When the flow transitions to unsteady regime, Nu_l increases along the troughs of the top wall as P increases. In contrast to the steady regime, however, Nu_l also increases along the furrows of the top wall. This is because the motion of the vortices in the unsteady regime enables the transport of hot fluid from the center of the flow to the cold walls along the furrows. Thus, instead of acting as a barrier between the wall and the hot core as in the steady flow regime, unsteady vortices facilitate heat transfer to the channel wall. The

increases in Nu_l along the entire length of the channel as P increases leads to an increase of the overall heat transfer rate across the channel. As a result, Nu_m exhibits a strong dependence on P and is relatively independent of A.

Although wavy walled geometries provide significant enhancements in the heat transfer occurring in the channel, these enhancements are accompanied by considerable increases in frictional losses. When the flow is steady, the high friction factor outweighs the increases in the heat transfer rate, leading to thermal-hydraulic performance factors lower than that of a straight channel. For larger pressure gradients (greater than the critical P associated with the transition to the unsteady regime), the thermal-hydraulic performance of small amplitude channels is greater than that of a straight channel. For large amplitude channels, however, the performance remains worse than that of straight channels for all P.

Based on the low magnitude of the thermal-hydraulic performance factor of wavy walled channels at low values of P, we can conclude that this geometry is not well suited for use in heat transfer applications with low flow rates ($\mathrm{Re} < 300$). At larger flow rates, however, the thermal-hydraulic performance of wavy walled channels shows a significant increase for smaller amplitudes, achieving greater than 50% improvement over a straight channel for the range of parameters investigated. This indicates that small amplitude wavy walled channels are preferable for use in applications such as heat exchangers provided that the flow rate is large enough for the flow to be unsteady.

CHAPTER 6. FOULING LAYER DEVELOPMENT

6.1 Introduction

The fouling of heat exchangers poses a significant problem across a wide range of industries. This is particularly true for the coolers found in exhaust gas recirculation systems used in gasoline in diesel engines. In these heat exchangers, the deposition of soot particles entrained in the exhaust gas form an extremely porous fouling layer. Because of its high porosity the layer acts to insulate the cold walls from the hot fluid, decreasing the effectiveness of the cooler. With high concentrations of soot particles found in the exhaust generated during the combustion process, this fouling process occurs rapidly leading to significant losses in the performance of the system.

In an attempt to extend the life span of EGR heat exchangers, engine manufacturers have begun utilizing wavy walled channels. This is because empirical evidence suggests that the wavy geometry provides better resistance to fouling than other traditional cooler types such as shell and tube. Despite this increased interest, a full understanding of how the fouling layer develops in these channels does not exist. Furthermore, significant discrepancies have been found between experimental results and those obtained from numerical simulations.

Using simulations, we probe the early development of the fouling layer from the deposition of particles entrained in a laminar flow through an asymmetric wavy walled channel. Specifically, we examine the physics driving the fouling layer formation to develop a clear understanding of how the geometry influences its growth and the

subsequent effects of this growth on the fluid flow and heat transfer occurring in the channel. Furthermore, we systematically vary the geometric parameters of the channel, A and L, along with the pressure gradient driving the flow in order to investigate their effects on the layer development. Using a computational model capable of capturing the effects of the growing fouling layer on the flow and heat transfer Results from these investigations provide vital insights into the fouling of wavy walled heat exchangers necessary for designing more fouling resistant coolers.

6.2 Computational Setup

Please refer to Section 2.6.4 for a detailed discussion of simulation parameters used in this investigation.

6.3 Results and Discussion

As particles entrained in the flow travel along the channel, a thermophoretic force induced by temperature gradients in the fluid results in their migration toward and subsequent deposition along the cooler walls. These deposited particles accumulate to form a layer of soot, which grows as particles continue to deposit. This growth is influenced by complex interactions between the effects of the fluid (i.e. advective transport and shear removal), and temperature distribution on the particle transport and deposition. Furthermore, as the layer grows, its effect on the flow and heat transfer influences subsequent development of the fouling layer. In the following discussion, we first examine the physical mechanisms driving the formation of the layer and the effects of this layer on the fluid flow, heat transfer and continued deposition along the walls. This is followed by

a systematic investigation of the dependence of the layer formation on the parameters A, P and L.

6.3.1 Physics of Fouling Layer Formation

Snapshots taken at equally spaced intervals of the total simulation time, T_{total}, showing the development of the fouling layer along one wall period of a channel with $A = 0.5$, $L = 4$ and $P = 2000$ are provided in Figure 6.1. In this figure, the position of the layer is obtained from the average position of the first three wall periods of the channel. Here we see as time progresses, the fouling layer forms across the entire length of the period. The rate at which this occurs varies spatially, resulting in a non-uniform thickness of the layer with the thickest and thinnest sections located on the front and back of the wall peaks, respectively.

In order to understand the mechanisms driving this formation, we first examine the fouling layer along the top wall at $t = T_{total}/4$, the thickness of which is provided in Figure 6.2 (a). Here, the thickness, t_{fl}, is defined as the distance, normalized by h, from the wall to surface of the fouling layer in the direction normal to the wall. In this plot we see that early in the formation of the layer, three areas of increased thickness develop along the wall, which together cover approximately half its length, from $x/l \approx 0.1$ to $x/l \approx 0.6$. In the following discussion, we will refer to these peak-like formations in the layer as dunes to avoid confusion as we have previously defined peaks to refer to a section of the wall. The largest of these dunes covers the entire front side of the wall peak (defined as $x/l \in [0.25, 0.5]$). The second tallest dune covers a portion of the backside, while the

smallest dune is positioned along a section of the furrow. Along the remaining section of the wall, the fouling layer maintains a nearly uniform thickness.

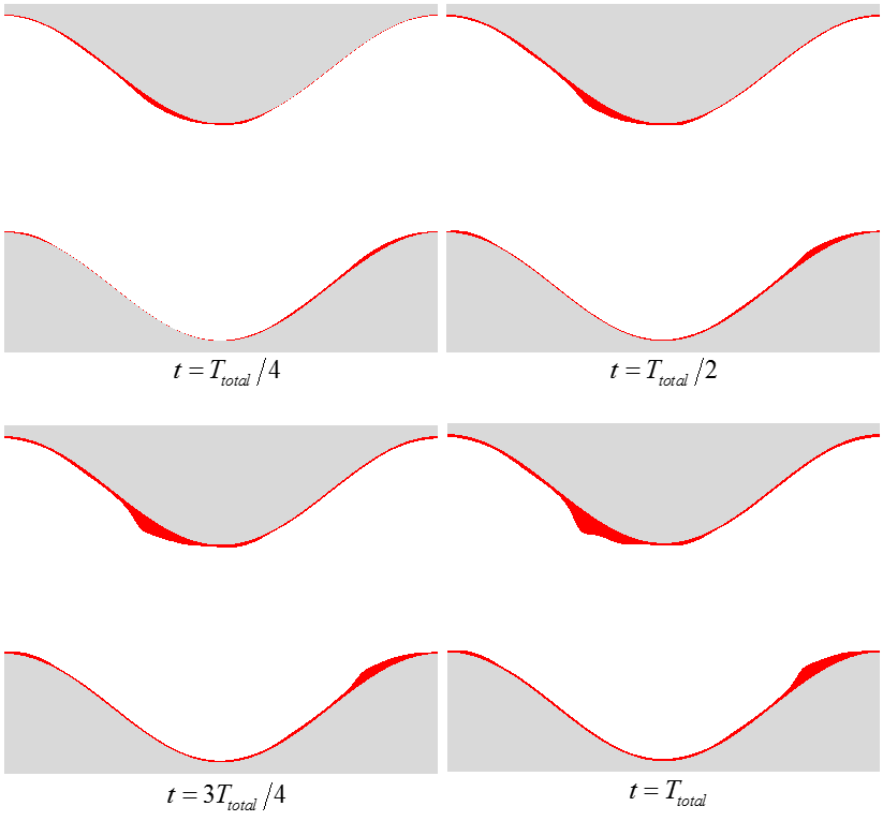

Figure 6.1 – Fouling layer formation along single wall period near inlet of channel with A = 0.5, L = 4 and P = 2500.

The increased thickness of the fouling layer forming these dunes is a result a larger rate of particle deposition along this section of the wall. This larger deposition rate is due to the increased thermal gradients at this location, which induce larger thermophoretic particle velocities acting in the direction of the wall. Because of the following relationship between the thermophoretic velocity, V_t and the local temperature, T :

$$V_t \propto \frac{dT}{dn}\frac{1}{T}, \qquad 6.1$$

the local Nusselt number along the wall, which is given by:

$$\mathrm{Nu}_{\mathrm{l}}\left(x\right)=\frac{4a}{T_s-T_{m,x}}\left(\frac{\partial T}{\partial n}\right), \tag{6.2}$$

serves as an accurate representation of the distribution of thermophoretic velocities near the wall (the bulk mean temperature of the fluid only decreases slightly across the length of the period). The distribution of the local Nu, representing the thermophoretic velocities near the wall, can be seen in the plot provided in Figure 6.2 (b), which contains the local Nusselt number, Nu_l, across the length of the top wall of the channel period. In this figure, we provide Nu_l at $t=0$ to show the thermophoretic velocity distribution leading to the formation of the layer obtained at $t=T_{total}/4$ shown in Figure 6.2 (a). Furthermore, to provide a more accurate representation of Nu_l which exhibits time-periodic oscillations from the unsteady flow, the values of Nu_l are obtained from an average of fifty samples taken at intervals of $T_{total}/2000$. Here we can see that, initially as layer begins to form, the distribution of Nu_l contains a single peak, which covers the same location along the channel wall as the fouling layer dunes. Furthermore, the center of the peak corresponds to the location of the thickest deposit. Additionally, the remaining length of the channel, where the thickness of the layer is constant, contains nearly uniform values of Nu_l.

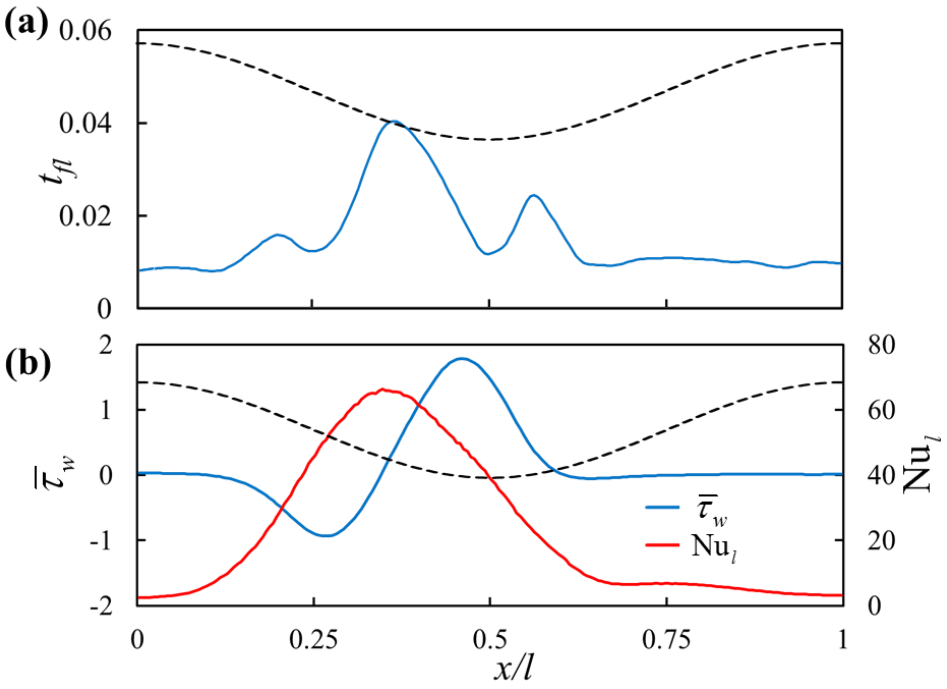

Figure 6.2 – Plots showing the (a) thickness of the fouling layer at $t = T_{total}/4$, and (b) the local Nusselt number and wall shear stress at $t = 0$ along the top wall of a single channel period. Values obtained from a period near the inlet of a channel with $A = 0.5$, $L = 4$ and $P = 2000$. Short dashed black line indicate position of the upper wall at each value of x/l (not to scale).

While the larger growth rates at the location of the dunes is due to the increased thermal gradients there, the formation of three dunes rather than one is a result of the wall shear stress induced by the flow. A plot of the normalized wall shear stress, $\bar{\tau}_w$, along the upper wall of the channel at $t = 0$ is provided in Figure 6.2 (b) along with Nu_l. Here, like Nu_l, the distribution of $\bar{\tau}_w$ is obtained from time averaged values. As discussed previously, the normalization for the shear stress is chosen such that for a straight channel, $\bar{\tau}_w = 1$, while negative values indicate shear acting in the $-x$ direction. In this figure, we see that the shear stress has two maxima (in terms of absolute value) with each acting in opposing directions.

The left maximum, located in the valley between the left and center dunes at $x/l \approx 0.25$, has a value of $\overline{\tau}_w = -0.93$ indicating that it acts in the upstream direction. As particles with diameters of $d_p \geq 210$ nm, which have a normalized critical shear stress of $\overline{\tau}_{cr} \leq 0.82$, deposit at this location along the wall, they are immediately removed from the surface by the large shear stress depositing further upstream along the wall. This continues as the particle travels along the wall in the $-x$ direction until it reaches a location with sufficiently low shear stress, resulting in a decreased rate of deposition at this section of the channel and the formation of the valley between the two dunes.

Although all particles sheared from the wall at the location of the valley eventually deposit at the location of the left dune, the size of this dune is significantly smaller than that of the center one. This is due to two causes, one being that the largest thermophoretic particle velocities and therefore the highest deposition rates are located along the section of the wall covered by the center dune. The second cause is that the vortices in the channel furrow act as a barrier, keeping the bulk flow along the center of the channel from reaching the section covered by the left dune. This can be seen in Figure 6.3 which contains the streamlines along a single wall period near the inlet of the channel at $t = 0$. Similar to the plots of $\overline{\tau}_w$ and Nu_l, the streamlines are calculated from the velocity field which is averaged from 15 samples spaced $T_{total}/500$ apart. In this figure we see that a stagnation point exists on the front side of the wall peak where the flow traveling along the center of the channel, which we refer to as the bulk flow, reattaches to the wall and continues traveling downstream. The majority of the particles are contained in this bulk flow, while only a small portion of the particles enter into the furrow through either the limited

convection into the furrow caused by the motion of the vortices, or thermophoresis. It is this small portion of particles that is able to deposit at the location of the left dune, while a significantly larger amount are able to deposit along the section of the wall peak where the bulk flow has reattached. Along the backside of the wall peak, the location where the bulk flow detaches ($x/l \approx 0.6$) coincides with the thickness of the fouling layer leveling off. As with the reduction in the thickness of the left dune, this is due to the reduced concentration of particles in the fluid filling the furrows compared with that of the bulk flow.

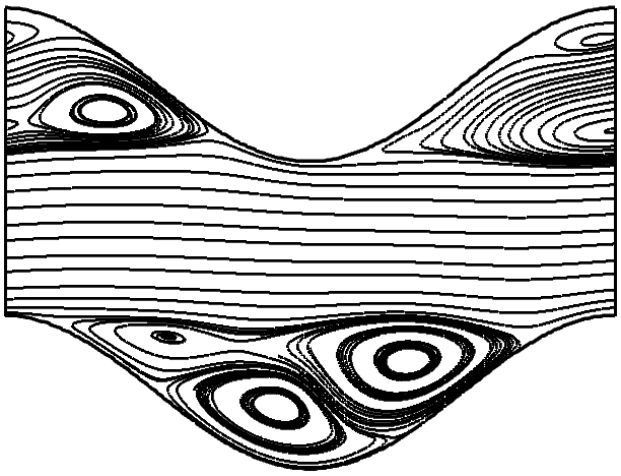

Figure 6.3 – Streamlines from the time averaged velocity field in a single wall period near the inlet of a channel with $A = 0.5$, $L = 4$, and $P = 2000$.

Similar to the left maximum of $\bar{\tau}_w$ at $t = 0$ shown in Figure 6.2 (b), the maximum on the right, located in the valley between the center and right dunes at $x/l \approx 0.5$, has a value of $\bar{\tau}_w = 1.8$. Because the magnitude of the shear stress here is nearly twice that of the left maximum, the largest diameter of particles capable of remaining attached to the wall is reduced from 190 nm to 150 nm. Despite this reduction, the thickness of the fouling layer is comparable to the thickness of the left valley due to the high concentration bulk flow traversing this section of the wall (as seen in Figure 6.3). As with the left valley, larger

diameter particles that deposit in the location of the right valley undergo successive deposition and removal until reaching an area of sufficiently low shear stress. During this process, the particle travels along the wall in the $+x$ direction resulting in the formation of the right dune, which, due to the increased particle flux, is approximately 60% taller than the dune on the left.

Positioned between the two maxima in $\bar{\tau}_w$ is the center dune, which is the tallest of the three. The topmost point of this dune is located at $x/l \approx 0.35$ which corresponds with both the largest thermophoretic velocities as well as the stagnation point where $\bar{\tau}_w = 0$. Furthermore, as this is where the particle laden bulk flow reattaches to the wall (see Figure 6.3), the fluid contains the highest concentration of particles at this location, which decreases as particles entrained in the fluid deposit as the flow travels along the length of the wall peak before detaching. The combination of these three effects leads to this location having the largest fouling layer growth rate, which results in this dune containing over 40% of the total area of the layer along the top wall of the channel period. The remaining section of the channel wall not covered by the dunes experiences a negligible shear stress. However, a minimal amount of particles deposit at this location due to the lower thermophoretic velocities and lower concentration of particles in the surrounding fluid. This lower concentration is due both the effect of the vortices as discussed previously as well as the large deposition rate near the wall peak reducing the number of particles available to deposit, resulting in this section experiencing the lowest rate of growth.

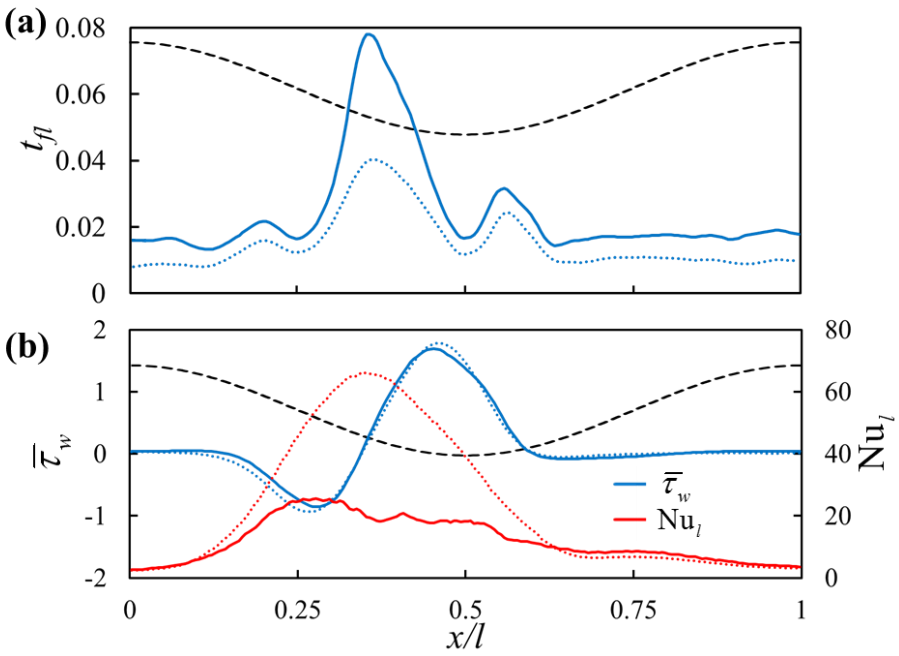

Figure 6.4 – Plots showing the (a) thickness of the fouling layer at $t = T_{total}/4$ (dotted line) and $t = T_{total}/2$ (solid line), and (b) the local Nusselt number and wall shear stress at $t = 0$ (dotted lines) and $t = T_{total}/4$ (solid lines) along the top wall of a single channel period. Values obtained from a period near the inlet of a channel with A = 0.5, L = 4 and P = 2000. Short dashed black line indicate position of the upper wall at each value of x/l (not to scale).

The fouling layer thickness continues to increase as additional particles deposit along the walls of the channel. This can be seen in Figure 6.4 (a), which contains a plot of the layer thickness along the top wall at $t = T_{total}/2$. In this figure we have included the previous thickness at $t = T_{total}/4$ for comparison. Here, we see that between $t = T_{total}/4$ and $t = T_{total}/2$, the thickness of the fouling layer along the center dune increased significantly compared to that of the remaining dunes. Specifically, during this time-span the average change in the normalized thickness is 0.0051, 0.018 and 0.0064 for the left, center and right dunes, respectively. When compared with the growth of the layer from $t = 0$ to $t = T_{total}/4$, we find that these changes in thickness represent decreases of 62% (left), 31% (center)

and 64% (right) in the growth rates. Furthermore, the average thickness of the remaining length of the wall increased by 0.0070 (a reduction of 27%), which is slightly higher than that of the two smaller dunes, indicating a change in the conditions that previously led to their formation.

The thermal resistance of the fouling layer is proportional to the layer thickness. Therefore, as the fouling layer grows, its effect on the distribution of thermophoretic velocities near the surface does as well. This can be seen in Figure 6.4 (b), which contains a plot of Nu_l across the surface of the fouling layer at $t = T_{total}/4$ (solid red line) along with the initial distribution across the wall at $t = 0$ (dotted red line). Here we see that the insulating effect of the fouling layer causes the local Nusselt number along the section of the dunes to reduce from its peak-like shape with a maximum value of 65.9 at $x/l = 0.35$ to a nearly plateau-like shape with a maximum of 25.6 at $x/l = 0.28$. This indicates a significant reduction in the thermophoretic velocities of the particles near this portion of the wall, resulting in the reduction of the fouling layer growth rate.

To understand how the distribution of Nu_l is altered by the formation of the fouling layer, it is necessary to examine how the layer influences the distribution of its constituent terms. The distribution of the surface temperature, θ_s, the bulk mean temperature, θ_m, the temperature gradient, $d\theta/d\bar{n}$, and Nu_l along the top wall are provided in Figure 6.5. Here, $\theta = (T - T_w)/(T_{in} - T_w)$ represents the normalized temperature and $d\theta/d\bar{n}$ is the temperature gradient normalized according to:

$$d\theta/d\bar{n} = \left[\frac{(dT/dn) - T_w}{T_{in} - T_w} \right] h . \qquad 6.3$$

At $t = 0$ (Figure 6.5 (a)), before a fouling layer has formed, the surface temperature is equivalent to the wall temperature. Furthermore, the bulk mean temperature of the fluid decreases monotonically from $\theta_m = 0.77$ to $\theta_m = 0.71$ across the length of the period. This results in the nearly identical shapes of Nu_l and $d\theta/d\bar{n}$, which contain a single peak. The maximum values of $d\theta/d\bar{n}$ and Nu_l coincide with the reattachment point of the bulk flow, which contains the highest fluid temperatures and, therefore, the largest thermal gradients.

At $t = T_{total}/4$, the formation of the fouling layer along the wall leads to the complex distribution of Nu_l caused by the layer's effect on the surface temperature and thermal gradient as seen in Figure 6.5 (b). Here, we see that, with the surface no long coinciding with the location of the wall, θ_s possess a shape similar to that of Nu_l at $t = 0$. Furthermore, a local minimum in $d\theta/d\bar{n}$ is found at the location of its previous maximum ($x/l = 0.36$). As discussed above, this location coincides with the reattachment point of the high temperature bulk flow, which induces the largest thermal gradients at $t = 0$ when $\theta_s = 0$. The large thermal gradients, in turn, cause this location to contain the thickest deposit layer at $t = T_{total}/4$ and, as a result, the largest thermal resistance between the surface and the wall. This large thermal resistance acts to insulate the surface from the wall, causing the surface temperature to approach that of the hot bulk flow and $d\theta/d\bar{n}$ to develop a local minimum at this location. With the surface at the reattachment point unable to conduct heat from the fluid to the cooled wall, the fluid maintains its high temperature as

it travels across the surface in opposite directions from this location. As a result, $d\theta/d\bar{n}$ contains a maximum value on both the left and right of the minimum location where the surface temperature is lower due to the thinner layer.

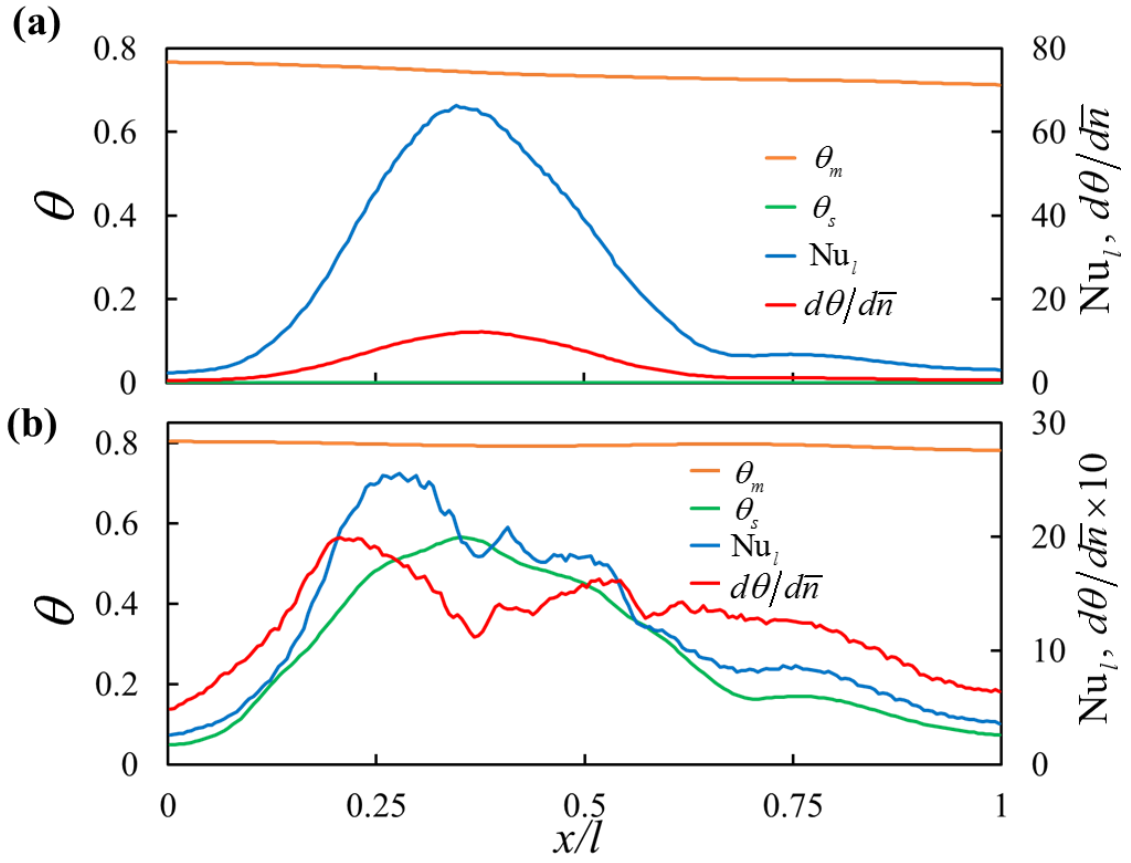

Figure 6.5 – Plots showing the surface temperature, θ_s, the thermal gradient, $d\theta/d\bar{n}$, and the local Nusselt number along the top wall and the bulk mean temperature, θ_m, along the length of the channel period at (a) $t = 0$ and (b) $t = T_{total}/4$. Values obtained from a period near the inlet of a channel with A = 0.5, L = 4 and P = 2000. Note, $d\theta/d\bar{n}$ rescaled by 10 in (b).

On either side of the three dunes, the values of Nu_l at $t = T_{total}/4$ are slightly higher compared to those obtained at $t = 0$. As with the development of the two maxima in $d\theta/d\bar{n}$ discussed above, this is due insulating effects of the fouling layer at the location where the

bulk flow reattaches to the surface. Outside of the dunes, the increase in the temperatures of the fluid near the surface are sufficiently high to induce marginally larger values of Nu_l than those found at $t = 0$. Although the local Nusselt number increases slightly, like the section of the wall covered by the dunes, this portion of the upper wall also experiences a decrease in the growth rate of the fouling layer. The decrease is a result of the insulating effects of the fouling layer causing a decrease in the magnitudes of the thermal gradients within the fluid. This, in turn, reduces the rate at which thermophoresis transports particles from the fluid at the center of the channel, where the concentrations are highest, to the vicinity of the wall where the can deposit along the wall.

Unlike Nu_l, the development of the fouling layer has limited effect on the shear stress along the surface, which we will continue to refer to as the wall shear stress. This can be seen in Figure 6.4 (b), which contains a plot of $\overline{\tau}_w$ across the surface at $t = T_{total}/4$ (solid blue line) along with the initial distribution at $t = 0$ (dotted blue line). Here we see that the formation of the fouling layer causes the left maxima to decrease from $\overline{\tau}_w = -0.93$ ($x/l = 0.26$) to -0.86 ($x/l = 0.28$), while the right maxima decreases from $\overline{\tau}_w = 1.8$ ($x/l = 0.46$) to 1.7 ($x/l = 0.45$). These represent decreases of 7.5% and 5.1%, respectively. The slight decreases in the shear stress is the result of the fouling along the entire length of the channel increasing the friction along the wall, which is evidenced by the friction factor increasing by 5.1% from $f = 0.092$ to 0.097. This increased friction leads to reduced fluid velocities and, subsequently, reduced wall shear stresses. Furthermore, the reduced inertia of the fluid causes the location of the maxima to shift closer to the stagnation point at $x/l \approx 0.34$.

Although the portion of the wall covered by the left and right dunes continues to experience an increased thermal gradient compared to the section of the wall with uniform thickness, it is no longer sufficient to overcome the elevated shear stress. As a result, the increase in the thickness along these two dunes is slightly lower than that of the uniform thickness section. The section covered by the center dune, on the other hand, continues to undergo the largest fouling layer growth rate due to it the negligible shear stress at its center, along with the large thermophoretic velocities, as evidenced by the high values of Nu_l at the surface. Furthermore, the location where the bulk flow reattaches to the surface remains at the center of the dune, resulting in this fluid near this location containing the largest particle concentrations. Because the center dune experiences the majority of the particle deposition, the percent of the total fouling layer area contained in the left, center and right dunes changes from 11%, 43%, and 13% at $t = T_{total}/4$ to 9.8%, 45% and 11% at $t = T_{total}/2$, respectively. The percent of the area found along the remaining length of the wall increases from 31% at $t = T_{total}/4$ to 34% at $t = T_{total}/2$.

As the fouling layer continues to grow, the deposition of particles follows a trend similar to that found at $t = T_{total}/2$. This can be seen in Figure 6.6 (a), which contains a plot of the layer thickness along the top wall at $t = 3T_{total}/4$. Again, we have included the previous thicknesses at $t = T_{total}/4$ (dotted line) and $t = T_{total}/2$ (long dashed line) for comparison. Here, we see that between $t = T_{total}/2$ and $t = 3T_{total}/4$, the center dune continues to experience significantly higher rates of deposition compared with the remaining length of the fouling layer. Specifically, during this time-span the average change in the normalized thickness is 0.017 for the center dune and 0.0045 for the

remaining length of the wall. These increases in the thickness represent decreases of 6.0% and 32% in the growth rates of layer at these two locations compared with the rates observed at $t = T_{total}/2$.

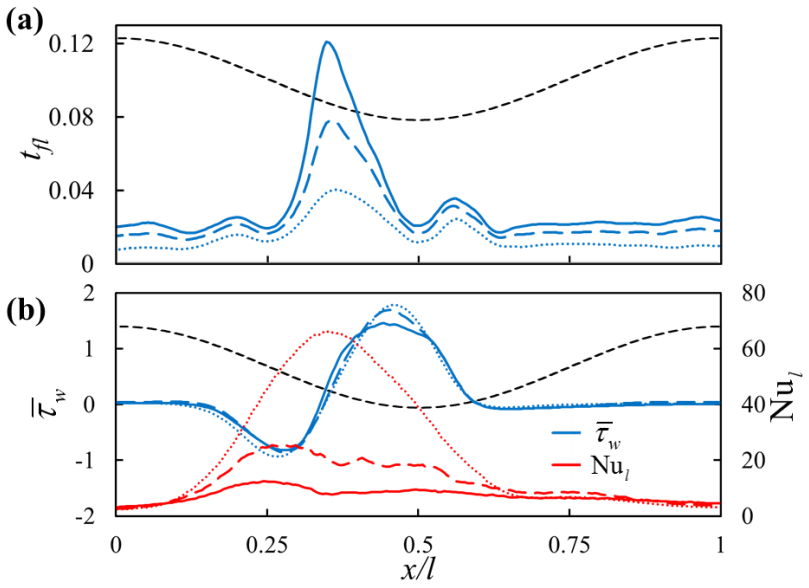

Figure 6.6 – Plots showing the (a) thickness of fouling layer at $t = T_{total}/4$ (dotted line), $t = T_{total}/2$ (long dashed line) and $t = 3T_{total}/4$ (solid line), and (b) Nu_l and $\bar{\tau}_w$ at $t = 0$ (dotted lines), $t = T_{total}/4$ (long dashed lines) and $t = T_{total}/2$ (solid lines) along the top wall of a single channel period. Values obtained from a period near the inlet of a channel with A = 0.5, L = 4 and P = 2000. Short dashed black line indicates position of the upper wall at each value of x/l (not to scale).

As the thermal resistance of the fouling layer continues to increase with its increasing thickness, the thermophoretic velocity of particles near the surface continues to decrease. This can be seen in Figure 6.6 (b), which contains a plot of Nu_l and $\bar{\tau}_w$ across the surface of the fouling layer at $t = 0$, $T_{total}/4$ and $T_{total}/2$. Here we see that the effect of the thicker fouling layer causes further decreases in Nu_l leading to the maximum value of Nu_l reducing from 25.6 at $t = T_{total}/4$ to 12.5 at $t = T_{total}/2$. As with the distribution of Nu_l for

$t = T_{total}/4$, a local minimum in Nu_l exists at the thickest point in the center dune for $t = T_{total}/2$. Furthermore, the local maxima in Nu_l on either side have continued to shift away from this point to the edges of the center dune at $x/l = 0.25$ and $x/l = 0.50$, which correspond to local minima in the fouling layer thickness.

As before, the continued growth of the fouling layer has limited effect on the shape of the wall shear stress distribution as seen in Figure 6.6 (b). Here, we see that $\bar{\tau}_w$ maintains its two regions of elevated shear stress corresponding to the locations of the valleys in the fouling layer. Although $\bar{\tau}_w$ retains a similar shape, the growing fouling layer is beginning to induce noticeable deviations from the initial distribution. Specifically, the change in the magnitude of the two maxima (in terms of absolute value) and the location between the two maxima where $\bar{\tau}_w = 0$. Examining the location of $\bar{\tau}_w = 0$, we find that its slight shift to left corresponds to an identical shift in the peak of the center dune. The slow migration of the center dune peak is the result of the larger values of Nu_l on the left face of the center dune, resulting in a slightly larger growth rate on that side. It is this small difference in the growth rate that causes the peak in the center dune, and subsequently the location of $\bar{\tau}_w = 0$ to undergo a slow shift leftward.

Examining the change in the magnitude of the two maxima, we find that the left and right maxima, respectively, decrease from $\bar{\tau}_w = -0.86$ and $\bar{\tau}_w = 1.7$ at $t = T_{total}/4$ to -0.82 and 1.5 at $t = T_{total}/2$. The 4.5% decrease in the maximum on the right is smaller than the previous decrease between $t = 0$ and $t = T_{total}/4$, while the 14% decrease in the right maximum is larger than before. As with the previous decrease, this is partially due to the

increased friction along the entire length of the channel reducing the fluid velocities. This, however, does not fully account for the 14% reduction seen in the right maximum. The additional decreases in the right maximum are the result of increased depth and reduced width of the valley between the center and right dunes. Because of the changes in its shape, fluid streamlines are unable to remain close to the surface, traveling over the valley rather than along it, causing the additional reduction in the magnitude of the shear stress along this section. Furthermore, the reduced shear stress in this location leads to slightly larger velocities of the fluid, increasing the shear stress on either side of the valley. This reduction in the shear stress does not occur on the left side of the center dune as the additional growth of the fouling layer does not result in the depth of the left valley increasing.

As discussed with the fouling growth at $t = T_{total}/2$, the non-zero shear stresses along the section of the wall covered by the left and right dunes acts to offset the elevated thermophoretic velocities. Because of this, the portion of the wall not covered by dunes experiences an average increase in thickness of 0.0049 while the left and right undergo average increases of 0.0034 and 0.0038 respectively. Furthermore, as the low shear stress and elevated thermophoretic velocities along the center dune, coupled with its location coinciding with the reattachment point of the bulk flow continues to produce the highest growth rates at the section of the wall covered by this dune. This results in the portion of the fouling layer area contained in the center dune to increase from 45% $t = T_{total}/2$ to 48% at $t = 3T_{total}/4$.

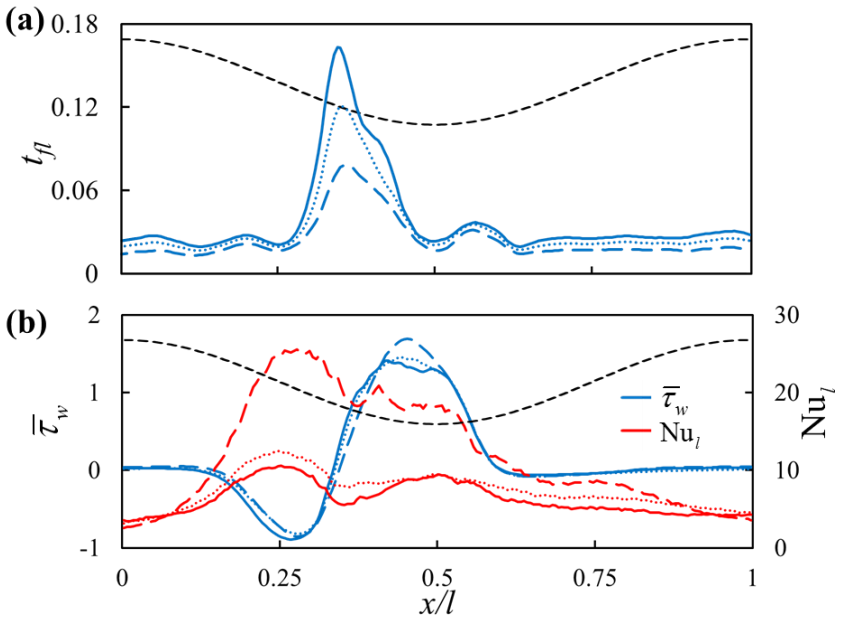

Figure 6.7 – Plots showing the (a) thickness of fouling layer at $t = T_{total}/2$ (long dashed line), $t = 3T_{total}/4$ (dotted line), and $t = T_{total}$ (solid line), and (b) Nu_l and $\overline{\tau}_w$ at $t = T_{total}/4$ (long dashed lines), $t = T_{total}/2$ (dotted lines) and $t = 3T_{total}/4$ (solid lines) along the top wall of a single channel period with A = 0.5, L = 4 and P = 2000. Short dashed black line indicates position of the upper wall at each value of x/l (not to scale).

The continued deposition of particles from $t = 3T_{total}/4$ to $t = T_{total}$ leads to the accentuation of three features in the distribution of the fouling layer, which were previously difficult to distinguish from their surroundings. These include the formation of two dunes located at the ends of the wall and a narrowing of the dune near its maximum value. These can be seen in Figure 6.7 (a) which contains a plot of the layer thickness along the top wall at $t = T_{total}/2$, $3T_{total}/4$ and T_{total}. In this figure, the new dunes on the left and right edges of the wall can be seen along the regions spanning $x/l \in (0, 0.1)$ and $x/l \in (0.9, 1)$, respectively. Along with the accentuation of these features, we can see that the growth of the fouling layer continues to follow a trend similar to that observed at $t = 3T_{total}/4$.

Specifically, the continuing decrease in the average growth rate of the fouling layer. During this time span the surface of the center dune increased by an average of 0.016, while the remaining length of the fouling layer get an average of 0.0042, representing decreases of 6.7% and 22%, respectively.

Although the initial formation of the dunes at the left and right ends of the top wall could be seen at $t = 3T_{total}/4$, these dunes remained smaller than the three which formed early in the development of the layer. This is due the initially high deposition rate in the location of the three initial dunes, reducing the particle concentration inside the furrow. As the fouling layer develops, the deposition rate decreases, increasing the particle concentration in the furrow. With higher concentrations, more particles are able to deposit along the furrow wall to form these new dunes. We will refer to these as the far left and far right dunes, while continuing to use left, center and right to refer to three initial dunes. At $t = T_{total}$, the far left and far right dunes reach a maximum thickness of 0.0279 at $x/l \approx 0.04$ and 0.0317 at $x/l \approx 0.96$, respectively, while the maximum thickness of the left dune is 0.0278.

Early in the development of the fouling layer, the large thermophoretic velocities along the wall peak acted to create a single wide section of increased particle deposition, while two regions of elevated shear stresses etched valleys into the deposits. The combination of these opposing mechanisms led to the formation of three dunes (left, center and right) rather than a single wide one. Furthermore, the peak of the center dune is located at a stagnation point where $\bar{\tau}_w = 0$, while the valleys on either side are positioned at the maximums in the shear stress distribution. The sections of the wall containing the far left

and right dunes, on the other hand, experience negligible shear stress and low thermophoretic velocities in the nearby particles. This can be seen in Figure 6.7 (b), which contains the distribution of Nu_l and $\bar{\tau}_w$ along the upper wall of the channel period at $t = T_{total}/4$, $T_{total}/2$ and $3T_{total}/4$. Furthermore, the valley to the right of the far left dune at $x/l \approx 0.1$ is located at a stagnation point where $\bar{\tau}_w = 0$. This indicates that, rather than forming from the wall shear stress relocating deposited particles to the peak where the shear is lower, these dunes form as a result of the advection induced by the vortices in the furrow.

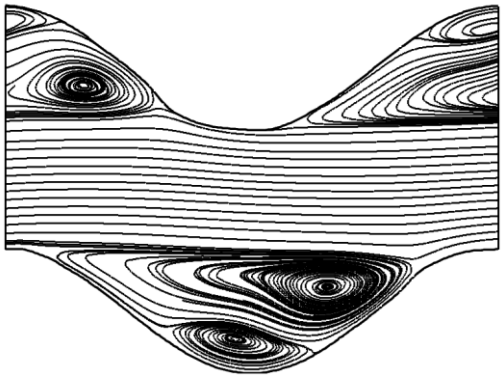

Figure 6.8 – Streamlines from the time averaged velocity field in a single period near the inlet of a channel with *A* = 0.5, *L* = 4 and *P* = 2000.

Inside the furrow along the top wall a large vortex occupies the majority of the area while a second smaller vortex fills the remaining area at the top of the furrow. The vortices can be seen in Figure 6.8.which displays the streamlines from the time averaged velocity field in a single period near the inlet of the channel. Here, the velocity field is averaged from 10 samples spaced $T_{total}/500$ apart. In this figure, we see that the stagnation point corresponding to the edge of the small upper vortex near the inlet of the channel period coincides with the valley to the right of the far left dune at $x/l \approx 0.1$.

Particles entrained in the fluid near the wall, which are sufficiently far away from the stagnation point experience convective and thermophoretic velocities acting parallel and perpendicular to the wall, respectively. This results in the thermophoretic deposition of particles as they are convected along the wall. Closer to this point, the convective velocities begin to act away from the wall in the opposite direction of thermophoresis. With the reduced thermal gradients along this section of the wall, the thermophoretic velocity of the particles is insufficient to overcome convection, resulting in a decreased deposition at the location of the stagnation point. This leads to a growth rate which increases with the distance from the stagnation point, forming the right half of the far left dune and the adjoining valley seen in Figure 6.7 (a). The increase in the growth rate moving to the left, away from the stagnation point, continues until $x/l \approx 0.04$, where the peak of the dune is located. Beyond this location, with convection acting parallel with the wall, the growth rate of the fouling layer is governed by the thermophoretic velocity of the particles. As a result, the growth rate of the layer decreases with the decreasing Nu_l from $x/l \approx 0.04$ to $x/l \approx 0$ forming the left half of the far left dune.

In the right upper furrow, particles entrained in the upper vortex are carried upstream into the channel period from the neighboring period to the right. Due to the curvature of the furrow wall, streamlines in this vortex rapidly diverge from the location of the stagnation point as they approach the wall (see Figure 6.8). This results in the convective velocity diverting the majority of the particles entrained in the upper vortex away from the stagnation point on their approach to the wall. Because of this, the location of the highest concentration of particle deposition is shifted away from the stagnation point to $x/l \approx 0.96$. Here, the increased deposition leads to the formation of the far right dune. Beyond this

location the growth rate slows from decreasing thermophoretic velocities (indicated by the decreasing Nu_l), forming the right side of the dune.

The third featured accentuated by the growing fouling layer is the narrowing of the peak in the center dune. This occurs as the fluid streamlines are unable to follow along the wall of the growing dune. As a result, particles traveling in the streamlines near the surface, which are increasingly dominated by convection along the growing dune, are carried away from the wall, following the streamlines. Further along the dune, the streamlines return to their close proximity with the surface. This causes a decrease in the deposition of particles where the streamlines divert from the wall and an increase where they return. As discussed previously, the diverting streamlines also cause an abrupt change in the shear stress at that location. Comparing the shear stress distribution at $t = 3T_{total}/4$ and the fouling layer thickness at $t = T_{total}$ (Figure 6.7 (b)), we find that the location of reduced deposition which forms the narrowed peak corresponds to an abrupt decrease in the shear stress at $x/l \approx 0.38$. Furthermore, the neighboring section of increased deposition corresponds to increasing values of the shear stress, signifying the streamlines have returned close to the surface. This indicates that, starting around $t = 3T_{total}/4$, the shape of the flow causes a reduction in the deposition near $x/l \approx 0.38$, which results in a narrowing of the peak of the center dune seen at $t = T_{total}$.

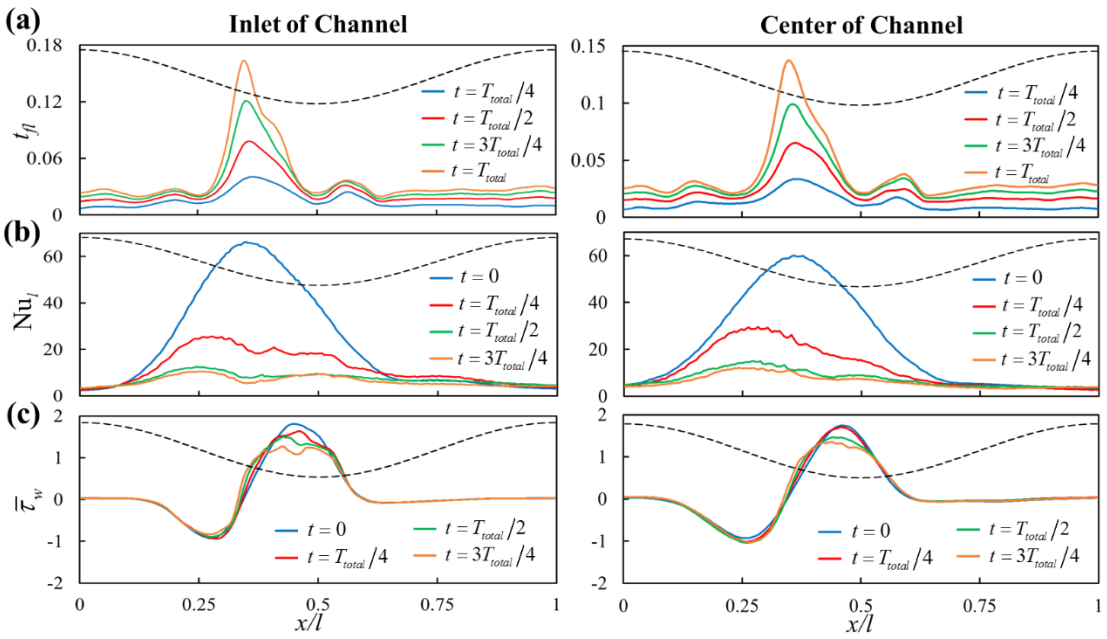

Figure 6.9 – Plots showing distribution of (a) fouling layer thickness (b) local Nusselt number and (c) wall shear stress along top wall of a single period near the inlet (left) and at the center (right) of a channel with *A* = 0.5, *L* = 4 and *P* = 2000.

Further along the channel near its center we find similar trends in the distributions of the fouling layer along the top wall to that seen near the inlet. This can be seen in Figure 6.9, which contains plots of the distributions of t_{fl}, Nu_l and $\overline{\tau}_w$ along the top wall of a period near the inlet and center period of the channel. Here, we see that in the center period, the fouling layer continues to develop three separate dunes along the peak of the wall. However, the thickness of the fouling layer is lower at this location further along the channel than it is near the inlet. This is due to a decreased growth rate of the fouling layer resulting from the decreasing concentration of particles in the fluid along the length of the channel. Along with the lower growth rate, slight variations in the shape of the distribution form as the layer develops. Specifically, the left and right dunes in the center period grow outward, away from the center dune as they increase in height, while those near the inlet grow vertically. As with the fouling layer, the wall shear stress and local Nusselt number

also contain similar distributions with only slight variations between two channels. Although these differences exist, the overall similarity between the effect of the developing and fully developed flow on the formation of the fouling layer indicates that, given sufficient time, the fouling layer will form in a similar manner regardless of its distance from the inlet.

6.3.2 Influence of Wall Amplitude

In order to investigate the influence of the wavy wall amplitude, we probe the fouling layer formation and its subsequent effects on the flow and heat transfer at wall amplitudes of $A = 0.25$, 0.5 and 0.75. Here, we fix the period length and driving pressure in each of the three channels at $L = 4$ and $P = 2000$, respectively. Examining the fouling layer formation at $t = T_{total}$, we find that all three amplitudes contain a peak at the location where the particle laden bulk flow reattaches to the top wall. This can be seen in Figure 6.10, which contains the fouling layer thickness along the top wall near the inlet of the channel at $t = T_{total}/2$ and $t = T_{total}$. Here, we see that for $A = 0.25$, in the initial stages of the fouling layer formation, the right dune discussed previously does not form along the wall. Instead, this channel develops two shorter, wider peaks with the larger of the two located on the front side of the wall peak, while the smaller is located on the backside. Furthermore, the remaining section of the wall develops a nearly uniform layer. With the additional growth in the layer at $t = T_{total}$, the valley between the dunes fills with deposits, resulting in the layer containing a single dune spanning nearly half the width of the wall and covering both sides of the wall peak.

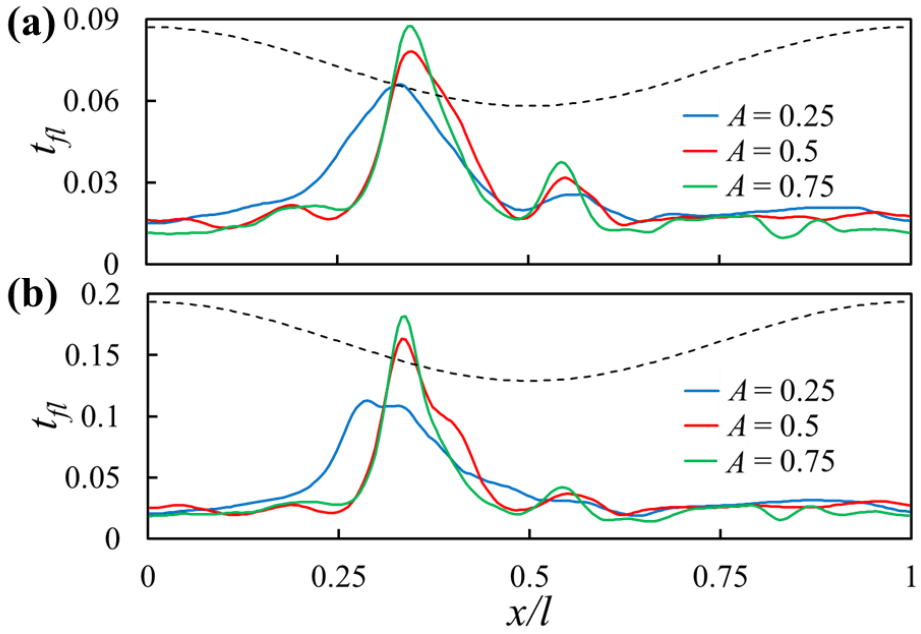

Figure 6.10 – Fouling layer thickness along top wall of period near inlet of channel at (a) $t = T_{total}/2$ and (b) $t = T_{total}$ for various amplitudes. Period length and driving pressure fixed at L = 4 and P = 2000, respectively.

As the amplitude of the channel increases, both the center and right dunes narrow as their height increases. This can be seen in the thickness distribution along the channel with $A = 0.75$. Furthermore, the effects of the smaller vortices forming in the furrow of the channel become more pronounced, leading to large variations in the thickness of the fouling layer along the wall of the furrow. Moreover, the fouling layer in the channel with $A = 0.75$ maintains a similar shape as it continues to grow from additional deposition.

The differences between the distributions along the wall of these three channels is a result of the differing flow patterns induced by the geometries. In small amplitude channels, the rapid shedding of vortices pulls fluid from the bulk flow along the center of the channel into the furrows. As discussed in Chapter 5, by bringing hot fluid into the cool furrow, the vortices act to enhance the heat transfer along a larger region of the wall. This wider region

of enhanced heat transfer can be seen in Figure 6.11, which contains the distributions of Nu_l at $t = 0$ and $t = T_{total}$. Similarly, these vortices also bring fluid containing high concentrations of particles into the furrow, resulting in a more uniform distribution of the fouling layer.

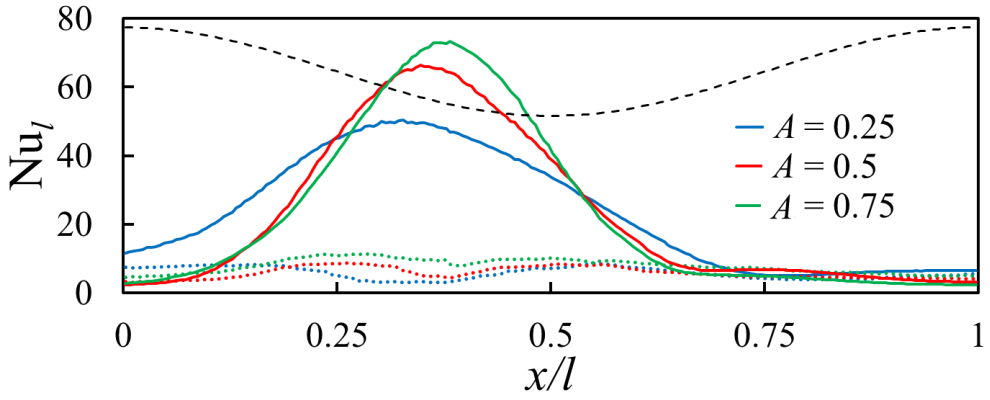

Figure 6.11 – Local Nusselt number along top wall of period near inlet of channel at $t = 0$ (solid lines) and $t = T_{total}$ (dotted lines) for various amplitudes. Period length and driving pressure fixed at L = 4 and P = 2000, respectively.

When the channel amplitude is increased, vortices trapped in the furrow inhibit the transport of fluid from the bulk flow into the furrow. This acts to narrow the section of the wall which experiences enhanced heat and mass transfer, leading to the narrower peak in the distribution of Nu_l as well as the center dune in the fouling layer. In spite of these differences in the shapes of the distributions, their average values are similar before the development of the fouling layer. Specifically, the averages for the three channels are $\mathrm{Nu}_{l,avg} = 23.3$, 22.9 and 23.1 for $A = 0.25$, 0.5 and 0.75, respectively.

Because the location of increased deposition coincides with that of the enhanced heat transfer, as the fouling layer develops it acts to even out heat transport along the wall. This

occurs for all three wall amplitudes, resulting in the nearly uniform distributions of Nu_l in Figure 6.11 at $t = T_{total}$ (dotted lines). Here, the average Nusselt numbers are reduced to $\mathrm{Nu}_{l,avg} = 5.8$, 5.8 and 7.9 for $A = 0.25$, 0.5 and 0.75, respectively. These reductions correspond to average fouling layer thicknesses of 0.041, 0.039 and 0.035.

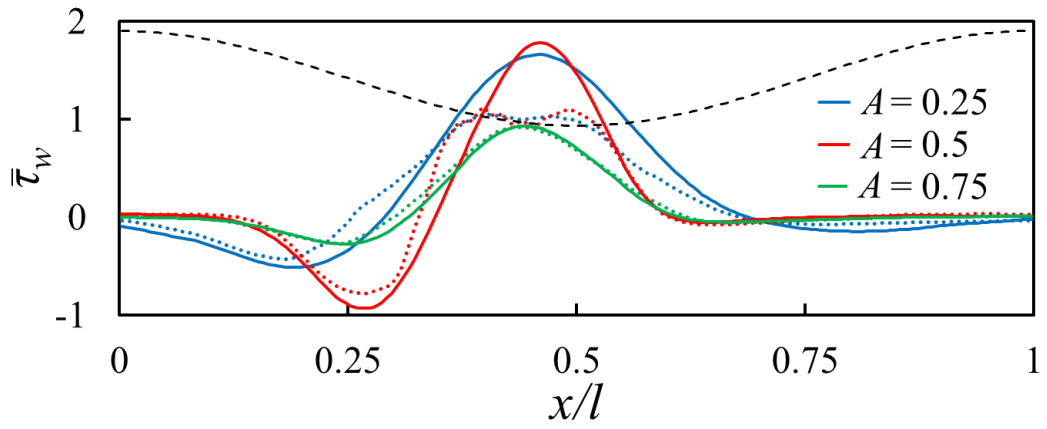

Figure 6.12 – Wall shear stress along top wall of period near inlet of channel at $t = 0$ (solid lines) and $t = T_{total}$ (dotted lines) for various amplitudes. Period length and driving pressure fixed at L = 4 and P = 2000, respectively.

Figure 6.12 contains the wall shear stress distributions along the top wall for the three different amplitude channels at $t = 0$ (solid lines) and $t = T_{total}$ (dashed lines). Here we see that, as with the heat transfer enhancement and particle deposition, the motion of the vortices along the furrow in the $A = 0.25$ amplitude channel induces a wider area of elevated shear stresses. Furthermore, as the frictional losses are less significant in the smaller amplitude channel, the average velocity is higher for a given driving pressure, P. Because of this, the channel with $A = 0.25$ has the largest average magnitude of the wall shear stress at $\bar{\tau}_{w,avg} = 0.48$, while those for $A = 0.5$ and 0.75 are $\bar{\tau}_{w,avg} = 0.38$ and 0.20, respectively. After the formation of the fouling layer, however, the channel with $A = 0.25$

experiences the largest reduction in its shear stresses, with its average decreasing to $\bar{\tau}_{w,avg} = 0.48$. The average wall shear stress for $A = 0.5$, on the other hand, decreases to $\bar{\tau}_{w,avg} = 0.32$ while the shear stress in the $A = 0.75$ channel remains at $\bar{\tau}_{w,avg} = 0.20$. Furthermore, this distribution of the wall shear stress in the channel with $A = 0.75$ remains nearly constant as the fouling layer develops.

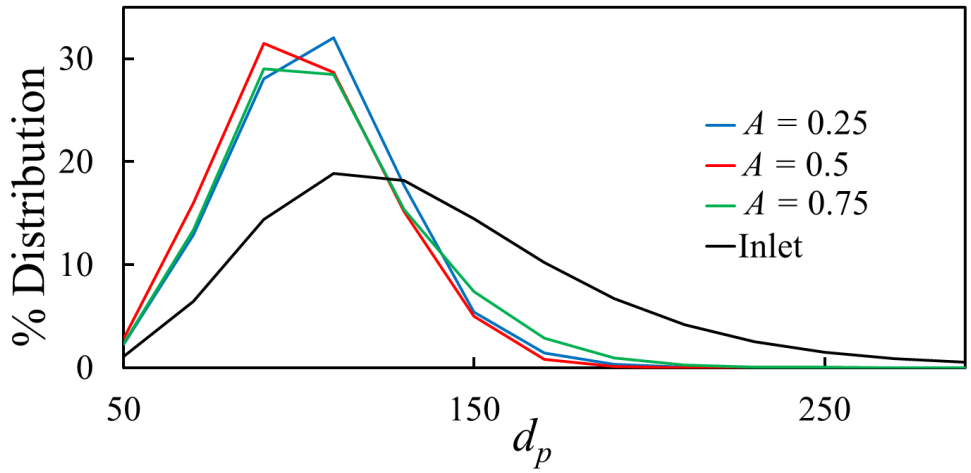

Figure 6.13 – Distribution of particle sizes deposited along top wall of period near inlet at $t = T_{total}$ for various wall amplitudes with L = 4 and P = 2000. Black line representing particle distribution at the inlet included for comparison.

Figure 6.13 contains the distributions of particles sizes along the top wall near the inlet of the channel for the three different amplitude channels at $t = T_{total}$, along with the distribution of particles sizes entering the channel. Here, we see that due to the wall shear stresses, particles with diameters of $d_p \geq 210$ nm are unable to deposit along the wall. This narrows the distribution, increasing the relative amount of smaller diameter particles compared to the inlet distribution. Comparing the distributions for the three wall amplitudes, we find that the increasing shear stresses associated with smaller amplitudes

act to further narrow the range of particle sizes. However, this narrowing is minimal due to the three channels inducing wall shear stress distributions of similar magnitude.

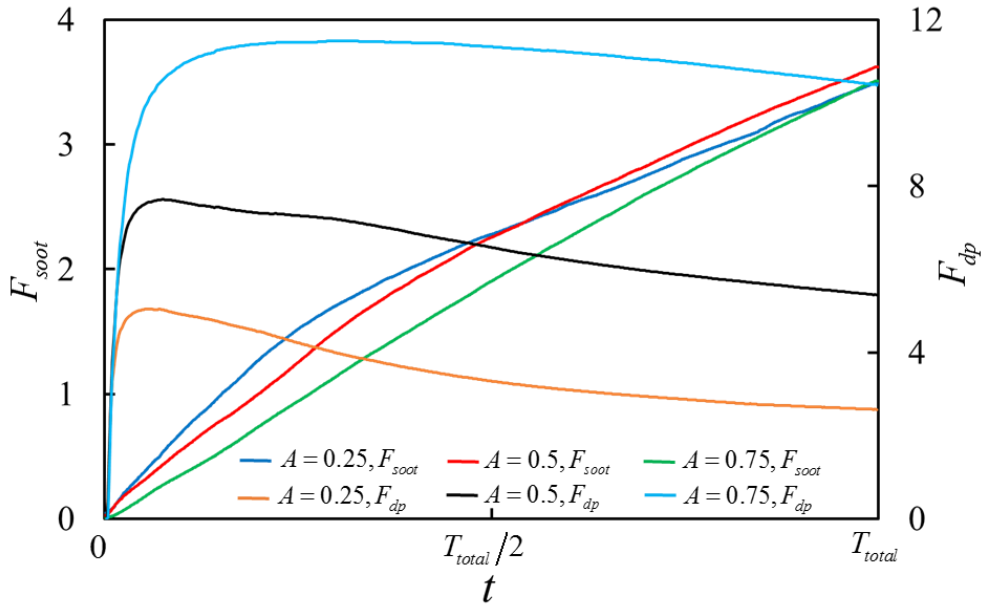

Figure 6.14 – Plot showing the time distributions of F_{soot} and F_{dp} for channels with amplitudes of A = 0.25, A = 0.5 and A = 0.75. Period length and driving pressure fixed at L = 4 and P = 2000, respectively.

Over the course of its development, the fouling layer occupies similar areas in each of the three channels. This can be seen in Figure 6.14, which contains the time distributions of F_{soot} and F_{dp} in each channel. Here, $F_{soot}(t)=\left(A_{soot}(t)/A_{channel}\right)\times 100$, is the percent of the total area of the channel occupied by the fouling layer, while $F_{dp}(t)=\left(N_{dep}(t)/N_{total}(t)\right)\times 100$ is the percent of the total particles entering the system, which have deposited along the wall. Comparing F_{soot} in each channel, we find that the fastest growth rate occurs in the channel with $A=0.25$ while $A=0.75$ has the slowest. Near $t=0.25T_{total}$ and $t=0.35T_{total}$ the growth rate slows for $A=0.25$ and $A=0.5$, respectively. The channel with $A=0.75$, on the other hand, retains a nearly constant

growth rate. As a result, at $t = T_{total}$ the fouling layer occupies 3.5%, 3.5% and 3.6% of the total area of the channel for $A = 0.25$, 0.5 and 0.75, respectively. The growth rates at $t = T_{total}$ suggest that with continued fouling, $A = 0.75$ will occupy the largest area, while $A = 0.25$ will occupy the smallest.

Although the fouling layers at $t = T_{total}$ possess nearly identical areas, the total number of particles passing through the channel decreases with increasing amplitude. This is a result of the reduced flowrates found in larger amplitude channels for a given driving pressure. Because of this, the total number of particles passing through the channel by $t = T_{total}$ is 5.4×10^9, 2.3×10^9 and 8.6×10^8 for $A = 0.25$, 0.5 and 0.75, respectively. In order to account for the differences in particle throughput we compare the percent of the current total throughput which have deposited, F_{dp}. Using this measurement, we find that with a maximum of $F_{dp} = 11.5$, the channel with $A = 0.75$ experiences the largest percentage of particles depositing onto its walls, while the channel with $A = 0.25$, with a maximum of 5.03, has the smallest. This indicates that the amplitude of the walls has a large influence of number of the particles depositing on the wall.

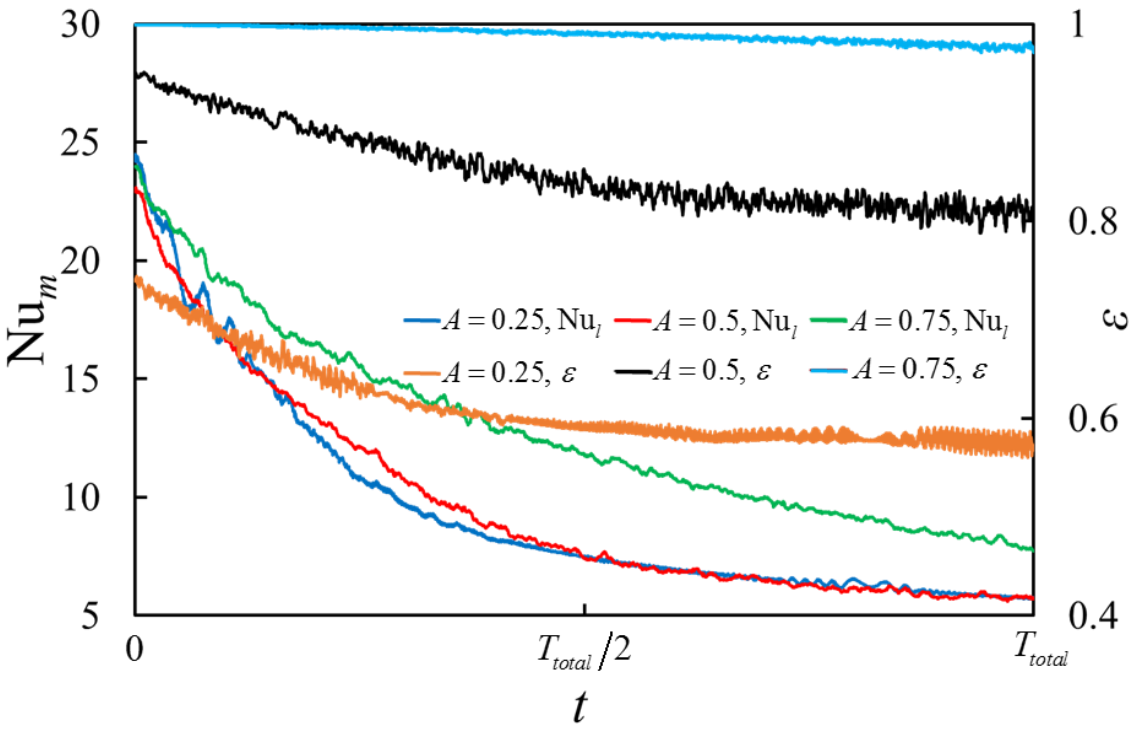

Figure 6.15 – Time distributions of the mean Nusselt number and heat exchanger effectiveness in channels with amplitudes of *A* = 0.25, *A* = 0.5 and *A* = 0.75. Period length and driving pressure fixed at *L* = 4 and *P* = 2000, respectively.

To compare the effects of fouling on the heat transfer performance, we provide a plot showing the time distributions of the mean Nusselt number and heat exchanger effectiveness in Figure 6.15. Here we see that, as discussed previously, the Nusselt number decreases due to the insulating effects of the growing fouling layer. For the channels with $A = 0.25$ and $A = 0.5$, the distributions of Nu_m follow similar trajectories decreasing from $\mathrm{Nu}_m = 24.5$ to 5.76 and $\mathrm{Nu}_m = 22.9$ to 5.70, respectively. The channel with $A = 0.75$, on the other hand, decreases at a much slower rate starting from $\mathrm{Nu}_m = 24.0$ at $t = 0$ and reducing to 7.74 by $t = T_{total}$. Furthermore, the effectiveness of this channel decreases only slightly throughout the development of the fouling layer reducing from $\varepsilon = 1$ to 0.97, while the effective decreases from $\varepsilon = 0.95$ to 0.80 for $A = 0.5$ and from

$\varepsilon = 0.74$ to 0.57 for $A = 0.25$. The $A = 0.75$ channel is able to maintain its effectiveness through the large contact times resulting from its lower flowrates. As a result, in the un-fouled channel, the fluid temperature reaches that of the walls at a location upstream from the outlet of the channel. The length of the channel beyond this location, therefore, remains free of deposits early in the layer formation allowing it to provide cooling as the channel fouls upstream. This "reserve capacity" allows for the channel to maintain its effectiveness as fouling occurs at the cost of lower throughput. For $A = 0.25$ and $A = 0.5$, which do not possess this "reserve capacity", the effectiveness decreases at a similar rate.

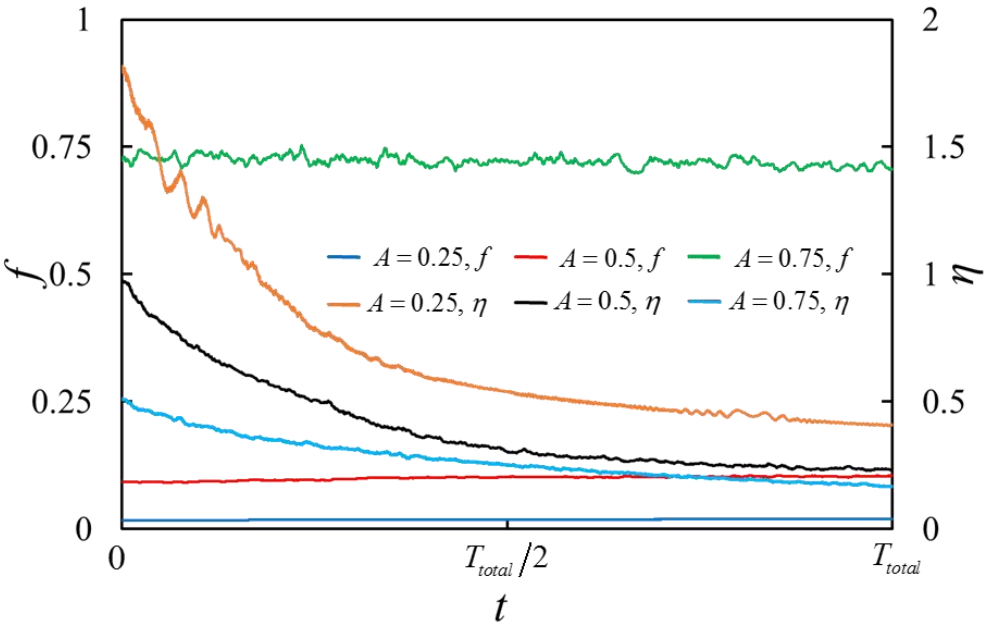

Figure 6.16 – Time distribution of friction factor and thermal-hydraulic performance factor in channels with amplitudes of *A* = 0.25, *A* = 0.5 and *A* = 0.75. Period length and driving pressure fixed at *L* = 4 and *P* = 2000, respectively.

As the fouling layer grows along the wall, it narrows the channel, increasing the friction factor f. This can be seen in Figure 6.16, which contains the time distribution of the friction factor and thermal-hydraulic performance factor, η, for each of the three

channels. Here, we see that, as expected, the friction factor increases with the wall amplitude. Unlike other properties of the flow, however, the friction factor for all three amplitude channels remains nearly constant. Although the friction factor undergoes minimal increases, the significant decrease in Nu_m acts to reduce the thermal-hydraulic performance of the channels. As discuss in the previous chapter, this factor provide a more complete description of the channels performance, by including the effects of increased losses induced along with the heat transfer enhancement. Using this performance factor, we seen that, before fouling occurs, the channel with $A = 0.5$ performs slightly worse than a straight channel at the same pressure drop ($\eta = 0.96$ versus $\eta = 1$), while the channel with $A = 0.75$ performs significantly worse at $\eta = 0.51$. Furthermore, over time their performance decreases further compared to an un-fouled straight channel. The channel with $A = 0.25$ initially outperforms a straight channel with $\eta = 1.82$, but as the heat transfer enhancement is reduced by fouling, this reduces to $\eta = 0.41$ at $t = T_{total}$.

Comparing the development of the fouling layer and its subsequent effects on the flow for channels containing wall amplitudes of $A = 0.25$, $A = 0.5$ and $A = 0.75$ with $L = 4$ and $P = 2000$, reveals each has advantages as well as disadvantages. For $A = 0.25$, the larger shear stress induced along the wall, coupled with lower thermal gradients in the fluid from the higher flowrate leads to a significantly smaller percentage of particles depositing along the wall. The benefits from the higher flowrate, however, are coupled with a lower residence time of the fluid resulting in a smaller effectiveness of the channel.

The channel with $A = 0.75$, conversely, experiences a larger percent of the particles entrained in the fluid depositing due to its lower flowrate and wall shear stress.

Furthermore, with its significantly higher friction factor, the large amplitude channel provides a suboptimal thermal-hydraulic performance without deposits, which worsens as the fouling layer develops. The lowered flowrates, on the other hand, provide the channel with "reserve capacity" for the given conditions, which mitigates the effects of the fouling layer formation on the effectiveness of the channel. However, this "reserve capacity" can be achieved with smaller amplitude channels by increasing their total length. Conversely, results discussed in Chapter 5 suggest that large amplitude channels are not capable of achieving $\eta > 1$ due to viscous losses.

Similar to $A = 0.75$, the channel with $A = 0.5$ suffers from poor thermal-hydraulic performance even before a fouling layer develops. Furthermore, after the formation of the fouling layer it continues to be outperformed by the channel with $A = 0.25$. Aside from the lower effectiveness resulting from the higher flowrates, the channel with $A = 0.25$ experiences the lowest total growth, and the largest thermal-hydraulic performance of the three amplitudes. This indicates that smaller amplitude channels are best suited to reduce the effects of the growing fouling layer.

6.3.3 Influence of Driving Pressure

In order to investigate the influence of the driving pressure, we probe the fouling layer formation and its subsequent effects on the flow and heat transfer at pressure drops of $P = 1500$, 2000 and 2500. Each pressure drop was applied to a channel with $A = 0.25$ and $L = 4$ as this geometry was determined to outperform channels containing larger amplitudes. Examining the fouling layer formation at $t = T_{total}$ we find that the distribution of the fouling layer thickness remains similar at each pressure drop. This can be seen in

Figure 6.17 which contains the distribution of the fouling layer thickness along the top wall for all three pressure drops. Here we see that the thickness of the layer varies slightly along the surface of the center dune, but remains comparable across the remaining length of the channel period.

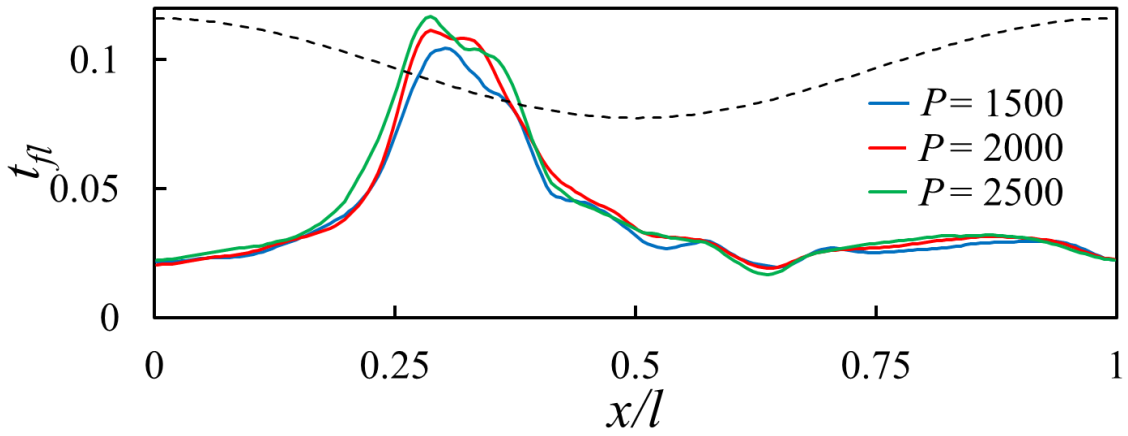

Figure 6.17 – Plot showing the fouling layer thickness along top wall of period near the inlet of channel at $t = T_{total}$ for various pressure drops with L = 4 and A = 0.25.

With the fouling layer forming similar distributions along the wall for each driving pressure in the channel, the total area occupied by the fouling layer follows comparable trajectories as well. This can be seen in Figure 6.18, which contains the time distributions of F_{soot} and F_{dp} for each pressure drop in the channel. Here we see that, despite an increase from $\mathrm{Re} \approx 700$ at $P = 1500$ to $\mathrm{Re} \approx 930$ at $P = 2500$, the area occupied by the fouling layer remains comparable for all three pressures throughout its development. Furthermore, the difference in F_{dp} for these driving pressures remains $< 1\%$ as well, with the largest percentage of particles depositing along the channel with the lowest pressure drop.

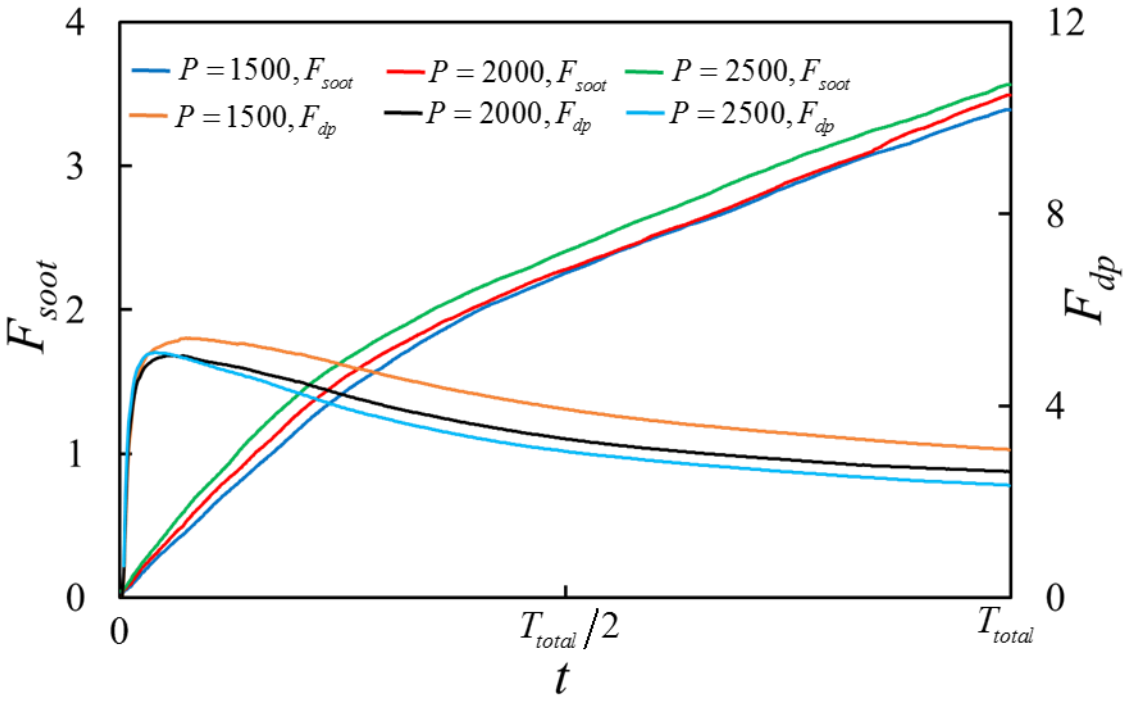

Figure 6.18 – Plots showing the time distributions of F_{soot} and F_{dp} in a channel with L = 4 and A = 0.25 at pressure drops of P = 1500, P = 2000 and P = 2500.

In order to understand how the fouling layers develop at similar rates despite the difference in flowrates, we examine the time distributions of the mean Nusselt number at each pressure drop. These distributions are provided for along with those of the distributions of the heat exchanger effectiveness in Figure 6.19. Here we find that, as expected, the initial Nu_m increases with increasing driving pressure. However, before the fouling layer reaches 2% of the channel area this difference in Nu_m becomes negligible with its value in all three flows decreasing to $\mathrm{Nu}_m \approx 5.8$. This difference in the heat transfer enhancement from $t = 0$ to $t = T_{total}/4$ corresponds to the early development of the fouling layer where the growth rate increases with increasing pressure drop. After $t = T_{total}/4$, when Nu_m is similar for the three pressure drops, the growth rates become similar as well with the lines slightly offset from the initial rates.

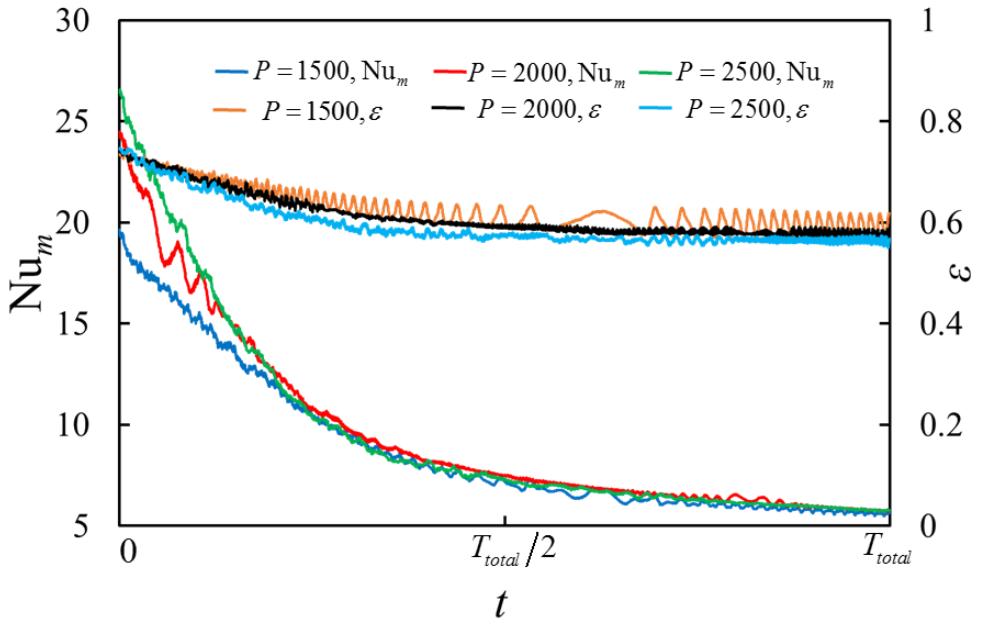

Figure 6.19 – Plots showing the time distributions of Nu_m and ε at pressure drops of P = 1500, P = 2000 and P = 2500 in a channel with L = 4 and A = 0.25.

Despite the lower residence time of the flow for higher pressure drops, the heat transfer enhancement induced by the larger flowrates is sufficiently large to achieve outlet temperatures lower than that found at $P=1500$. As a result, the heat transfer effectiveness in the un-fouled channel is $\varepsilon=0.73$, 0.74 and 0.75 for $P=1500$, 2000 and 2500, respectively. As the channel fouls and the heat transfer enhancement equalizes, the effectiveness for the larger driving pressures quickly drops below that of the smaller channel. Although the flow produced by $P=2500$ provides the lowest effectiveness by $t=T_{total}$, its value is only 5.3% smaller than that found at $P=1500$. Specifically, the final values of the effectiveness, which are averaged over the last 40 points to account for oscillations in the values, are $\varepsilon=0.59$, 0.57 and 0.56 for $P=1500$, 2000 and 2500, respectively.

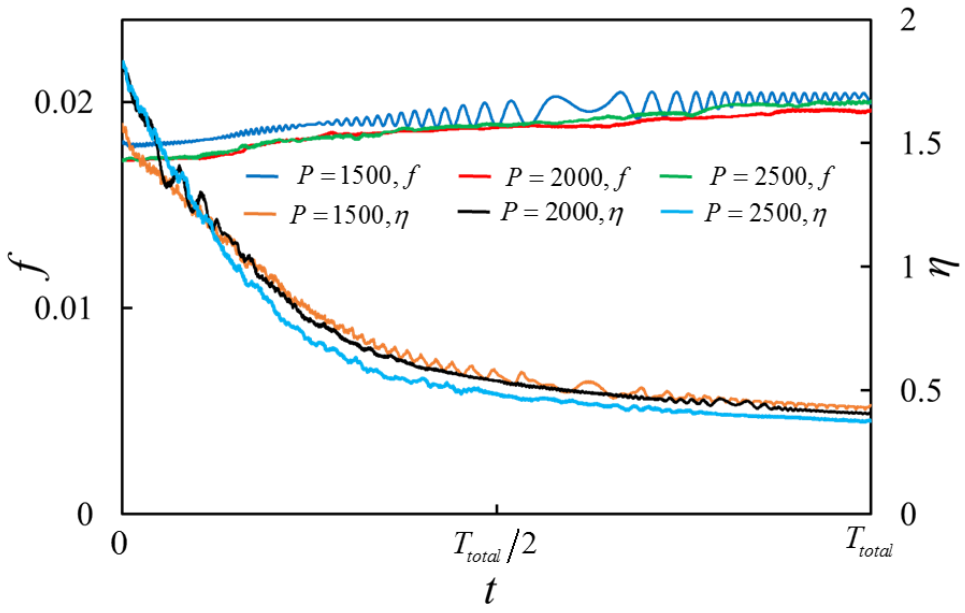

Figure 6.20 – Plots showing the time distributions of the friction factor and the thermal-hydraulic performance at pressure drops of P = 1500, P = 2000 and P = 2500 in a channel with L = 4 and A = 0.25.

Comparing the friction factor induced by each of the three pressure drops, we find similar distributions for each. This is expected, as we found in Chapter 4 that once the flow is sufficiently far into the unsteady regime, the friction factor depends heavily on the amplitude rather than the driving pressure. For $P = 2000$ and $P = 2500$, the distributions increase steadily over time, while for $P = 1500$ the friction factor experiences large oscillations. These oscillations, which are also found in the distribution of the effectiveness for this pressure drop, are the result of the unsteady flow induced by the geometry. Although the flows at each pressure drop oscillate from the effect of the wavy walls, the larger flowrates at $P = 2000$ and $P = 2500$ require longer distances to fully develop. As this developing flow is not spatially periodic, the average values across the channel experience minimal oscillation in their values. At $P = 1500$, however, the flow develops further upstream along the channel, resulting in a larger portion of the channel containing

spatially periodic flow. This leads to the oscillations along this section of the channel dominating the averages across the entire length of the channel. Furthermore, the growth in the fouling layer creates additional disturbances, which are amplified in the unstable flow, leading to increasing amplitude of the oscillations as well as the change in their period.

As with the heat transfer enhancement, the thermal-hydraulic performance is smallest for the lowest pressure drop at $t = 0$. However, as the fouling layer forms along the wall, the performance at $P = 2500$ decreases at the fastest rate, with that for $P = 2000$ decreasing at a slightly slower rate. This results in the channel with $P = 1500$ having the highest performance at $\eta = 0.43$ after the fouling layer develops, while $P = 2000$ and $P = 2500$ have performance values of $\eta = 0.41$ and $\eta = 0.38$, respectively. This is due to the heat transfer enhancement equalizing between the pressure drops, while the largest pressure drop continues to experience the largest relative friction factor compared to a straight channel.

Unlike the amplitude of the channel walls, the driving pressure has little effect on both the fouling layer formation as well as its effects subsequent effects on the system. At $P = 1500$ the thermal-hydraulic performance is slightly larger and the total area of the fouling layer is slightly smaller than those found at $P = 2000$ and $P = 2500$ after the fouling layer develops. However, this is coupled with a lower throughput into the channel. The flow at $P = 2500$, on the other hand, achieves an effectiveness within 6% of that found at $P = 1500$ while also experiencing similar values in its thermal-hydraulic performance

and fouling layer growth rate. Furthermore, this occurs at a throughput more than 30% larger than that found at $P = 1500$.

6.3.4 Influence of Wall Period Length

In order to investigate the influence of the wall period length, we probe the fouling layer formation and its subsequent effects on the flow and heat transfer in channels with period lengths of $L = 3$, 4 and 5. For each period length, the wall amplitude and driving pressure were fixed at $A = 0.25$ and $P = 2500$, respectively, as these values were previously determined to provide optimal conditions. Examining the fouling layer formation at $t = T_{total}$ we find that the distribution of the layer thickness varies significantly with the period length. This can be seen in Figure 6.21 which contains the distribution of the fouling layer thickness along the top wall for all three L. Here we see that the fouling layer continues to experience the largest deposition along the front side of the wall peak, leading to the formation of a large dune. The height and width of this dune, however, varies significantly across the different period lengths, with both its width and height decreasing with L. This is due to the relative amplitude of the channel walls increasing as the length decreases. As a result, the fouling layer in the channel with $L = 3$ appears similar to those found in the larger amplitude channels discussed previously.

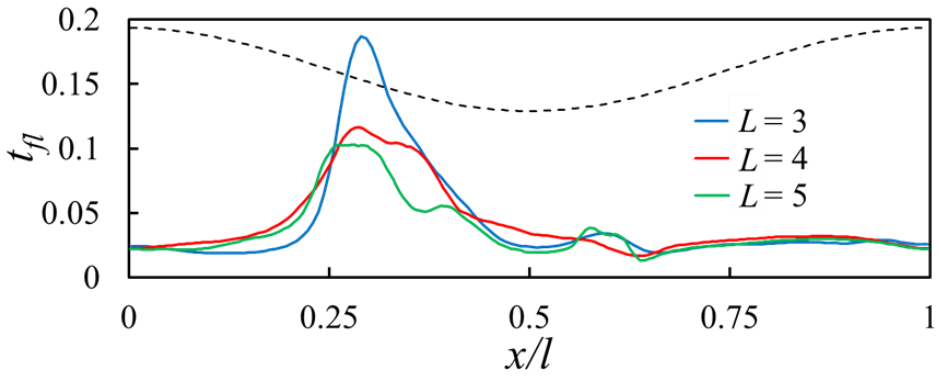

Figure 6.21 – Plot showing the fouling layer thickness along top wall of period near the inlet of channel at $t = T_{total}$ for various values of L with A = 0.25 and P = 2500.

When comparing the total area of the fouling layer, we find significant variations in the area throughout the fouling layer development. This can be seen in Figure 6.22 which contains the time distributions of F_{soot} and F_{dp} for each of the three channel geometries being investigated. In this plot we can see that initially, the fouling layers for all three period lengths grow at similar rates until $t \approx T_{total}/10$ when the rate for $L = 5$ begins to slow. This is followed soon after with a decrease in the channel with $L = 3$, leading to the $L = 4$ containing the largest area. At $t \approx 0.55T_{total}$, a noticeable increase in the growth rate for $L = 3$ occurs, while those in the other two channels continue to gradually decrease. This results in the channel with $L = 3$ occupying the largest fraction of the total channel area, followed by $L = 4$ and then $L = 5$ with the smallest.

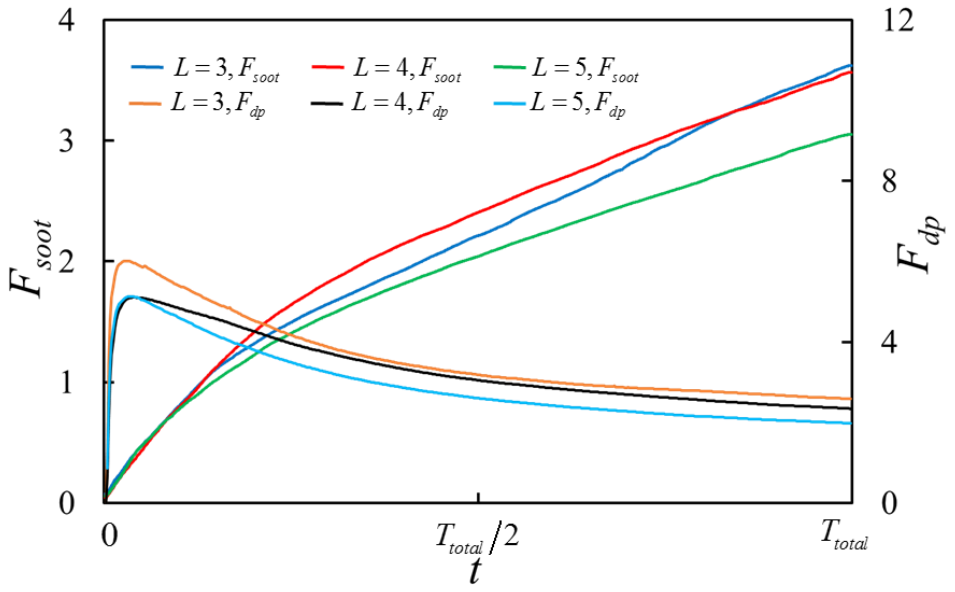

Figure 6.22 – Plot showing the time distributions of F_{soot} and F_{dp} in channels of various wall period lengths with A = 0.25 and P = 2500.

Comparing the fraction of the total particles deposited, we find that the sudden increase in the growth rate for $L=3$ corresponds to a slight deviation in its distribution of F_{dp} with that of $L=4$. This does not account for the large change in the growth rate, however. Because F_{dp} only represents the fraction of the particles which deposit, provide a plot of the time distribution of the total number of deposited particles in each of the three channels in Figure 6.23. Here we seen that for $L=4$ and $L=5$, the rate at which particles are depositing decreases at the wall fouls, while for $L=3$ the rate remains constant. Furthermore, as the fouling layer develops the changes it induces changes in the flow leading to an increase in the deposition of larger diameter particles. The can be seen in Figure 6.24, which contains the distribution of particle sizes deposited on the wall for $L=3$. Here, we see that after $t=T_{total}/2$, the deposition rate of particles with diameters of $d_p=130\,\text{nm}$ and $d_p=150\,\text{nm}$ increases. With this increase, coupled with the still constant

rate of total particle deposition, the growth rate of the fouling layer begins to increase as seen in Figure 6.22.

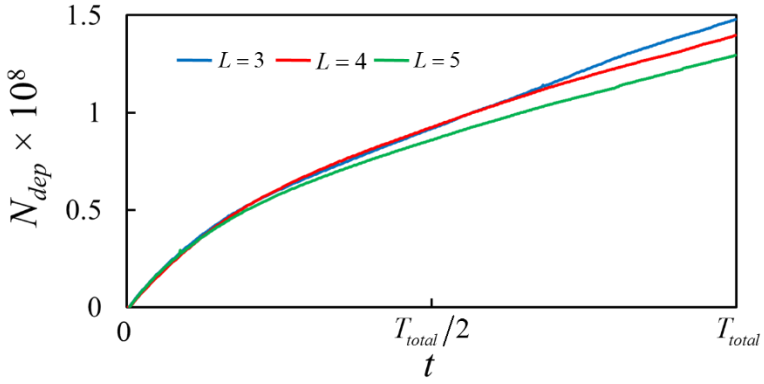

Figure 6.23 – Plot showing the total deposition of particles along the wall in channels of various wall period lengths with *A* = 0.25 and *P* = 2500.

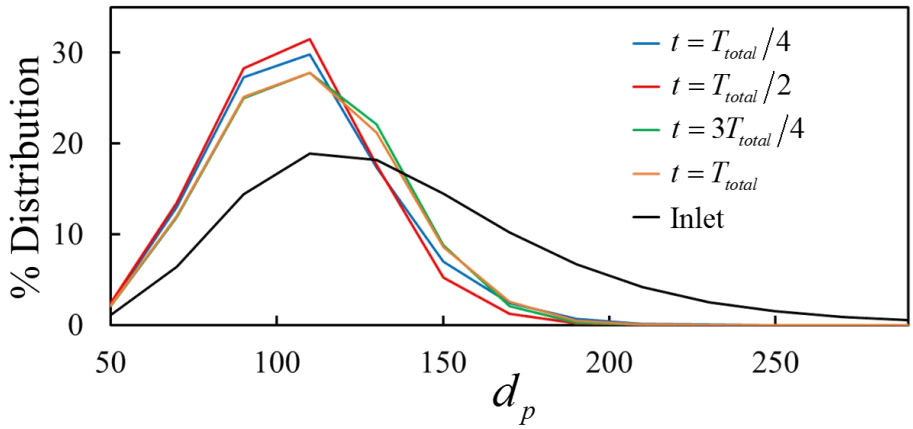

Figure 6.24 – Plot of the distribution of particle diameters deposited along the wall of a channel with *A* = 0.25, *L* = 3 and *P* = 2500.

Comparing the heat transfer enhancement for the three period lengths, we find that for the un-fouled channels, $L = 5$ has the largest value of Nu_m followed by $L = 3$ and $L = 4$ has the lowest. This can be seen in Figure 6.25, which contains the time distributions of the mean Nusselt number and heat exchanger effectiveness for the three channels. Here

we see that for all three channels, the distributions of Nu_m undergo similar decreases in value as the fouling layer grows. This results in $L=5$ maintaining its significantly larger values of Nu_m compared to that of the other channels. Due to the increased flowrate associated with longer periods, the channel with $L=3$ produces the largest values of the heat exchanger effectiveness, while the channel with $L=5$ produces the lowest. Unlike the similar values of the effectiveness seen for different driving pressure, the distributions for the three period lengths differ significantly. This is because, along with decreasing the flowrate, the shorter period length of the walls for $L=3$ acts to increase the relative wall amplitude, changing the flow structures found within channel.

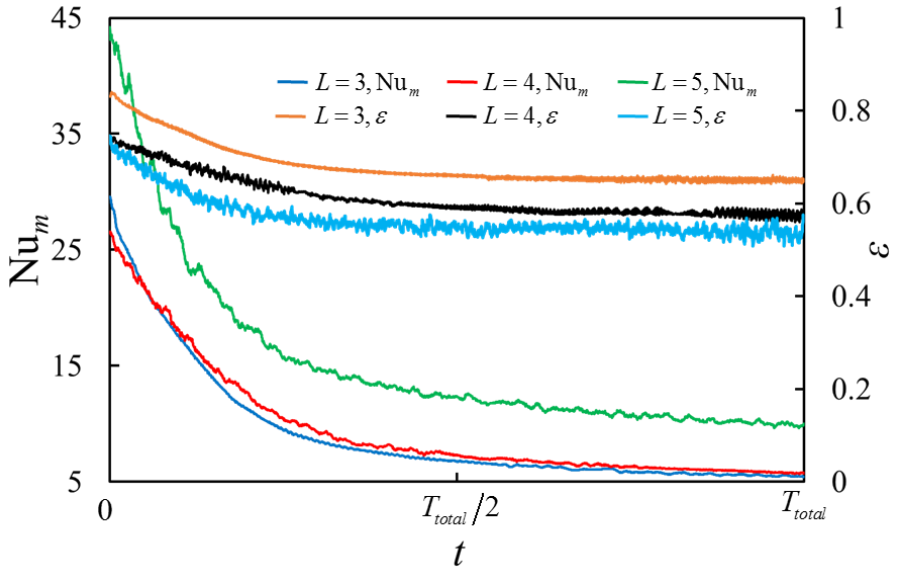

Figure 6.25 – Plot showing the time distributions of Nu_m and ε in channels of various wall period lengths with A = 0.25 and P = 2500.

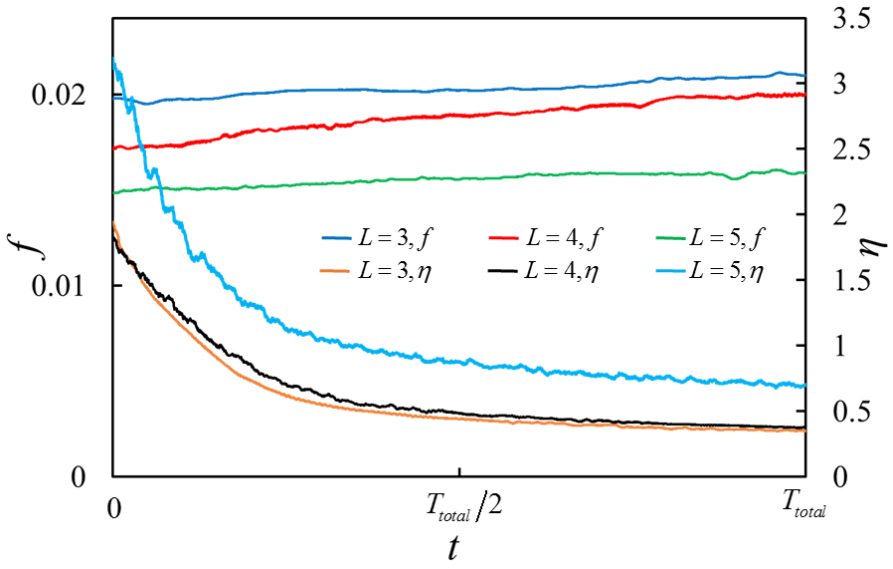

Figure 6.26 – Plot showing the time distributions of f and η in channels of various wall period lengths with *A* = 0.25 and *P* = 2500.

Comparing the effect of the fouling layer on the friction factor for the three channels we find that, as expected, f increases with decreasing period length. As discussed above, this is due to the larger relative wall amplitude for channels with smaller L. Because of the fouling layer acts to reduce the effective height of the channel, the friction factor of the flow increases as the layer grows. This is most pronounced in the channel with $L=4$, which increases by 16% by $T=T_{total}$, while the channels with $L=3$ and $L=5$ increase by 6.3% and 6.1%, respectively. The large increase seen for $L=4$, however, does not have a significant impact on the thermal-hydraulic performance of the channel as it follows a similar trajectory that of $L=3$. Additionally, the thermal-hydraulic performance found for $L=5$ undergoes a similar decrease. However, due to its larger initial value, the channel retains a significantly higher performance factor of $\eta=0.70$ at $T=T_{total}$ compared to the channels with $L=3$ and $L=4$, which decrease to $\eta=0.35$ and $\eta=0.38$, respectively.

With its smaller growth rate coupled with a higher thermal-hydraulic performance, the channel with $L = 5$ provides a substantially greater resistance to fouling compared to the two channels with smaller L. Moreover, this resistance is coupled with a total throughput which is 14% larger than that found in the channel with $L = 3$. Specifically, the channels contained flows with Reynolds numbers of $\mathrm{Re} = 860$, $\mathrm{Re} = 932$ and $\mathrm{Re} = 982$ for $L = 3$, $L = 4$ and $L = 5$, respectively. Furthermore, with comparable thermal-hydraulic performance, a smaller growth rate and an 8% greater throughput, the period length of $L = 4$ also provides a greater resistance to fouling compared to $L = 3$. This indicates a strong dependence of a channels resistance to the development of a fouling layer, and its effects on the flow and heat transfer.

6.4 Summary

Due to the interplay between the convective velocities induced by the unsteady flow, thermophoretic velocities induced by varying thermal gradients along the wall, and a non-uniform wall shear stress, the deposition of particles forms a fouling layer of varied thickness across each period of the channel. This varied thickness consists of two regions, one containing thick dune-like deposits located along the wall peak, and the other containing thinner more uniform deposits located along the wall furrow. The region containing thick deposits is characterized by large thermal gradients and wall shear stresses, while the region with thinner deposits contain lower thermal gradients and negligible stresses.

The thick deposits along the wall peak are the result of the elevated thermophoretic velocities induced by large thermal gradients along this section of the wall, coupled with

high concentrations of particles found in the surrounding fluid. This results in the rapid formation of a layer, which is shaped by the large shear stresses induced by the high velocity fluid traveling along the center of the channel. The resulting shape created by these effects takes the form of two or more dunes, with the largest located just before the center of the wall peak. In the furrows of the channel, the effect of the vortices reduces both the thermal gradients as well as the particle concentration in the region, resulting in the reduced deposition along the wall.

By concentrating the flow along the center of the channel, the wavy walls are able to produce larger wall shear stresses along the wall peaks compared to a straight channel at an identical pressure drop. As this region corresponds to that of the largest thermal gradients, this helps to reduce the deposition rate of larger diameter particles. However, due to the existence of a stagnation point where the flow reattaches to the wall, the shear stress is unable to reduce the deposition along the entire section of the wall experiencing elevated deposition. This results in the formation of the valleys and dunes characterizing the formation along the wall peak.

By systematically varying the wavy wall amplitude and period as well as the pressure gradient driving the flow, we were able to determine how these parameters influence the fouling layer formation. For the wall amplitude and period length, we determined that channels containing smaller relative amplitudes (A/L) are able provide the optimum conditions for mitigating the effects of the fouling layer formation. This is due to the larger thermal-hydraulic performance produced by these channels, coupled with a similar fouling layer growth rate and higher throughput achieved in these channels for a given pressure

drop. The pressure gradient in the range of $1500 \leq P \leq 2500$ has limited influence on the formation of the fouling layer and its subsequent effects on the system. However, these small differences are found in flows with varied throughput. Therefore, larger pressure gradients, with their similar resistance to fouling at a higher throughput offers better performance than a flows driven by lower pressure drops.

The insights gained from this research provide vital information necessary for the design of heat exchangers which are more resistant to the effects of fouling. Furthermore, the model developed for these investigations serves as a framework which will be extended to further examine the fouling layer formation in EGR heat exchangers.

CHAPTER 7. CONCLUDING REMARKS

In this dissertation we have studied the fluid flow, heat transfer enhancement and particle deposition occurring in an asymmetric wavy walled channel. Our investigations were conducted using a two-dimensional numeral model which utilized the lattice Boltzmann method, finite differences and Brownian dynamics to model the fluid flow, heat transfer and particle motion, respectively. Furthermore, we developed a fully coupled model for simulating the early stages of a growing fouling layer that results from particles depositing along the wall. These methods were implemented using the OpenCL© framework, which allowed for computational acceleration using GPUs. Our research used a stepwise approach first investigating the effect of the wavy walled geometry on the fluid flow, followed by an examination of the heat transfer enhancement and concluded by studying the particle transport and fouling layer formation along the walls.

In our investigation the effect of these channels on the fluid flow, we systematically examined how the structures of the flow as well as its stability are influenced by the amplitude and period of the wavy walls as well as the driving pressure. From this, we were able to determine the minimum pressure drops necessary to achieve unsteady as well as chaotic flows in the channel. Our investigations revealed that the transitions to each of the unsteady flow regimes exhibits a nontrivial dependence on the channel wall amplitude. The transition is related to an interplay among fluid inertia, disturbances introduced by wavy walls, and channel confinement. For small amplitude channels, the unsteady flow is characterized by vortex shedding and the absence of trapped vortices. In channels with larger wall amplitudes, confinement effects result in the trapping of vortices, which

oscillate within the furrows as shed vortices combine with them. Lastly, we showed that the geometry of the channel induces significant friction coefficients compared to a straight channel. Further, we demonstrated that the friction coefficient is nearly independent of the driving pressure when the flow is unsteady.

Using the insights gained from our examination of the fluid flow, we systematically investigated the effects of these same parameters on the heat transfer enhancement induced by the geometry. In the course of this research we determined that, while large amplitude channels outperform channels with smaller amplitudes in terms of heat transfer enhancement at low Reynolds numbers, once the flow becomes unsteady this difference in performance becomes negligible. Furthermore, we found that when comparing channels in terms of their thermal-hydraulic performance, smaller amplitude channels outperform larger amplitude channels. This is due to the increased viscous losses induced by the large amplitude channels.

Using the knowledge gained when investigating the flow and heat transfer enhancement in this geometry our research concluded with an examination of the fouling layer development in a wavy walled heat exchanger channel. Using our computational model, we studied the mechanisms driving the early formation of deposits along the wall. Here we found that the complex interactions between the flow structures, heat transfer enhancement and shear stress distribution generated by the wavy geometry induces a complicated fouling layer structure. Furthermore, we examined how the period and amplitude of the wavy walls, as well as the driving pressure influence the formation of these deposits. In the course of these investigations we determined that, as with the heat

transfer enhancement, small aspect ratio (A/L) wavy walled channels provide the greatest resistance to the effects of fouling.

The results from this research have impacts not only in EGR heat exchanger design, but on a wide range of engineering applications. This includes mixing and heat transfer in microscale devices which are incapable of achieving turbulent mixing, as well as designing more efficient general purpose heat exchangers were fouling may or may not be a significant issue. Furthermore, our computational model has provided a more comprehensive understanding of the physics governing the early fouling layer development.

Although this model contains significant improvements compared to previous models for simulating the fouling layer development in wavy walled channels, continued development is still necessary. This includes the extension of the model to three dimensions, as well as the inclusion of models for turbulence and the transport and condensation of hydrocarbons. This improved model can be utilized for further investigation into the fouling of wavy walled EGR heat exchangers. Moreover, a systematic examination of a wide range of complex geometries, such as converging-diverging channels, corrugated pipes and ribbed plates, is necessary to determine the geometry best suited for use in EGR coolers.[9] This task, which would be prohibitively expensive if performed experimentally, could be accomplished using this computational model. Furthermore, as heat exchanger fouling impacts many different industries, these investigations should be extended to examine other forms of fouling beyond the particulate fouling found in EGR coolers. These include biological, scaling, crystallization, corrosive

as well as chemical fouling.[146] As of now, many consider heat exchanger fouling to be the major unsolved problem in heat transfer.[147] However, with the ever increasing power and speed of computers, computational modeling is well poised to tackle the monumental task of solving this problem.

.

REFERENCES

1 R. C. Xin and W. Q. Tao, "Numerical Prediction of Laminar-Flow and Heat-Transfer in Wavy Channels of Uniform Cross-Sectional Area," *Numerical Heat Transfer,* vol. 14, pp. 465-481, 1988.

2 A. M. Jacobi and R. K. Shah, "Air-side flow and heat transfer in compact heat exchangers: A discussion of enhancement mechanisms," *Heat Transfer Engineering,* vol. 19, pp. 29-41, Oct-Dec 1998.

3 V. Hessel, H. Lowe, and F. Schonfeld, "Micromixers - a review on passive and active mixing principles," *Chemical Engineering Science,* vol. 60, pp. 2479-2501, Apr-May 2005.

4 L. S. Ismail, R. Velraj, and C. Ranganayakulu, "Studies on pumping power in terms of pressure drop and heat transfer characteristics of compact plate-fin heat exchangers-A review," *Renew. Sust. Energ. Rev.*, vol. 14, pp. 478-485, Jan 2010.

5 M. S. Abd-Elhady, T. Zornek, M. R. Malayeri, S. Balestrino, P. G. Szymkowicz, and H. Muller-Steinhagen, "Influence of gas velocity on particulate fouling of exhaust gas recirculation coolers," *International Journal of Heat and Mass Transfer,* vol. 54, pp. 838-846, Jan 31 2011.

6 N. Epstein, "Elements of particle deposition onto nonporous solid surfaces parallel to suspension flows," *Experimental Thermal and Fluid Science,* vol. 14, pp. 323-334, May 1997.

7 C. H. He and G. Ahmadi, "Particle deposition with thermophoresis in laminar and turbulent duct flows," *Aerosol Science and Technology,* vol. 29, pp. 525-546, Dec 1998.

8 M. Abarham, J. Hoard, D. Assanis, D. Styles, E. Curtis, and N. Ramesh, "Review of soot deposition and removal mechanisms in EGR coolers," SAE Technical Paper2010.

9 J. Hoard, M. Abarham, D. Styles, J. M. Giuliano, C. S. Sluder, and J. M. Storey, "Diesel EGR cooler fouling," SAE Technical Paper2008.

10 T. Nishimura and S. Matsune, "Mass transfer enhancement in a sinusoidal wavy channel for pulsatile flow," *Heat and Mass Transfer,* vol. 32, pp. 65-72, Nov 1996.

11 M. S. Abd-Elhady, M. R. Malayeri, and H. Müller-Steinhagen, "Fouling problems in exhaust gas recirculation coolers in the automotive industry," *Heat Transfer Engineering,* vol. 32, pp. 248-257, 2011.

12 H. M. Kim, S. K. Park, K. S. Cho, H. M. Wang, D. H. Lee, D. K. Lee, *et al.*, "Investigation on the flow and heat transfer characteristics of diesel engine EGR coolers," *International Journal of Automotive Technology,* vol. 9, pp. 149-153, Apr 2008.

13 R. Zhan, S. T. Eakle, J. W. Miller, and J. W. Anthony, "EGR system fouling control," SAE Technical Paper2008.

14 R. Zhang, F. Charles, D. Ewing, J.-S. Chang, and J. Cotton, "Effect of diesel soot deposition on the performance of exhaust gas recirculation cooling devices," SAE Technical Paper 0148-7191, 2004.

15 J. Hoard, J. Giuliano, D. Styles, S. Sluder, J. Storey, S. Lewis, *et al.*, "EGR Catalyst for Cooler Fouling Reduction," *DOE Diesel Engine-Efficiency and Emissions Reduction, Detroit, MI,* pp. 1-22, 2007.

16 I. J. Sobey, "Flow through Furrowed Channels .1. Calculated Flow Patterns," *Journal of Fluid Mechanics,* vol. 96, pp. 1-26, 1980.

17 K. D. Stephanoff, I. J. Sobey, and B. J. Bellhouse, "On flow through furrowed channels. Part 2. Observed flow patterns," *J. Fluid Mech.*, vol. 96, pp. 27-39, 1980.

18 A. M. Guzman and C. H. Amon, "Transition to Chaos in Converging Diverging Channel Flows - Ruelle-Takens-Newhouse Scenario," *Physics of Fluids,* vol. 6, pp. 1994-2002, Jun 1994.

19 A. M. Guzman and C. H. Amon, "Dynamical flow characterization of transitional and chaotic regimes in converging-diverging channels," *J. Fluid Mech.,* vol. 321, pp. 25-57, Aug 25 1996.

20 C. H. Amon, A. M. Guzman, and B. Morel, "Lagrangian chaos, Eulerian chaos, and mixing enhancement in converging-diverging channel flows," *Physics of Fluids,* vol. 8, pp. 1192-1206, May 1996.

21 A. M. Guzman, T. A. Aracena, M. J. Cardenas, and R. A. Escobar, "Heat transfer characteriastics and enhancement in symmetric wavy channels in a frequency-doubling transition scenario," *Proceedings of the Asme/Jsme Thermal Engineering Summer Heat Transfer Conference 2007, Vol 2,* pp. 691-698, 2007.

22 A. M. Guzman, M. J. Cardenas, F. A. Urzua, and P. E. Araya, "Heat transfer enhancement by flow bifurcations in asymmetric wavy wall channels," *Int J Heat Mass Tran,* vol. 52, pp. 3778-3789, Jul 2009.

23 A. M. Guzmán, T. A. Aracena, F. A. Urzua, and R. A. Escobar, "Flow Bifurcations and Transition Scenarios in Confined Flows: Channel Geometry and Operational Parameter Dependency," in *ASME 2006 International Mechanical Engineering Congress and Exposition*, 2006, pp. 309-316.

24 A. M. Guzman, R. A. Hormazabal, and T. A. Aracena, "Heat Transfer Enhancement Due to Frequency Doubling and Ruelle-Takens-Newhouse Transition Scenarios in Symmetric Wavy Channels," *Journal of Heat Transfer-Transactions of the Asme,* vol. 131, Sep 2009.

25 K. J. Cho, M. U. Kim, and H. D. Shin, "Linear stability of two-dimensional steady flow in wavy-walled channels," *Fluid Dyn. Res.,* vol. 23, pp. 349-370, Dec 1998.

26 A. Cabal, J. Szumbarski, and J. M. Floryan, "Stability of flow in a wavy channel," *J. Fluid Mech.,* vol. 457, pp. 191-212, Apr 25 2002.

27 C. Canuto, *Spectral methods : evolution to complex geometries and applications to fluid dynamics*. Berlin ; New York: Springer, 2007.

28 C. C. Wang and C. K. Chen, "Forced convection in a wavy-wall channel," *International Journal of Heat and Mass Transfer,* vol. 45, pp. 2587-2595, Jun 2002.

29 G. Wang and S. P. Vanka, "Convective Heat-Transfer in Periodic Wavy Passages," *International Journal of Heat and Mass Transfer,* vol. 38, pp. 3219-3230, Nov 1995.

30 T. Nishimura, "Oscillatory Flow and Mass-Transfer within Asymmetric and Symmetrical Channels with Sinusoidal Wavy Walls," *Heat Mass Transfer,* vol. 30, pp. 269-278, Apr 1995.

31 T. Nishimura, A. Tarumoto, and Y. Kawamura, "Flow and Mass-Transfer Characteristics in Wavy Channels for Oscillatory Flow," *International Journal of Heat and Mass Transfer,* vol. 30, pp. 1007-1015, May 1987.

32 T. Nishimura, H. Miyashita, S. Murakami, and Y. Kawamura, "Effect of Strouhal Number on Flow Characteristics in a Symmetric Sinusoidal Wavy-Walled Channel for Oscillatory Flow," *Journal of Chemical Engineering of Japan,* vol. 22, pp. 505-511, Oct 1989.

33 T. Nishimura, H. Miyashita, S. Murakami, and Y. Kawamura, "Oscillatory flow in a symmetrical sinusoidal wavy-walled channel at intermediate Strouhal numbers," *Chem. Eng. Sci.,* vol. 46, pp. 757-771, 1991.

34 T. Nishimura, S. Murakami, and Y. Kawamura, "Mass-Transfer in a Symmetrical Sinusoidal Wavy-Walled Channel for Oscillatory Flow," *Chemical Engineering Science,* vol. 48, pp. 1793-1800, May 1993.

35 T. Nishimura and N. Kojima, "Mass-Transfer Enhancement in a Symmetrical Sinusoidal Wavy-Walled Channel for Pulsatile Flow," *International Journal of Heat and Mass Transfer,* vol. 38, pp. 1719-1731, Jun 1995.

36 T. Nishimura and S. Matsune, "Vortices and wall shear stresses in asymmetric and symmetric channels with sinusoidal wavy walls for pulsatile flow at low Reynolds numbers," *International Journal of Heat and Fluid Flow,* vol. 19, pp. 583-593, Dec 1998.

37 I. J. Sobey, "Oscillatory flows at intermediate Strouhal number in asymmetric channels," *J. Fluid Mech.,* vol. 125, pp. 359-373, 1982.

38 Y. Sui, C. J. Teo, P. S. Lee, Y. T. Chew, and C. Shu, "Fluid flow and heat transfer in wavy microchannels," *Int J Heat Mass Tran,* vol. 53, pp. 2760-2772, Jun 2010.

39 Y. Sui, C. J. Teo, and P. S. Lee, "Direct numerical simulation of fluid flow and heat transfer in periodic wavy channels with rectangular cross-sections," *Int J Heat Mass Tran,* vol. 55, pp. 73-88, Jan 15 2012.

40 Y. Sui, P. S. Lee, and C. J. Teo, "An experimental study of flow friction and heat transfer in wavy microchannels with rectangular cross section," *International Journal of Thermal Sciences,* vol. 50, pp. 2473-2482, Dec 2011.

41 L. Gong, K. Kota, W. Q. Tao, and Y. Joshi, "Parametric numerical study of flow and heat transfer in microchannels with wavy walls," *J. Heat Trans.-T. Asme,* vol. 133, p. 051702, May 2011.

42 K. Stone and S. P. Vanka, "Numerical study of developing flow and heat transfer in a wavy passage," *J Fluid Eng-T Asme,* vol. 121, pp. 713-719, Dec 1999.

43 K. M. S. S. P. Vanka, "Numerical Study of Flow and Heat Transfer in Wavy Passages," University of Illinois at Urbana-Champagne, Technical Report TR-118, 1997 1997.

44 T. A. Rush, T. A. Newell, and A. M. Jacobi, "An experimental study of flow and heat transfer in sinusoidal wavy passages," *International Journal of Heat and Mass Transfer,* vol. 42, pp. 1541-1553, May 1999.

45 H. M. Metwally and R. M. Manglik, "Enhanced heat transfer due to curvature-induced lateral vortices in laminar flows in sinusoidal corrugated-plate channels," *International Journal of Heat and Mass Transfer,* vol. 47, pp. 2283-2292, May 2004.

46 T. Nishimura, Y. Kajimoto, A. Tarumoto, and Y. Kawamura, "Flow Structure and Mass-Transfer for a Wavy Channel in Transitional Flow Regime," *J Chem Eng Jpn,* vol. 19, pp. 449-455, Oct 1986.

47 J. H. Zhang, J. Kundu, and R. M. Manglik, "Effect of fin waviness and spacing on the lateral vortex structure and laminar heat transfer in wavy-plate-fin cores," *International Journal of Heat and Mass Transfer,* vol. 47, pp. 1719-1730, Apr 2004.

48 R. M. Manglik, J. H. Zhang, and A. Muley, "Low Reynolds number forced convection in three-dimensional wavy-plate-fin compact channels: fin density effects," *International Journal of Heat and Mass Transfer,* vol. 48, pp. 1439-1449, Apr 2005.

49 R. K. Shah and D. P. Sekulic, *Fundamentals of heat exchanger design*: John Wiley & Sons, 2003.

50 M. Ahmed, M. Yusoff, K. Ng, and N. Shuaib, "The effects of wavy-wall phase shift on thermal-hydraulic performance of Al 2 O 3–water nanofluid flow in sinusoidal-wavy channel," *Case Studies in Thermal Engineering,* vol. 4, pp. 153-165, 2014.

51 Y. Bravo, J. L. Lázaro, and J. L. García-Bernad, "Study of Fouling Phenomena on EGR Coolers due to Soot Deposits. Development of a Representative Test Method," SAE Technical Paper 0148-7191, 2005.

52 R. Zhan, S. T. Eakle, J. W. Miller, and J. W. Anthony, "EGR system fouling control," *SAE International Journal of Engines,* vol. 1, pp. 59-64, 2008.

53 M. Abd-Elhady, C. Rindt, J. Wijers, and A. Van Steenhoven, "Particulate fouling in waste incinerators as influenced by the critical sticking velocity and layer porosity," *Energy,* vol. 30, pp. 1469-1479, 2005.

54 M. S. Abd-Elhady, C. C. M. Rindt, J. G. Wijers, A. A. van Steenhoven, E. A. Bramer, and T. H. van der Meer, "Minimum gas speed in heat exchangers to avoid particulate fouling," *International Journal of Heat and Mass Transfer,* vol. 47, pp. 3943-3955, Aug 2004.

55 C. S. Sluder, J. Storey, M. J. Lance, and T. Barone, "Removal of EGR Cooler Deposit Material by Flow-Induced Shear," *SAE International Journal of Engines,* vol. 6, pp. 999-1008, 2013.

56 C. Paz, E. Suarez, M. Concheiro, and J. Porteiro, "Experimental study of soot particle fouling on ribbed plates: Applicability of the critical local wall shear stress criterion," *Experimental Thermal and Fluid Science,* vol. 44, pp. 364-373, Jan 2013.

57 M. Abarham, J. Hoard, D. N. Assanis, D. Styles, E. W. Curtis, N. Ramesh, *et al.*, "Numerical modeling and experimental investigations of EGR cooler fouling in a diesel engine," SAE Technical Paper 0148-7191, 2009.

58 M. Abarham, P. Zamankhan, J. W. Hoard, D. Styles, C. S. Sluder, J. M. Storey, *et al.*, "CFD analysis of particle transport in axi-symmetric tube flows under the influence of thermophoretic force," *International Journal of Heat and Mass Transfer,* vol. 61, pp. 94-105, 2013.

59 H. Teng and G. Regner, "Particulate fouling in EGR coolers," *SAE International Journal of Commercial Vehicles,* vol. 2, pp. 154-163, 2009.

60 A. Warey, S. Balestrino, P. Szymkowicz, and M. R. Malayeri, "A One-Dimensional Model for Particulate Deposition and Hydrocarbon Condensation in Exhaust Gas Recirculation Coolers," *Aerosol Science and Technology,* vol. 46, pp. 198-213, 2012.

61 C. Paz, E. Suárez, A. Eirís, and J. Porteiro, "Development of a predictive CFD fouling model for diesel engine exhaust gas systems," *Heat Transfer Engineering,* vol. 34, pp. 674-682, 2013.

62 M. Paz, E. Suarez, M. Concheiro, and J. Portherio, "CFD transient simulation of fouling in an EGR cooler in a diesel exhaust environment," in *Proceedings of International Conference on Heat Exchanger Fouling and Cleaning*, 2013, pp. 247-254.

63 T. Han, A. Booth, S. Song, D. Styles, and J. Hoard, "Review and A Conceptual Model of Exhaust Gas Recirculation (EGR) Cooler Fouling Deposition and Removal Mechanism," in *Procceding of Internal Conference on Heat Exchanger Fouling and Cleaning*, 2015.

64 A. R. Razmavar and M. R. Malayeri, "A Simplified Model for Deposition and Removal of Soot Particles in an Exhaust Gas Recirculation Cooler," *Journal of Engineering for Gas Turbines and Power-Transactions of the Asme,* vol. 138, Jan 2016.

65 H. Teng and G. Regner, "Characteristics of Soot Deposits in EGR Coolers," *SAE International Journal of Fuels and Lubricants,* vol. 2, pp. 81-90, 2009.

66 M. J. Lance, C. S. Sluder, H. Wang, and J. M. Storey, "Direct measurement of EGR cooler deposit thermal properties for improved understanding of cooler fouling," SAE Technical Paper2009.

67 M. J. Lance, C. S. Sluder, S. Lewis, and J. Storey, "Characterization of field-aged EGR cooler deposits," *SAE International Journal of Engines,* vol. 3, pp. 126-136, 2010.

68 K. A. Strebel, "Simulations of Thermophoretic Deposition in Wavy Channels," Master of Science in Mechanical Engineering, Mechanical Engineering Department, University of Illinois at Urbana-Champaign, Urbana, Illinois, 2010.

69 K. Nagendra, D. K. Tafti, and A. K. Viswanathan, "Modeling of soot deposition in wavy-fin exhaust gas recirculator coolers," *Int. J. Heat Mass Tran.,* vol. 54, pp. 1671-1681, Mar 2011.

70 N. Krishnamurthy, "Investigation of Fouling in Wavy-Fin Exhaust Gas Recirculators," Master of Science in Mechanical Engineering, Mechanical

Engineering Department, Virginia Polytechnic Institute and State University, Blacksburg, Virginia, 2010.

71 K. O. W. Group, "The opencl specification," *Version*, vol. 1, p. 8, 2008.

72 S. Succi, *The lattice Boltzmann equation for fluid dynamics and beyond*. Oxford: Oxford University Press, 2001.

73 A. J. C. Ladd and R. Verberg, "Lattice-Boltzmann simulations of particle-fluid suspensions," *J. Stat. Phys.*, vol. 104, pp. 1191-1251, Sep 2001.

74 C. K. Aidun and J. R. Clausen, "Lattice-Boltzmann method for complex flows," *Annu. Rev. Fluid Mech.*, vol. 42, pp. 439-472, 2010.

75 S. Chen and G. D. Doolen, "Lattice Boltzmann method for fluid flows," *Annu Rev Fluid Mech*, vol. 30, pp. 329-364, 1998.

76 J. Hardy, Y. Pomeau, and O. D. Pazzis, "Time Evolution of a Two-Dimensional Classical Lattice System," *Physical Review Letters*, vol. 31, pp. 276-279, 1973.

77 N. A. Gershenfeld, *The nature of mathematical modeling*. Cambridge ; New York: Cambridge University Press, 1999.

78 D. A. Wolf-Gladrow, *Lattice-gas cellular automata and lattice Boltzmann models : An introduction*. New York: Springer, 2000.

79 U. Frisch, B. Hasslacher, and Y. Pomeau, "Lattice-Gas Automata for the Navier-Stokes Equation," *Physical Review Letters*, vol. 56, pp. 1505-1508, Apr 7 1986.

80 G. McNamara and G. Zanetti, "Use of the Boltzmann equation to simulate lattice-gas automata," *Physical Review Letters*, vol. 61, pp. 2332-2335, 1988.

81 F. J. Higuera and J. Jimenez, "Boltzmann approach to lattice gas simulations," *Europhysics Letters*, vol. 9, pp. 663-668, 1989.

82 Y. H. Qian, D. Dhumieres, and P. Lallemand, "Lattice Bgk Models for Navier-Stokes Equation," *Europhysics Letters*, vol. 17, pp. 479-484, Feb 1 1992.

83 S. Y. Chen, H. D. Chen, D. Martinez, and W. Matthaeus, "Lattice Boltzmann Model for Simulation of Magnetohydrodynamics," *Physical Review Letters*, vol. 67, pp. 3776-3779, Dec 30 1991.

84 D. Dhumieres, "Generalized Lattice-Boltzmann Equations," *Rarefied Gas Dynamics: Theory and Simulations*, vol. 159, pp. 450-458, 1994.

85 I. Ginzburg, "Lattice Boltzmann modeling with discontinuous collision components: Hydrodynamic and advection-diffusion equations," *Journal of Statistical Physics*, vol. 126, pp. 157-206, Jan 2007.

86 I. Ginzburg, "Equilibrium-type and link-type lattice Boltzmann models for generic advection and anisotropic-dispersion equation," *Advances in Water Resources,* vol. 28, pp. 1171-1195, Nov 2005.

87 E. G. Flekkoy, "Lattice Bhatnagar-Gross-Krook Models for Miscible Fluids," *Physical Review E,* vol. 47, pp. 4247-4257, Jun 1993.

88 X. He, S. Chen, and G. D. Doolen, "A novel thermal model for the lattice Boltzmann method in incompressible limit," *Journal of Computational Physics,* vol. 146, pp. 282-300, Oct 10 1998.

89 M. R. Swift, E. Orlandini, W. R. Osborn, and J. M. Yeomans, "Lattice Boltzmann simulations of liquid-gas and binary fluid systems," *Phys Rev E,* vol. 54, pp. 5041-5052, Nov 1996.

90 X. He, S. Chen, and R. Zhang, "A lattice Boltzmann scheme for incompressible multiphase flow and its application in simulation of Rayleigh–Taylor instability," *Journal of Computational Physics,* vol. 152, pp. 642-663, 1999.

91 Q. Zou and X. He, "On pressure and velocity boundary conditions for the lattice Boltzmann BGK model," *Physics of Fluids (1994-present),* vol. 9, pp. 1591-1598, 1997.

92 M. Bouzidi, M. Firdaouss, and P. Lallemand, "Momentum transfer of a Boltzmann-lattice fluid with boundaries," *Phys. Fluids,* vol. 13, pp. 3452-3459, Nov 2001.

93 A. J. C. Ladd, "Numerical simulations of particulate suspensions via a discretized Boltzmann-equation. Part 1. Theoretical foundation," *Journal of Fluid Mechanics,* vol. 271, pp. 285-309, Jul 25 1994.

94 M. N. Ozisik, *Finite difference methods in heat transfer*. Boca Raton: CRC Press, 1994.

95 S. Patankar, *Numerical heat transfer and fluid flow*: CRC press, 1980.

96 J. C. Tannehill, D. A. Anderson, and R. H. Pletcher, *Computational fluid mechanics and heat transfer,* 2nd ed. Washington, DC: Taylor & Francis, 1997.

97 S. A. M. Karimian and A. G. Straatman, "A thermal periodic boundary condition for heating and cooling processes," *International Journal of Heat and Fluid Flow,* vol. 28, pp. 329-339, Apr 2007.

98 K. E. Torrance, "Computational heat transfer," *Computational heat transfer*.

99 G. Karniadakis and R. M. Kirby, *Parallel Scientific Computing in C++ and MPI: A Seamless Approach to Parallel Algorithms and Their Implementation*: Cambridge University Press, 2003.

100 R. Verberg, J. M. Yeomans, and A. C. Balazs, "Modeling the flow of fluid/particle mixtures in microchannels: Encapsulating nanoparticles within monodisperse droplets," *Journal of Chemical Physics,* vol. 123, p. 224706, Dec 8 2005.

101 H. C. Ottinger, *Stochastic processes in polymeric fluids*. Berlin: Springer-Verlag, 1996.

102 R. Verberg, A. Alexeev, and A. C. Balazs, "Modeling the release of nanoparticles from mobile microcapsules," *J Chem Phys,* vol. 125, p. 224712, Dec 14 2006.

103 A. Messerer, R. Niessner, and U. Poschl, "Thermophoretic deposition of soot aerosol particles under experimental conditions relevant for modem diesel engine exhaust gas systems," *Journal of Aerosol Science,* vol. 34, pp. 1009-1021, Aug 2003.

104 D. Mehta, T. Alger, M. Hall, R. D. Matthews, and H. Ng, "Particulate Characterization of a DISI Research Engine using a Nephelometer and In-Cylinder Visualization," SAE Technical Paper 0148-7191, 2001.

105 P. A. Lakshminarayanan, Y. Shi, R. D. Reitz, and Y. V. Aghav, *Modelling Diesel Combustion*: Springer Netherlands, 2010.

106 C. Housiadas and Y. Drossinos, "Thermophoretic deposition in tube flow," *Aerosol Science and Technology,* vol. 39, pp. 304-318, Apr 2005.

107 L. Talbot, R. K. Cheng, R. W. Schefer, and D. R. Willis, "Thermophoresis of Particles in a Heated Boundary-Layer," *Journal of Fluid Mechanics,* vol. 101, pp. 737-758, 1980.

108 E. Cunningham, "On the velocity of steady fall of spherical particles through fluid medium.," *Proceedings of the Royal Society of London Series a-Containing Papers of a Mathematical and Physical Character,* vol. 83, pp. 357-365, Mar 1910.

109 C. Davies, "Coagulation of aerosols by Brownian motion," *Journal of Aerosol Science,* vol. 10, pp. 151-161, 1979.

110 G. Marsaglia and W. W. Tsang, "The ziggurat method for generating random variables," *Journal of statistical software,* vol. 5, pp. 1-7, 2000.

111 B. Dahneke, "The capture of aerosol particles by surfaces," *Journal of colloid and interface science,* vol. 37, pp. 342-353, 1971.

112 G. A. Somorjai and Y. Li, *Introduction to surface chemistry and catalysis*: John Wiley & Sons, 2010.

113 B. E. Lee, C. A. J. Fletcher, S. H. Shin, and S. B. Kwon, "Computational study of fouling deposit due to surface-coated particles in coal-fired power utility boilers," *Fuel,* vol. 81, pp. 2001-2008, Oct 2002.

114 C. Thornton and Z. M. Ning, "A theoretical model for the stick/bounce behaviour of adhesive, elastic-plastic spheres," *Powder Technology,* vol. 99, pp. 154-162, Sep 15 1998.

115 K. L. Johnson and H. M. Pollock, "The Role of Adhesion in the Impact of Elastic Spheres," *Journal of Adhesion Science and Technology,* vol. 8, pp. 1323-1332, 1994.

116 K. Johnson, K. Kendall, and A. Roberts, "Surface energy and the contact of elastic solids," in *Proceedings of the Royal Society of London A: Mathematical, Physical and Engineering Sciences,* 1971, pp. 301-313.

117 M. J. Lance, H. Bilheux, J.-C. Bilheux, S. Voisin, C. S. Sluder, and J. Stevenson, "Neutron Tomography of Exhaust Gas Recirculation Cooler Deposits," SAE Technical Paper 0148-7191, 2014.

118 H. Rosen and T. Novakov, "Identification of Primary Particulate Carbon and Sulfate Species by Raman-Spectroscopy," *Atmospheric Environment,* vol. 12, pp. 923-927, 1978.

119 M. Soltani and G. Ahmadi, "On particle adhesion and removal mechanisms in turbulent flows," *Journal of Adhesion Science and Technology,* vol. 8, pp. 763-785, 1994.

120 M. O'neill, "A sphere in contact with a plane wall in a slow linear shear flow," *Chemical Engineering Science,* vol. 23, pp. 1293-1298, 1968.

121 M. Matyka, Z. Koza, and Ł. Mirosław, "Wall orientation and shear stress in the lattice Boltzmann model," *Computers & Fluids,* vol. 73, pp. 115-123, 2013.

122 N. S. Altman, "An introduction to kernel and nearest-neighbor nonparametric regression," *The American Statistician,* vol. 46, pp. 175-185, 1992.

123 D. Leighton and A. Acrivos, "The lift on a small sphere touching a plane in the presence of a simple shear flow," *Zeitschrift für angewandte Mathematik und Physik ZAMP,* vol. 36, pp. 174-178, 1985.

124 F. P. Incropera, *Fundamentals of heat and mass transfer*. Hoboken: John Wiley, 2007.

125 K. Park, D. B. Kittelson, M. R. Zachariah, and P. H. McMurry, "Measurement of inherent material density of nanoparticle agglomerates," *Journal of Nanoparticle Research,* vol. 6, pp. 267-272, 2004.

126 A. S. Dorfman, *Conjugate problems in convective heat transfer*: CRC Press, 2009.

127 D. A. Yuen, L. Wang, X. Chi, L. Johnsson, W. Ge, and Y. Shi, *GPU solutions to multi-scale problems in science and engineering*: Springer, 2013.

128 Nvidia, "CUDA Programming guide," ed, 2008.

129 B. Gaster, L. Howes, D. R. Kaeli, P. Mistry, and D. Schaa, *Heterogeneous Computing with OpenCL: Revised OpenCL 1*: Newnes, 2012.

130 "Bolt: A C++ template library optimized for GPUs," ed, 2014.

131 D. B. Thomas, "The MWC64X random number generator," ed, 2011.

132 E. K. Donald, "The art of computer programming," *Sorting and searching,* vol. 3, pp. 426-458, 1999.

133 H. M. Metwally and R. M. Manglik, "Enhanced heat transfer due to curvature-induced lateral vortices in laminar flows in sinusoidal corrugated-plate channels," *Int J of Heat Mass Tran,* vol. 47, pp. 2283-2292, May 2004.

134 A. Cabal, "Stability of wall-bounded flow modified due to the presence of distributed surface roughness," Ph.D. Doctoral dissertation, Applied Mathematics, University of West Ontario, Ontario, 1999.

135 R. K. Shah and A. L. London, *Laminar flow forced convection in ducts : a source book for compact heat exchanger analytical data*. New York: Academic Press, 1978.

136 C. Housiadas, F. E. Larrode, and Y. Drossinos, "Numerical evaluation of the Graetz series," *International Journal of Heat and Mass Transfer,* vol. 42, pp. 3013-3017, Aug 1999.

137 F. Takens, "Detecting strange attractors in turbulence," in *Dynamical systems and turbulence, Warwick 1980*, ed: Springer, 1981, pp. 366-381.

138 N. H. Packard, J. P. Crutchfield, J. D. Farmer, and R. S. Shaw, "Geometry from a time series," *Physical review letters,* vol. 45, p. 712, 1980.

139 A. M. Fraser and H. L. Swinney, "Independent coordinates for strange attractors from mutual information," *Physical review A,* vol. 33, p. 1134, 1986.

140 G. P. Williams, *Chaos theory tamed*: Joseph Henry Press, 1997.

141 D. Ruelle and F. Takens, "On the nature of turbulence," *Communications in mathematical physics,* vol. 20, pp. 167-192, 1971.

142 S. Newhouse, D. Ruelle, and F. Takens, "Occurrence of strange AxiomA attractors near quasi periodic flows onT m, m≧ 3," *Communications in Mathematical Physics,* vol. 64, pp. 35-40, 1978.

143 N. Mohamed, B. R. Wided, E. Mohamed, M. Abd el Karim, and B. Mohamed, "Numerical Investigation on the Fluid Flow and Heat Transfer in the Entrance Region of Wavy Channel," *Enrgy Proced,* vol. 36, pp. 76-85, 2013.

144 B. R. Munson, T. H. Okiishi, and W. W. Huebsch, *Fundamentals of fluid mechanics*, 6th ed. Hoboken, NJ: J. Wiley & Sons, 2009.

145 C. C. Wang and C. K. Chen, "Forced convection in a wavy-wall channel," *Int J Heat Mass Tran,* vol. 45, pp. 2587-2595, Jun 2002.

146 T. R. Bott, *Fouling of heat exchangers*: Elsevier, 1995.

147 S. Kakac, *Boilers, evaporators, and condensers*: John Wiley & Sons, 1991.

VITA

Zachary Grant Mills was raised in Athens, Georgia. He received his B.S. in Mechanical Engineering from the Georgia Institute of Technology in 2011, where he continued with his Ph.D. studies. Zach has worked with the Complex Fluids Modeling and Simulation Group under the direction of Dr. Alexander Alexeev since 2011. Zach's research interests are in all aspects of computational mechanics from numerical algorithms, software development, and data analysis to solve interdisciplinary problems in engineering and physics.